

**COMPUTER-AIDED MODELING AND  
SIMULATION OF FLOW OF SELF  
COMPACTING CONCRETE**

BY

**Faisal Mukhtar**

A Thesis Presented to the  
DEANSHIP OF GRADUATE STUDIES

**KING FAHD UNIVERSITY OF PETROLEUM & MINERALS**

DHAHRAN, SAUDI ARABIA

In Partial Fulfillment of the  
Requirements for the Degree of

**MASTER OF SCIENCE**

In

**Civil Engineering**

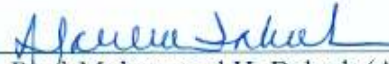
December, 2011

**KING FAHD UNIVERSITY OF PETROLEUM & MINERALS  
DHAHRAN 31261, SAUDI ARABIA**

**DEANSHIP OF GRADUATE STUDIES**

This thesis, written by **FAISAL MUKHTAR** under the direction of his thesis advisor and approved by his thesis committee, has been presented to and accepted by Dean of Graduate Studies, in partial fulfillment of the requirements for the degree of **MASTER OF SCIENCE IN CIVIL ENGINEERING**.


Thesis Committee



Prof. Mohammad H. Baluch (Advisor)



Dr. Muhammad K. Rahman (Co-Advisor)



Prof. Al-Farabi M. Sharif (Member)




Dr. Ali H. Al-Gadhib (Member)



Dr. Maher A. Bader (Member)

08 JAN 2012

  
Dr. Nedal A. Ratrou  
(Department Chairman)

  
Dr. Salam A. Zummo  
(Dean of Graduate Studies)



9/1/12  
Date

*This thesis is dedicated to*  
*My parents*  
*For their*  
*Innumerable prayers and encouragement*

## ACKNOWLEDGEMENTS

All praise be to ALLAH Subhanahu wa ta'ala for bestowing me with health, opportunity, patience and knowledge to complete this research. I acknowledge KFUPM for the support extended towards my research through its remarkable facilities and for providing me the opportunity to pursue graduate studies.

My sincerest gratitude goes to my advisor Prof. M.H Baluch and co-advisor Dr. M.K Rahman who guided me with their dedicated attention, expertise, and knowledge throughout this research. I am also grateful to my Committee Members, Prof. Al-Farabi M. Sharif, Dr. Ali H. Al-Gadhib and Dr. Maher A. Bader, for their constructive guidance and support. Thanks are also due to the other staff members of the Civil Engineering Department who helped me directly or indirectly.

I also acknowledge Messrs Redwan Hameed and Khaldoon Mohammed Slaiai as well as the entire staff of Saudi Ready-mix Concrete Company for their support during the research.

My heartfelt gratitude to my parents, brothers, sisters and all members of my family in Nigeria for their continuous love, encouragement, prayers, emotional and moral support throughout my life.

Special thanks are due to all my friends and colleagues for their guidance, support and encouragement throughout my stay at KFUPM.

# TABLE OF CONTENTS

<b>ACKNOWLEDGEMENTS</b> .....	<b>IV</b>
<b>TABLE OF CONTENTS</b> .....	<b>V</b>
<b>LIST OF TABLES</b> .....	<b>IX</b>
<b>LIST OF FIGURES</b> .....	<b>X</b>
<b>THESIS ABSTRACT</b> .....	<b>XIX</b>
<b>THESIS ABSTRACT (ARABIC)</b> .....	<b>XX</b>
<b>CHAPTER ONE</b> .....	<b>1</b>
<b>INTRODUCTION</b> .....	<b>1</b>
1.1 GENERAL.....	1
1.2 RESEARCH SIGNIFICANCE.....	3
1.3 RESEARCH AIM AND OBJECTIVES .....	4
1.4 SCOPE AND LIMITATIONS.....	6
1.5 RESEARCH METHODOLOGY.....	6
<i>1.5.1 Literature Review</i> .....	6
<i>1.5.2 Selection and Design of Concrete Mixes</i> .....	6
<i>1.5.3 Casting of Slab and Vertical Wall</i> .....	7
<i>1.5.4 Selection of Software for Simulation</i> .....	7
<i>1.5.5 Development of Model</i> .....	7
<i>1.5.6 Simulation of the SCC Flow Tests</i> .....	8
<i>1.5.7 Simulation of SCC Casting and Formwork Pressure</i> .....	8
<i>1.5.8 Analysis of Simulation and Experimental Results</i> .....	9
<b>CHAPTER TWO</b> .....	<b>10</b>
<b>LITERATURE REVIEW</b> .....	<b>10</b>
2.1 GENERAL.....	10
2.2 SIMULATION OF THE TESTING OF FRESH CONCRETE .....	11
2.3 SIMULATION OF CONCRETE CASTING.....	18

2.4 SIMULATION OF FORMWORK PRESSURE DUE TO SELF COMPACTING CONCRETE .....	22
<b>CHAPTER THREE.....</b>	<b>30</b>
<b>PRINCIPLES OF COMPUTATIONAL FLUID DYNAMICS (CFD) AND EQUATIONS GOVERNING THE MOTION OF A FLUID.....</b>	<b>30</b>
3.1 NAVIER-STOKES AND CONTINUITY EQUATIONS FOR.....	30
INCOMPRESSIBLE FLOW IN CARTESIAN COORDINATES.....	30
3.1.1 <i>Derivation of the Continuity Equation</i> .....	31
3.1.2 <i>Derivation of the Momentum (Navier-Stokes) Equations</i> .....	34
3.1.2.1 <i>Momentum Change and Flux</i> .....	35
3.1.2.2 <i>Derivation of Forces</i> .....	37
3.1.2.3 <i>Newtonian/Non-Newtonian Fluids</i> .....	39
3.2 NAVIER-STOKES AND CONTINUITY EQUATIONS FOR.....	40
INCOMPRESSIBLE FLOW IN CYLINDRICAL COORDINATES .....	40
3.2.1 <i>Continuity Equation</i> .....	40
3.2.2 <i>Momentum (Navier-Stokes) Equations</i> .....	44
3.3 PRINCIPLES OF COMPUTATIONAL FLUID DYNAMICS (CFD).....	45
<b>CHAPTER FOUR .....</b>	<b>47</b>
<b>EXPERIMENTAL INVESTIGATIONS AND RESULTS.....</b>	<b>47</b>
4.1 EXPERIMENTAL PROGRAM .....	47
4.1.1 <i>Preparation of SCC Mixes</i> .....	47
4.1.2 <i>Slump Flow and T500 Test</i> .....	48
4.1.3 <i>V-funnel Test</i> .....	49
4.1.4 <i>L-box Test</i> .....	51
4.1.5 <i>Determination of Rheological Parameters of Yield Stress and Viscosity</i> .....	52
4.1.5.1 <i>Stress Growth Test</i> .....	52
4.1.5.2 <i>Flow Curve Test</i> .....	55
4.1.6 <i>Full-Scale Casting of a Wall and Determination of Lateral Pressure on the Formwork – Instrumentation and Data Acquisition</i> .....	56

4.1.7 Full-Scale Casting of a Slab.....	59
4.2 RESULTS FOR THE EXPERIMENTAL PROGRAM AND DISCUSSION .....	61
4.2.1 Slump Flow, T500, L-box and V-funnel Tests .....	61
4.2.2 Rheology and Thixotropy Parameters.....	63
4.2.3 Flow Profiles during Slab Casting and Lateral Formwork Pressure .....	66
<b>CHAPTER FIVE .....</b>	<b>68</b>
<b>COMPUTATIONAL FLUID DYNAMICS SIMULATION OF SCC FLOW AND</b>	
<b>RESULTS.....</b>	<b>68</b>
5.1 GENERAL.....	68
5.2 NUMERICAL (CFD) SIMULATION OF SCC CONVENTIONAL TESTS .....	68
5.2 NUMERICAL (CFD) SIMULATION OF SCC CONVENTIONAL TESTS .....	70
5.2.1 Discretization Scheme .....	70
5.2.2 FLUENT Multiphase Modeling-The VOF Model [Fluent inc., 2003] .....	74
5.2.3 Defining the Input File .....	77
5.2.4 Modeling the Thixotropy of SCC: User-Defined Viscosity Function.....	79
5.3 NUMERICAL (CFD) SIMULATION OF THE SLAB CASTING .....	84
5.4 NUMERICAL (CFD) SIMULATION OF THE WALL CASTING.....	84
5.5 RESULTS OF THE NUMERICAL (CFD) SIMULATION OF SCC FLOW .....	85
TESTS .....	85
5.5.1 Slump Flow and T500 Test.....	88
5.5.2 L-box Test .....	91
5.5.3 V-funnel Test.....	92
5.6 RESULTS OF THE NUMERICAL (CFD) SIMULATION OF SLAB CASTING	
.....	94
5.7 RESULTS OF THE NUMERICAL (CFD) SIMULATION OF WALL CASTING	
AND RESULTING FORMWORK PRESSURE .....	98
<b>CHAPTER SIX.....</b>	<b>101</b>
<b>FINITE ELEMENT MODEL DEVELOPMENT AND SIMULATION RESULTS</b>	
<b>FOR THE EVOLUTION OF SCC FORMWORK PRESSURE .....</b>	<b>101</b>

6.1 GENERAL.....	101
6.2 DEVELOPMENT OF MODEL FOR THE FORMWORK PRESSURE.....	102
6.2.1 <i>Treatment of Boundary Conditions</i> .....	102
6.2.2 <i>Solution of Problem in ANSYS Environment</i> .....	106
6.3 THE PROPOSED FINITE ELEMENT MODEL (FEM) PREDICTIONS.....	107
VERSUS EXPERIMENTAL MEASUREMENTS .....	107
6.3.1 <i>Decay of Lateral Pressure with Respect to Time</i> .....	111
6.3.2 <i>Pumping Versus Casting</i> .....	117
6.3.3 <i>Effect of Casting Rate on Maximum Lateral Pressure</i> .....	118
<b>CHAPTER SEVEN .....</b>	<b>120</b>
<b>CONCLUSIONS AND RECOMMENDATIONS .....</b>	<b>120</b>
7.1 CONCLUSIONS .....	120
7.2 RECOMMENDATIONS FOR FUTURE RESEARCH .....	122
<b>APPENDIX: SCC FLOW TEST SIMULATION RESULTS .....</b>	<b>123</b>
<b>REFERENCES .....</b>	<b>144</b>
<b>VITA .....</b>	<b>148</b>



## LIST OF TABLES

Table 2.1: Classification of SCC According to their Flocculation Rate $A_{thix}$ .....	21
Table 4.1: Mix Proportions used for Casting of Slab and Wall Elements. ....	48
Table 4.2: Fresh Properties of SCC.....	62
Table 4.3: Bingham Parameters. ....	62
Table 4.4: Thixotropy Parameters for all Mixes. ....	65
Table 4.5: Experimental Results for the Full-Scale Slab Casting. ....	66
Table 4. 6: Experimental Results for the Pressure exerted on Formwok during the Full-Scale Wall Casting. ....	67
Table 5.1: Mix Proportions [Malik, 2011]. ....	69
Table 5.2: Thixotropy and Bingham Parameters for all Mixes [Malik, 2011].....	69
Table 5.3: Specifications for the Set Face Element Type Form.....	72
Table 5.4: FLUENT Model Parameters. ....	83
Table 5.5: Slump Flow and T-50 Test Results. ....	89
Table 5.6: L-box Test Results. ....	91
Table 5.7: V-funnel Test Results.....	93
Table 5.8: Experimental and Numerical Simulation Results for the Full-Scale Slab Casting. ....	95
Table 5.9: Experimental Pressure Measurements and Numerical Simulation During the Vertical Wall Casting Process. ....	98

## LIST OF FIGURES

Figure 2.1: Axi-Symmetric Numerical Simulation of Slump Test for SCC Without Fibres [Kulasegaram et al., 2010].	11
Figure 2.2: Axi-Symmetric Numerical Simulation of Slump Test for SCC With Fibres [Kulasegaram et al., 2010].	12
Figure 2.3: Different Snapshots of the L-box Test on SCC at Time (a) 0 s (b) 0.45 s (c) 0.85 s (d) 7.63 s with a Door Opening Time of 1 s [Dufour and Pijaudier-Cabot, 2005].	15
Figure 2.4: Evolution in Time of Concrete Height in Different Cross-Sections for SCC Flow in L-box Test [Dufour and Pijaudier-Cabot, 2005].	15
Figure 2.5: Examples of Obtained Shapes for the ASTM Cone [Roussel, 2004].	16
Figure 2.6: Slump in Terms of Yield Stress for ASTM Cone and Mini Cone [Roussel, 2004].	16
Figure 2.7: 2m Test Semi-Transparent Formwork [Roussel et al., 2007(b)].	19
Figure 2.8: Comparison between Experiments and Numerical Simulations for SCC with Yield Stress equal to (a) 120 Pa and (b) 60 Pa [Roussel et al., 2007(b)].	19
Figure 2.9: Numerical Simulations of the Multi-Layer Casting Phenomenon with $\tau_0 = 50 \text{ Pa}$ , $\mu_p = 50 \text{ Pa}\cdot\text{s}$ , $A_{\text{thix}} = 0.5 \text{ Pa/s}$ , $\alpha = 0.005$ . (a) 5-min resting time (b) 20-min resting time [Roussel, 2006].	22
Figure 2.10: Hydraulic Press and System of Automatic Data Acquisition	24
Figure 2.11: Instantaneous Simulation of 14 m High Concrete Column	24
Figure 2.12: Effect of Mixture Consistency on $p_{\text{max.}}/p_{\text{hyd}}$ . Values Determined on the 2.8m High Experimental Column [Assaad and Khayat (2006)].	25

Figure 2.13: Shape of the Formwork Considered for Analyses [Gallego et al., (2011)]	26
Figure 2.14: Comparison of Lateral Pressures obtained with the 2-D and 3-D Numerical Models and the Equations of the Current Standards [Gallego et al., (2011)]	27
Figure 2.15: Comparison between Experimental Results and Predictions by Eqs. 2.2 and 2.3 in the Case of a Rectangular Formwork and a Column [Ovalez and Roussel, 2006].	29
Figure 3.1: Elemental Fluid Volume for Derivation of the Fluid Equations in Cartesian Coordinates	31
Figure 3.2: Elemental Fluid Volume for Derivation of the Fluid Equations in Cylindrical Coordinates	41
Figure 3.3: Change of Variables from Cartesian to Cylindrical Coordinates.	44
Figure 3.4: Continuous Domain : PDEs + Boundary Conditions in Continuous Variables	46
Figure 3.5: Discrete Domain ( $x_1, x_2, \dots, x_N$ ): Algebraic Equations in Discrete Variables	46
Figure 4.1: Slump Flow and T500 Test.	49
Figure 4.2: V-funnel Test.	50
Figure 4.3: L-box Test.	51
Figure 4.4: ICAR Rheometer.	52
Figure 4.5: Stress Growth Test.	53

Figure 4.6: ICAR Rheometer Software Window [ICAR, 2008].	53
Figure 4.7: Cases where (a) All Material Flows and (b) Not All Material Flows.	55
Figure 4.8: Flow Curve Test.	56
Figure 4.9: A 2mX1.5mX0.2m Fabricated Formwork for the Measurement of Lateral Pressure Exerted by SCC due to Full-Scale Casting of a Wall.	57
Figure 4.10: (a) PWF-20MPB Pressure Transducer (b) Fixing Details.	58
Figure 4.11: Determination of the Calibration Coefficient:	59
Figure 4.12: Operations During the Wall Casting; (a) Mixing using a Truck Mixer.	60
Figure 4.13: Fabricated Formwork for the Study of Flow Profiles during the Casting of the Slab.	61
Figure 4.14: $\lambda$ vs Time at Constant Shear Rate.	63
Figure 4.15: $\lambda_0$ vs Resting Time.	64
Figure 5.1: Quadrilateral Face Element Types.	71
Figure 5.2: Triangular Face Element Types.	71
Figure 5.3: The Set Face Element Type Form.	71
Figure 5.4: Grid for the Axisymmetric Simulation of Slump Test.	73
Figure 5.5: Grid for the 2D Simulation of L-box Test.	73
Figure 5.6: Grid for the 2D Simulation of V-funnel Test.	74
Figure 5.7: Defining the Boundary Conditions.	78
Figure 5.8: Patching the Initial Location of SCC.	79
Figure 5.9: Summary of the Steps Needed to Obtain a CFD Solution.	82
Figure 5.10: 2D Simulation of Slab Casting (a) Grid (b) Contours of SCC at $t = 0$ sec	84

Figure 5.11: 2D Simulation of Wall Casting (a) Grid (b) Contours of SCC at t = 0 sec .....	85
Figure 5.12: Contours of Volume Fraction of SCC at t = 0 Sec. ....	86
Figure 5.13: Typical Progressive Flow of SCC during the Simulation of Slump Test for 2.5% Silica Fume.....	87
Figure 5.14: Typical Progressive Flow of SCC during the Simulation of L-box test for 2.5% Silica Fume.....	87
Figure 5.15: Typical Progressive Flow of SCC during the Simulation of V-funnel Test for 2.5% Silica Fume.....	88
Figure 5.16: Comparison between Experimental and Numerical Simulation for (a) Slump Flow, and (b) T-50 Tests. ....	89
Figure 5.17: Comparison between Experimental and Numerical Simulation for the L-box Test. ....	92
Figure 5.18: Comparison between Experimental and Numerical Simulation for the V-funnel Test.....	93
Figure 5.19: Comparison between Experiment and Numerical Simulation for the Slab Casting Process.....	95
Figure 5.20: Progressive Flow of SCC during the Simulation of Full-Scale Casting of the Slab.....	96
Figure 5.21: The Flow Profile of a Typical SCC Mix Too Stiff to have a Satisfactory Filling Ability.....	97
Figure 5.22: Progressive Flow of SCC during the Simulation of Full-Scale Casting of the Wall. ....	99

Figure 5.23: A CFD Solution for the Lateral Pressure Exerted on the Formwork at the End of Casting. ....	100
Figure 6.1: Formwork Geometry and Coordinate System. ....	102
Figure 6.2: 2D Boundary Shear Stress Distribution as a Function of the Resting Time .....	104
Figure 6.3: Physical Model of the Shear Boundary Condition using Discrete Springs of Time-Dependent Stiffness $k(t)$ . ....	104
Figure 6.4: Interdependency between the Steps in Solving the Problem. ....	108
Figure 6.5: Domain of the Modeled Fresh Concrete showing (a) Discrete Spring Elements and Meshing (b) Boundary Conditions. ....	109
Figure 6.6: A Finite Element Solution using the Proposed Model for the Lateral Pressure Exerted on the Formwork at the End of Casting. ....	110
Figure 6.7: Comparison between Experimental, Finite Element and CFD Simulation Results for the Lateral Pressure Variation at the Base of the Wall Formwork at Various Casting Heights. ....	111
Figure 6.8: Comparison between Literature Experimental Results [Khayat et al., 2005] and Predictions of the Proposed Model for the Evolution of Base Relative Lateral Pressure with Time after Casting at a Rate of $R=25m/hr$ . ....	113
Figure 6.9: Comparison between Literature Experimental Results [Khayat et al., 2005] and Predictions of the Proposed Model for the Evolution of Base Relative Lateral Pressure with Time after Casting at a Rate of $R=10m/hr$ . ....	113
Figure 6.10: The Finite Element Model Showing the Influence of Casting Rate on Lateral Pressure Variations. ....	114

Figure 6.11: Relative Effect of Thixotropy on Lateral Pressure Decay.....	114
Figure 6.12: Prediction of the Lateral Pressure Variation by the Proposed Finite Element Model at Various Heights above the Base of the 2.1m High Concrete Tested by Khayat et al. (2005).....	115
Figure 6.13: Comparison between Literature Experimental Results [Khayat et al. 2005] and Predictions of the Proposed Model of the Lateral Pressure Variations ((a) 1 hour (b) 2 hours (c) 3 hours) at Various Heights above the Base of a 2.1m High Column. ....	116
Figure 6.14: Comparison between Literature Experimental Results [Vanhove et al., 2004] and Predictions of the Proposed Model for the Evolution of Relative Lateral Pressure with Time after Casting at a Rate of $R=10.3m/hr$ and $A_{thix}=0.4Pa/s$ .....	118
Figure 6.15: Comparison between Prediction by the Model Proposed, Experimental Result by Khayat et al. (2005), and the Model Proposed by Ovarlez and Roussel (2006) for the Effect of Casting Rate on Relative Lateral Pressure at the Base of a 2.1m High Column. ....	119
Figure A 1: Progressive Flow of SCC during the Simulation of Slump Test for the Reference Mix. ....	124
Figure A 2: Progressive Flow of SCC during the Simulation of Slump Test for 5% Fly Ash.....	125
Figure A 3: Progressive Flow of SCC during the Simulation of Slump Test for 7.5% Fly Ash.....	126

Figure A 4: Progressive Flow of SCC during the Simulation of Slump Test for 10% Fly Ash.....	127
Figure A 5: Progressive Flow of SCC during the Simulation of Slump Test for 5% Lsp.....	128
Figure A 6: Progressive Flow of SCC during the Simulation of Slump Test for 10% Lsp.....	129
Figure A 7: Progressive Flow of SCC during the Simulation of Slump Test for 15% Lsp.....	130
Figure A 8: Progressive Flow of SCC during the Simulation of Slump Test for 2.5% Silica Fume.....	131
Figure A 9: Progressive Flow of SCC during the Simulation of Slump Test for 5% Silica Fume.....	132
Figure A 10: Progressive Flow of SCC during the Simulation of Slump Test for 7.5% Silica Fume.....	133
Figure A 11: Progressive Flow during the Simulation of L-box Test for the Reference Mix. ....	134
Figure A 12: Progressive Flow during the Simulation of L-box Test for the 5% Fly-Ash.....	134
Figure A 13: Progressive Flow during the Simulation of L-box Test for the 7.5% Fly-Ash.....	135
Figure A 14: Progressive Flow during the Simulation of L-box Test for the 10% Fly-Ash.....	135



Figure A 15: Progressive Flow during the Simulation of L-box Test for the 5% Lsp.....	136
Figure A 16: Progressive Flow during the Simulation of L-box Test for the 10% Lsp.....	136
Figure A 17: Progressive Flow during the Simulation of L-box Test for the 15% Lsp.....	137
Figure A 18: Progressive Flow during the Simulation of L-box Test for the 2.5% Silica Fume.....	137
Figure A 19: Progressive Flow during the Simulation of L-box Test for the 5% Silica Fume.....	138
Figure A 20: Progressive Flow during the Simulation of L-box Test for the 7.5% Silica Fume.....	138
Figure A 21: Progressive Flow during the Simulation of V-funnel Test for the Reference Mix. ....	139
Figure A 22: Progressive Flow during the Simulation of V-funnel Test for the 5% Fly-Ash.....	139
Figure A 23: Progressive Flow during the Simulation of V-funnel Test for the 7.5% Fly-Ash.....	140
Figure A 24: Progressive Flow during the Simulation of V-funnel Test for the 10% Fly-Ash.....	140
Figure A 25: Progressive Flow during the Simulation of V-funnel Test for the 5% Lsp.....	141

Figure A 26: Progressive Flow during the Simulation of V-funnel Test for the 10% Lsp.....	141
Figure A 27: Progressive Flow during the Simulation of V-funnel Test for the 15% Lsp.....	142
Figure A 28: Progressive Flow during the Simulation of V-funnel Test for the 2.5% Silica Fume.....	142
Figure A 29: Progressive Flow during the Simulation of V-funnel Test for the 5.0% Silica Fume.....	143
Figure A 30: Progressive Flow during the Simulation of V-funnel Test for the 7.5% Silica Fume.....	143

## THESIS ABSTRACT

**Name:** Faisal Mukhtar  
**Title:** Computer-Aided Modeling and Simulation of Flow of Self Compacting Concrete  
**Major Field:** Civil Engineering (Structures)  
**Date of Degree:** December, 2011

To make an optimum use of Self-Compacting Concrete (SCC), especially when planning the casting of concrete in complicated structures, simulation may serve as a tool in the construction and formwork design as well as determining the desired rheological parameters for a robust mix design of SCC.

The aim of this research work is the development and validation of the hydrodynamics of the flow behavior of SCC made from local materials found in Saudi Arabia using a continuum (single fluid) approach. Navier-Stoke's equations that govern the flow were used to obtain numerical solution of the problem using computational fluid dynamics (CFD) commercial software that enabled the tracking, in time and space, of material motion with any type of material behavior, including non-linear and time-dependent ones. The problem is characterized by free surface flow of a non-Newtonian fluid. While the rheological behavior can be described by means of a Bingham model, some extra phenomenon occurs in case of SCC, like shear thickening and sometimes significant thixotropy. For that reason, the Bingham behavior in combination with shear thickening and thixotropy was modeled in the software package FLUENT by means of a user-defined thixotropy model. Validation of the simulation results was achieved by using experimental data from a series of tests conducted at KFUPM using different SCC mixes to obtain the critical range of rheological parameters of yield stress and viscosity for robust mixes.

In addition, a new finite element model for the lateral pressure evolution in formwork due to SCC was developed in which the effects of thixotropy and casting rate were incorporated. Experimental investigation was conducted to verify the model developed for the lateral pressure evolution due to SCC and prediction of flow behavior during the full-scale casting of a slab. More experimental data from the literature were used to further validate the developed finite element model in this study. Simulation runs of full-scale casting of the slab were also carried out to study the effect of the rheological parameters on the flow of this material.

A successful validation of the CFD simulations and the finite element model's predictions shows a good correlation with the conducted experimental results and those from the literature.

**MASTER OF SCIENCE DEGREE**  
**KING FAHD UNIVERSITY OF PETROLEUM AND MINERALS**  
**Dhahran, Saudi Arabia.**

## THESIS ABSTRACT (ARABIC)

### ملخص الرسالة

**الاسم:** فيصل مختار.  
**عنوان الرسالة:** استخدام الحاسوب لمحاكاة ونمذجة تدفق الخرسانة ذاتية الدمك.  
**التخصص:** الهندسة المدنية.  
**تاريخ التخرج:** كانون الأول 2011م.

للحصول على استخدام أمثل للخرسانة ذاتية الدمك (SCC)، وخصوصاً عند التخطيط لصب الخرسانة في هياكل معقدة، يمكن توظيف المحاكاة كأداة في تصميم البناء والقوالب، وكذلك تحديد المعايير المطلوبة لتصميم مزيج متين من الخرسانة ذاتية الدمك.

الهدف من هذا العمل البحثي هو التطوير والتحقق من تدفق الخرسانة ذاتية الدمك المصنوعة من مواد محلية وجدت في المملكة العربية السعودية باستخدام نهج السلسلة المتصلة (السائل واحد). حيث استخدمت معادلات نافير ستوك التي تحكم التدفق للحصول على الحل العددي لهذه المشكلة باستخدام ديناميكيات السوائل الحسابية (CFD)، والبرمجيات التجارية التي تمكن التتبع، في الزمان والمكان، حركة المواد مع أي نوع من السلوك المادي، بما في ذلك غير الخطية التي تتبدل مع الزمن. وتتميز هذه المشكلة من خلال التدفق الحر لسطح السائل غير النيوتروني. بينما يمكن تمثيل سلوك الريولوجية عن طريق نموذج بينجهام، وتحدث بعض الظواهر في حالة الخرسانة ذاتية الدمك، مثل سماكة القص، وأحياناً الانسيابية الكبيرة، ولهذا السبب، تم نمذجة سلوك بينجهام بالاتحاد مع سماكة القص والانسيابية باستخدام برنامج فلوينت (FLUENT) عن طريق استخدام النموذج الانسيابي.

بالإضافة إلى ذلك، تم تطوير نموذج العناصر المحدودة لتقييم الضغط الجانبي الناتج من الخرسانة ذاتية الدمك مع الأخذ بالاعتبار تأثير الانسيابية ومعدل الصب. وقد تم التحقق من نتائج المحاكاة باستخدام البيانات المتاحة من التجارب، حيث نفذت بالفعل سلسلة من التجارب باستخدام خلطات مختلفة من الخرسانة ذاتية الدمك للحصول على العديد من المعاملات الريولوجية الحرجة من إجهاد الخضوع واللزوجة ومتانة الخليط. ومع ذلك، أجريت بعض التجارب التجريبية لمزيد من التحقق للنموذج المطور لتقييم الضغط الجانبي للخرسانة ذاتية الدمك والتنبؤ من سلوك التدفق أثناء الصب على نطاق كامل للبلطة.

المحاكاة عملت على نطاق كامل من صب البلاطة لدراسة تأثير المعاملات الريولوجية ومتغيرات الانسيابية على تدفق هذه المواد.

تم التحقق الناجح من صحة المحاكاة لديناميكيات السوائل الحسابية CFD وتنبؤات النموذج ذات العناصر المحدودة وظهر وجود علاقة جيدة مع نتائج التجارب التي أجريت وتلك من المسح السابق.

### **درجة الماجستير**

**جامعة الملك فهد للعلوم والبتروالمعادن  
الظهران 31261 – المملكة العربية السعودية**

# CHAPTER ONE

## INTRODUCTION

### 1.1 GENERAL

Various advantages are responsible for making concrete an efficient and durable construction material. The ease with which structural concrete elements can be formed into a variety of shapes and sizes, resistance to cyclic loading, good fire resistance, ease of maintenance, coupled with the fact that it is usually the cheapest and most readily available material are few reasons why concrete is widely adopted for construction purposes.

During the casting operation, traditional concrete has to be vibrated by means of external energy. For onsite casting conditions, where vibrating needles are the standard compaction equipment, the compaction operation quite often is not properly executed, or sometimes even completely neglected. As a consequence, this produces a concrete that has poor durability, and suffers from a much faster degradation. In addition, noisy environment due to vibration can lead to uncomfortable working conditions. In order to deal with these issues, self-compacting concrete (SCC) has been developed about two decades ago. This type of concrete more or less acts like a liquid, filling the complete formwork by gravity, without any external compaction energy. From a technological point of view, SCC has been developed as a result of applied nanotechnology [Dufour and Pijaudier-Cabot, 2005].

Due to the introduction of SCC the shape or form of the concrete element can be defined with more freedom [De Schutter, 2008]. However, fundamental knowledge concerning

the flow of SCC is needed to enable the engineer and the contractor answer the fundamental questions concerning the mix design and the casting or filling process of the formworks, with or without advanced pumping techniques. This knowledge is most appropriately gained through experience, experiment and simulation tools.

Computational modeling of flow could be used to simulate the total form filling and detailed flow behavior as particle migration and formation of granular arches between reinforcement (blocking). Moreover, computational modeling of flow could be a potential tool for understanding the rheological behavior of concrete and a tool for mix proportioning. This will result in tremendous progress in the correlation between mix proportioning and rheological parameters, thereby improving the entire approach to mix proportioning.

The rheological behavior of traditional concrete is mostly described by means of a Bingham model. However, in case of SCC some extra phenomena occur; like shear thickening and sometimes significant thixotropy [De Schutter and Audenaert, 2007]. In other words, this means that the apparent viscosity decreases over time at a constant shear rate and eventually steadies out to a constant value [Barnes, 1997]. This phenomenon happens because of presence of more ingredients, more complex mix design, and low yield stress and viscosity. Variations in properties (and robustness) are therefore associated to the specific effects of the ingredients on the rheological properties of the mixture, effects of the physical properties (i.e., size and specific density) of the aggregate, and the mixing history [Lange et al., 2008]. For instance, use of limestone powder, fly ash and silica fume affect the fresh and hardened properties of SCC [Bhattacharya et al., 2008]. In a study conducted by Cyr et al.(2000), it was reported that

the shear thickening is increased in the presence of metakaolin, ground quartz and fly ash have no effect on it, whereas silica fume reduces it.

The research outcome/conclusion will form the basic information for the hydrodynamic modeling of the flow of SCC as well as lead to improved guidelines for production of robust SCC using local materials in the Kingdom of Saudi Arabia.

## **1.2 RESEARCH SIGNIFICANCE**

In spite of the numerous uses of SCC in some parts of the world, it is still relatively new in Saudi Arabia. The few cases where SCC is used in the Kingdom include construction of ‘Al-Turky Business Park’ in which Riyadh aggregate was used. It was also used in ‘Al-Othman Tower’ project completed recently in Al-Khobar. This new age concrete is gaining recognition in the Kingdom and its use will become more popular in the future.

Several studies have been conducted in Saudi Arabia on self compacting concrete [Raza, 2006]. Most of these studies have addressed mix proportion, flowability, strength and shrinkage characteristics of SCC. The first study on rheology of SCC in the kingdom was carried out by Baluch et al. (2010) and Malik (2011) to determine the effect of different types of mineral admixtures, SCC rheology, aggregate gradation and volume fraction on flowability of SCC. Despite the growing awareness of the numerous advantages of SCC, no study related to the modeling of flow of SCC using local materials in its production has been carried out in the Kingdom. A need to study the behavior of this newly emerging concrete using simulation tools is, therefore, evident. Hence, this research work may serve as a pioneering work in the field of flow modeling of SCC and other fresh concretes in KSA.



Focusing on verifying the material constitutive behavior and flow characteristics, the numerical simulation of flow of SCC will provide insight into development of formwork pressure and pumpability of SCC, both issues of relevance to field applications including formwork design and pumping of SCC in moderate to high rise buildings.

This work will also create more awareness to the Kingdom's design and concrete construction industry about how simulation tools can be used to specify the required material fluidity for any specific work, thereby establishing confidence in its use. Also, bearing in mind that fewer number of tests, less amount of materials, and more simulation runs will be needed to achieve that, this will lead to considerable savings in time and costs on projects, and help to establish virtual simulation as a tool in the optimum design of SCC and other concrete mixes.

### **1.3 RESEARCH AIM AND OBJECTIVES**

The aim of the research project is the development and validation of the hydrodynamic modeling of the flow of SCC during the testing and casting processes. This will help in determining the effect of cement paste/mortar and SCC rheology on flowability attributes of SCC.

The primary objectives of this research work are as follows:

1. Computer/Numerical simulation of the SCC flow to verify its constitutive material behavior for each of the following SCC flow tests:
  - Slump Flow and T500 Test
  - L-box Test
  - V-funnel Test

2. Development of finite element model for lateral formwork pressure followed by numerical simulation using the same model to study the evolution of the pressure with time for several full-scale vertical walls.
3. Experimental program followed by a numerical simulation of full-scale casting of a slab as well as studying the effect of the rheological and thixotropic parameters on the casting process.

For validation of the model with respect to the objective one (1) above, experimental investigations were already carried out on SCC with various mix designs produced locally by Saudi Ready Mix, a leading supplier of SCC in the Kingdom [Baluch et al., 2010 and Malik, 2011] to determine the effect of different types of mineral admixtures, SCC rheology, aggregate gradation and volume fraction on flowability of SCC. However, the second and third objectives require conducting more experimental tests and utilizing some literature results.

Since the simulation adopted is based on single fluid approach, selection of the mixes modeled in this work is based on those in which segregation effect is absent (robust mixes) as observed during the already conducted experimental program in [Baluch et al., 2010 and Malik, 2011].

Some of the tests conducted under the aforementioned project include:

- Determination of rheological parameters of yield stress, viscosity and thixotropy of SCC for different mixes (made from Silica fume, Limestone powder, and Fly Ash) using ICAR Rheometer.
- Experimental investigation of the conventional flow and strength properties of concrete. The conventional flow was studied by carrying out the most

frequently applied testing methods as mentioned under item 1 above (Slump Flow and T500, L-box, and V-funnel Tests).

#### **1.4 SCOPE AND LIMITATIONS**

This study is limited to the following conditions:

- Use of continuum (single fluid) approach was made
- Effect of segregation was not studied since the research is geared towards modeling of robust SCC mixes in which segregation is absent
- The model is developed to study the flow behavior of SCC in a global scale. Hence, the micro or local behaviors were approximated

#### **1.5 RESEARCH METHODOLOGY**

The accomplishment of the aim and objectives of this research work requires eight major tasks to be completed as outlined in the phases below.

##### **1.5.1 Literature Review**

The literature review focusing on the characteristics & properties of SCC, review of rheological models governing flow of SCC and Computer-aided numerical simulation of SCC.

##### **1.5.2 Selection and Design of Concrete Mixes**

Two sources were used as the means to validate the proposed model simulations in this research: (i) Some experiments were conducted (ii) Already available literature

experimental data. However, from the data, mix design was undertaken on different types of SCC by varying the aggregate gradation, aggregate volume fraction and water-binder ratio. These mixes were identified in close collaboration with Saudi Ready Mix.

### **1.5.3 Casting of Slab and Vertical Wall**

Two boxes, one measuring 200cmX150cmX20cm and the other 100cmX100cmX30cm made of a combination of plywood and Plexiglas, were fabricated as molds for casting the vertical wall and slab respectively. In each case, one side is intentionally made with plexiglas in order to visually monitor the flow progress during the casting operation.

### **1.5.4 Selection of Software for Simulation**

The research was carried out on different types of SCC with various mix designs, by adopting the use of computational fluid dynamics (CFD) commercial software. An available numerical method was applied in order to develop a hydrodynamic modeling of the flow of SCC. This is available within the commercial software package FLUENT [Fluent Inc., 2003].

### **1.5.5 Development of Model**

The fresh concrete was considered as a homogeneous and incompressible fluid. Several aspects were studied in this context: the time-dependent thixotropic Bingham behavior and thixotropy, flow with free surface for most frequently applied testing methods for fresh SCC, interaction between the fluid (fresh concrete) and the formwork, and simulation of the real-life casting of both vertical wall and slab.

The Bingham behavior was modeled in the software package FLUENT by means of a Herschel-Bulkley viscosity model. However, as the flow process is evolving on a much

faster time scale than the hydration process, the thixotropy of SCC was programmed by means of a user-defined subroutine. To achieve that, the thixotropy model proposed by Roussel, (2006) was used.

#### **1.5.6 Simulation of the SCC Flow Tests**

This involves numerically simulating the following SCC flow tests using the model described in 1.5.5 above.

- Slump Flow & T500 Test
- L-box Test
- V-funnel Test

In order to accurately simulate the flow, free fluid surfaces were modeled. This was done by means of the VOF-technique (Volume of Fluid). The testing and casting processes were investigated and a validation of the hydrodynamic modeling was based on the position of the free surface. Based on the experimental results, the accuracy of the model was evaluated, and improvements were made.

#### **1.5.7 Simulation of SCC Casting and Formwork Pressure**

Unlike the simulation of the SCC tests, this is a replica of what happens in real-life castings of a slab thereby serving as a stronger tool to study how the SCC behaves in full scale casts. In addition, a finite element model was developed for a formwork pressure evolution in a vertical wall after casting. Numerical simulation was carried out using this model and the results verified by comparing with those from the conducted experiments and those from available literature.

### **1.5.8 Analysis of Simulation and Experimental Results**

Thorough analysis and discussion of the results achieved at the end of both the simulation and experiment was carried out.

## CHAPTER TWO

### LITERATURE REVIEW

#### 2.1 GENERAL

From the computational viewpoint, several researches have been carried out to model the flow of SCC using different approaches. Neglecting the presence of the rebars, as a first approximation, SCC flow can be considered as the flow of a single fluid thus rendering a discrete modeling approach unnecessary [Russel et al., 2007(a)].

Single fluid simulations have mostly been used to model the flow of fresh concrete during testing. However, a few examples of computational, modeling of full-scale castings assuming single fluid behavior can also be found in recent papers. The two main numerical difficulties in connection to single fluid simulations are the yield stress behavior of the material and the free surface displacement. It is the apparent viscosity of the material that is, most of time, applied in the Navier-Stoke's equations in order to obtain a numerical solution of the problem. [Russel et al., 2007(a)], however, reported that the apparent viscosity of a yield stress fluid approaches infinity when the shear rate approaches zero. They stressed the fact that, as a matter of necessity, this indetermination of the deformation state below the yield stress zones where flow stops or starts, which are most of the time the zones of interest should be avoided. Moreover, as continuum mechanics methods, single fluid simulation requires a clear definition of the boundary conditions.

The following areas are covered in this chapter.

- Simulation of the testing of fresh concrete

- Simulation of concrete casting
- Simulation of formwork pressure due to self compacting concrete

## 2.2 SIMULATION OF THE TESTING OF FRESH CONCRETE

Kulasegaram et al. (2010) used a lagrangian particle-based method, smooth particle hydrodynamics (SPH), to model the flow of SCC with or without short steel fibres. An incompressible SPH method was used to simulate the flow of such non-Newtonian fluids where they described its behavior by a Bingham-type model, in which the kink in the shear stress vs shear strain rate diagram was first appropriately smoothed out. The basic equations solved in the SPH were the incompressible mass conservation and Navier-Stokes equations. Their results demonstrated the capability of SPH and a proper rheological model to predict SCC flow and mould-filling behavior.

Figures 2.1 and 3.1 show the various stages during the numerical simulation of slump test of SCC without fibres and SCC flow with fibres, respectively as reported by Kulasegaram et al. (2010).

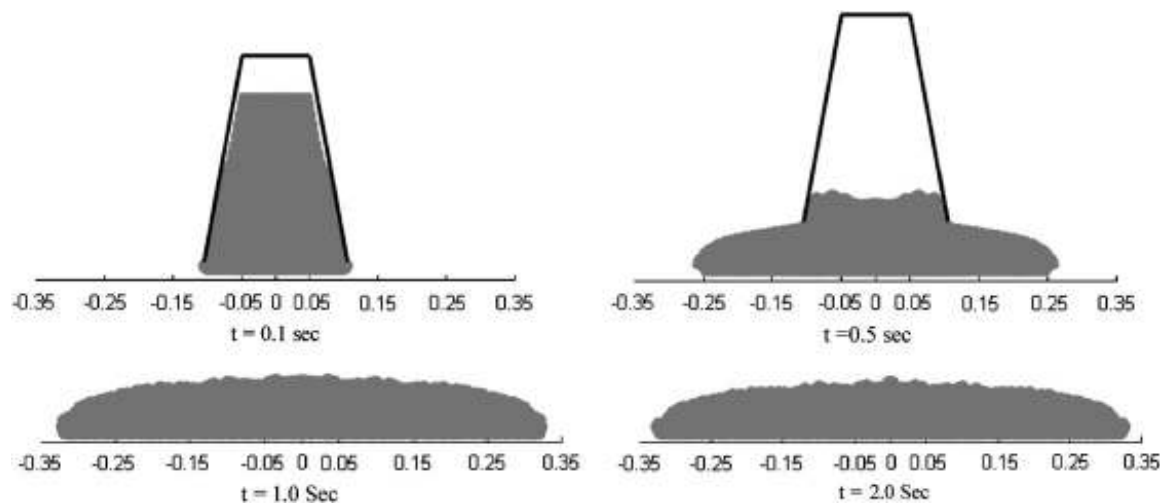


Figure 2.1: Axi-Symmetric Numerical Simulation of Slump Test for SCC Without Fibres [Kulasegaram et al., 2010].



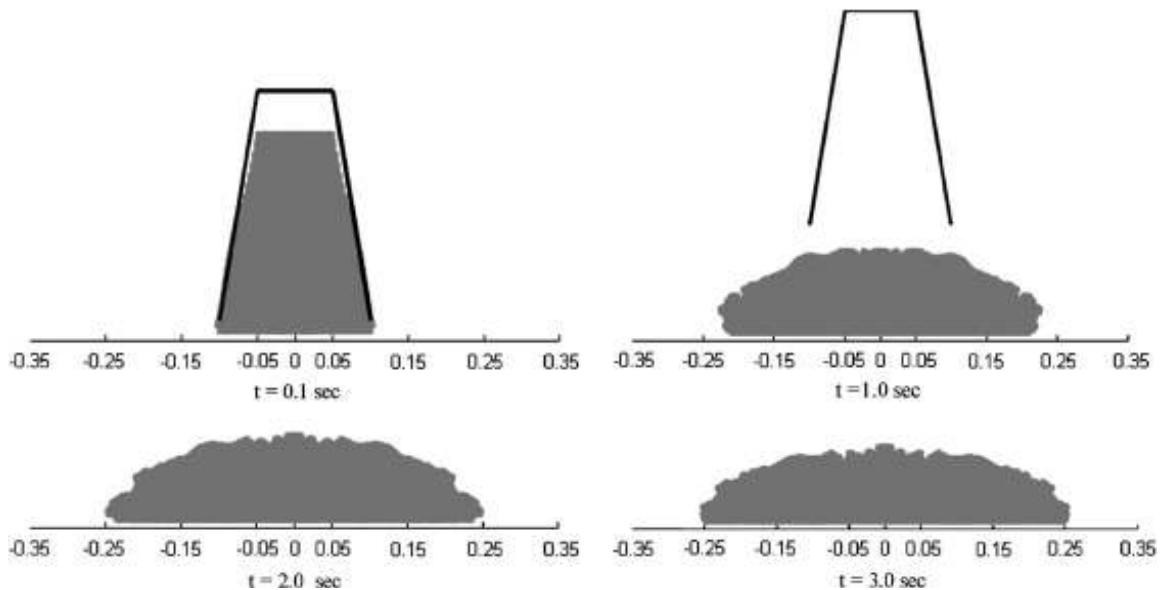


Figure 2.2: Axi-Symmetric Numerical Simulation of Slump Test for SCC With Fibres [Kulasegaram et al., 2010].

Viscoplastic Finite Element Method (VFEM) and the Viscoplastic Divided Element Method (VDEM) were used by Mori and Tanigawa (1992) to simulate flow of fresh concrete. Both the two approaches assume concrete as a homogeneous single fluid with given rheological properties. In VFEM the fresh concrete is divided into elements in which the deformation is calculated, and the flow is described by displacement of nodal points. In VDEM, space is divided into elements and cells, which are either empty or full, and the flow is described by the displacement of virtual markers. However, the fixed position of nodal points allows reinforcement and complicated boundary conditions to be simulated. Both methods were found applicable for simulation of various test methods and at reasonable computation time.

Dufour and Pijaudier-Cabot (2005) presented a numerical model aimed at simulating concrete flow based on homogeneous viscous fluid approach using a finite element method with Lagrangian integration points (FEM-LIP). They used Bingham's rheology for the fresh concrete behavior by considering three concretes, namely, one ordinary

concrete (OC), one high-performance concrete (HPC) and one self-compacting concrete (SCC) with contrasted rheologies.

On the material side, they identified Bingham's parameters on slump test (as the model calibration) using *ELLIPSES* code with a trial and error approach for the concretes considered. Since, their model assumed the fluid flow to be two-dimensional (2D), its consequences were investigated first and found to change value of the ratio slump/spreading compared to the axisymmetric case because the material can only flow in the plane of study on the contrary of the axisymmetric model where the material can flow radially. This resulted in nearly constant maximum shear stress for a given height and various spreadings, but changes a lot for a given spreading and different heights. As a result, they used the model for comparing only slumps between experiments, which are close to an axisymmetric geometry, and the numerical model but not the base spreading which was not sensitive on the shear stress. Part of their observation, also, was that the final slump is not affected by the plastic viscosity. So, the plastic viscosity given by the concrete formulation software *BETONLAB* which is based on the compressible packing model was used:

$$\mu = \exp\left(A \times \left(\frac{\Phi}{\Phi^*} - B\right)\right) \quad (2.1)$$

$$\tau_0 = \exp(a_0 + a_c K_c' + a_f K_f' + a_s K_s' + a_s K_s' + a_g K_g' + a_G K_G') \quad (2.2)$$

Where,

$\mu$  = Plastic viscosity

$\tau_0$  = Yield stress

$\Phi$  = Solid content of the concrete

$\Phi^*$  = packing density

A and B = Constants

$a's$  = Empirical parameters depending on grain size and on super-plasticizer quantity

$K'$  = Compaction index

Index  $c$  is related to cement,  $f$  to calcareous filler,  $s$  to powders with grains smaller than  $80\mu\text{m}$ ,  $S$  to sand grains,  $g$  to small aggregates and  $G$  to larger aggregates.

Regardless of error due to the 2D assumption, their numerical analysis of the slump test gave an estimation of the yield stress up to 2, 33 and 32% for OC, HPC and SCC, respectively.

With the use of this calibrated model, L-box tests were simulated and the flow speed and shape at stoppage measured. Their experimental data was found to be quite close to numerical predictions.

A typical output of the study carried out by [Dufour and Pijaudier-Cabot, 2005] is given in Figure 2.3 which shows different snapshots of the SCC flow in the L-box test for opening time of 1 s. Evolution in time of concrete height in different cross-sections for SCC flow in the L-box test is shown in Figure 2.4. Curves with a (‘) correspond to a Door Opening Time of 1 s and others to 0 s.

The computational fluid mechanics code Flow 3D® was used by Roussel (2004) to perform 3D simulations of different slump test methods (Figure 2.5). An elasto-viscoplastic model was used to describe the fluid behavior of concrete with yield stresses between 25 and 5500 Pa, assuming an incompressible and elastic solid up to the yield stress and a Bingham fluid beyond that as well as no sliding at the base. He was able to

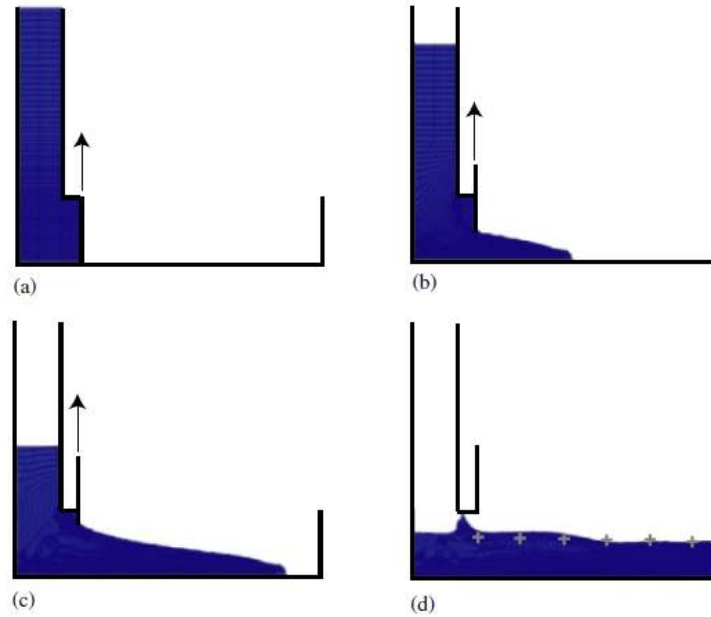


Figure 2.3: Figure 2.3: Different Snapshots of the L-box Test on SCC at Time (a) 0 s (b) 0.45 s (c) 0.85 s (d) 7.63 s with a Door Opening Time of 1 s [Dufour and Pijaudier-Cabot, 2005].

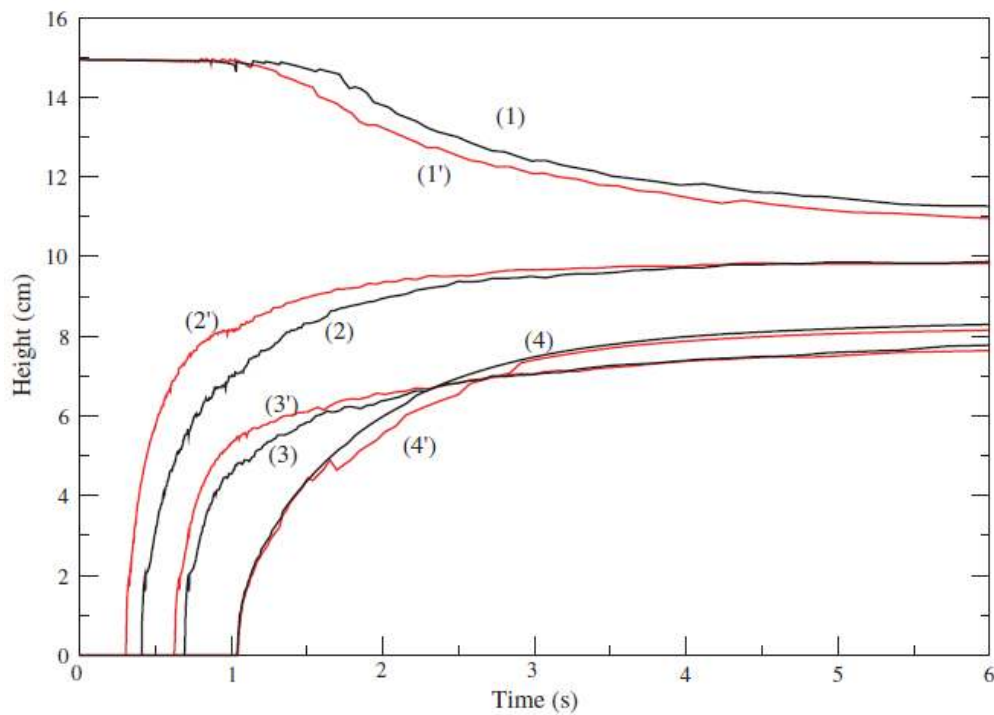


Figure 2.4: Evolution in Time of Concrete Height in Different Cross-Sections for SCC Flow in L-box Test [Dufour and Pijaudier-Cabot, 2005]: (1) At the Door Cross-Section; (2) and (3) At a Distance of 20 and 40 cm, respectively; and (4) At the end section.

achieve a good agreement between numerical and experimental results for the mini cone test and for the ASTM tests (Figure 2.6).

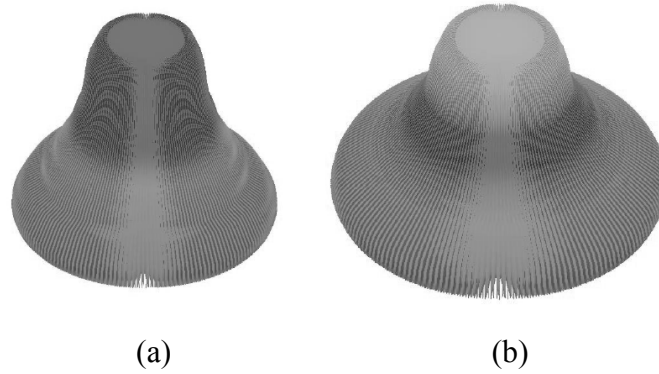


Figure 2.5: Examples of Obtained Shapes for the ASTM Cone [Roussel, 2004]  
 (a) Yield stress=2600 Pa (b) Yield stress = 2000 Pa.

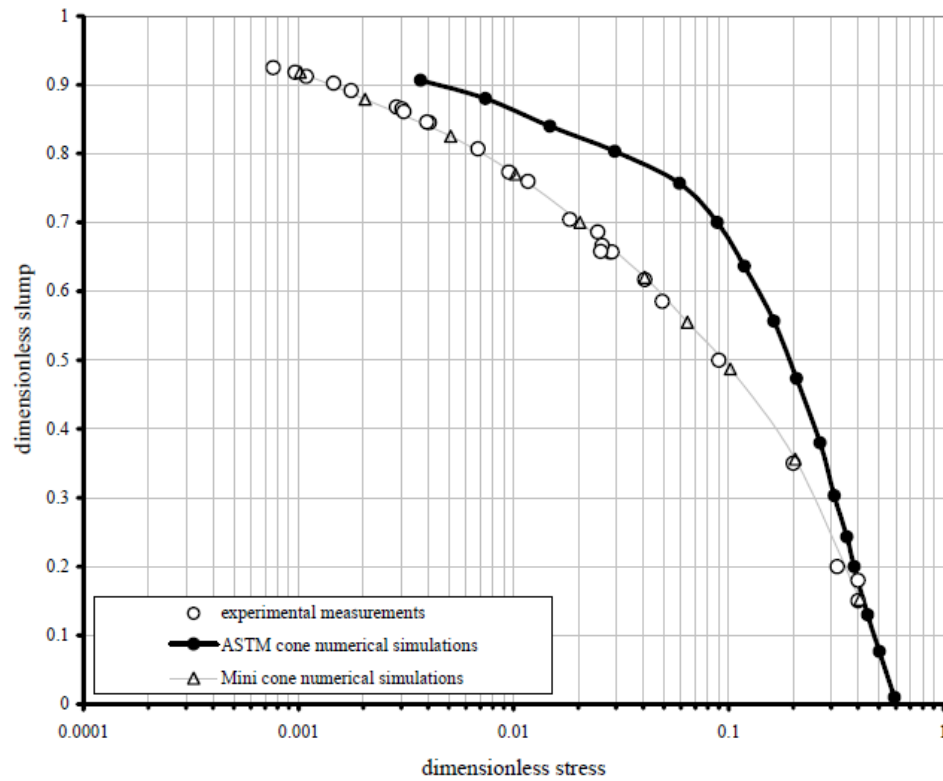


Figure 2.6: Slump in Terms of Yield Stress for ASTM Cone and Mini Cone [Roussel, 2004].

In [Thrane et al., 2004], simulation of SCC flow during L-box test was also based on a single fluid approach assuming Bingham behavior. The simulation approach was based

on the Galerkin FEM formulation of the Navier-Stokes' equation and included moving boundaries, and was undertaken by the code FIDAP. Combined simulations and experiments indicated that the flow in an L-box with reinforcement can be simulated assuming an ideal Bingham behavior and rheological properties measured in a BML rheometer. It was, however, necessary for them to include boundary conditions and to use a 3D model for simulating the flow in the L-box.

Wallevik (2003) gave a detailed description of numerical simulation of the flow in selected rheometers. His simulations are based on the assumption of a viscoplastic material, flowing either under steady state or time-dependent (transient) conditions. He used a combination of several different techniques to describe the viscoplastic behavior of the concrete. Using his own and freely available numerical software, he simulated velocity and shear stress profiles for various viscometer configurations. The computational modeling was used for the comparison of rheometers with regard to, among others, variations in shear rate and particle migration.

Gram (2009) investigated the numerical simulation of concrete flow using both discrete as well as continuous approaches. He used the discrete particle model as a means to simulate details and phenomena concerning aggregates modeled as individual objects. Spherical particles were used to achieve that. The continuous approach, on the other hand, has been used to simulate large volumes of concrete in the work. The concrete was modeled as a homogeneous material, but particular effects of aggregate, such as blocking or segregation were not accounted for in the continuous approach. This large scale quantitative analysis was performed rather smoothly with the continuous approach, whereas the smaller scale details and phenomena were better captured qualitatively with

the discrete particle approach. Good correspondence was achieved with a Bingham material model used to simulate concrete laboratory tests (e.g. slump flow, L-box) and form filling. Flows of concrete in a particularly congested section of a double-tee slab as well as two lifts of a multi-layered full scale casting were also simulated successfully.

### **2.3 SIMULATION OF CONCRETE CASTING**

To date, only limited research has been reported on simulation of SCC or any form of full-scale concrete casting.

Roussel et al., (2007(b)) applied numerical simulations to an industrial casting of a very high strength concrete pre-cambered composite beam. The results of the simulations carried out for various values of the rheological parameters (Bingham model) helped to determine the value of minimum fluidity needed to cast the element. The mix proportioning of the concrete was done keeping in mind this minimum value and the numerical predictions were finally compared with the experimental observations carried out during two trial castings and the real casting of the two 13m beams.

Although the assumptions needed to carry out the simulations may be over-simplistic (the rebars and possible thixotropy were not taken into account and only 2D simulations were carried out), a satisfactory agreement was found between the predicted and actual flow (Figure 2.8). Black shading emphasizes the casting defect on the upper left picture of Figure 2.8.

Although most of the applications deal with yield stress fluids, single fluid methods provide a large choice of behavior laws allowing the simulation of complex phenomena such as thixotropy. Roussel (2006) proposed a model derived from the Bingham model and able to describe the thixotropy of fresh concrete with only two additional parameters.



Figure 2.7: 2m Test Semi-Transparent Formwork [Roussel et al., 2007(b)].

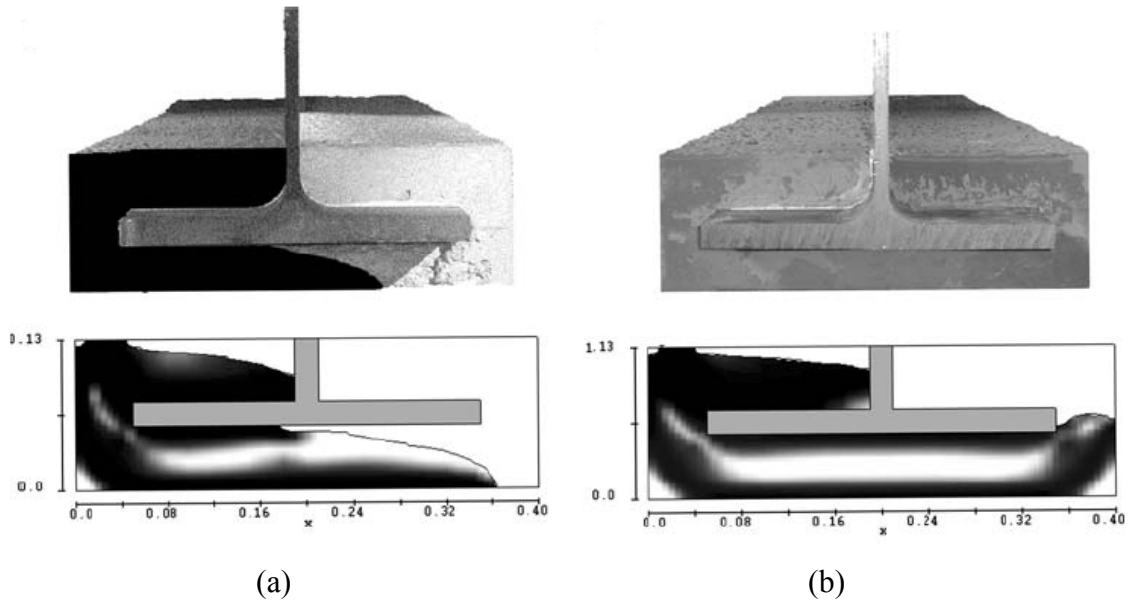


Figure 2. 8: Comparison between Experiments and Numerical Simulations for SCC with Yield Stresses equal to (a) 120 Pa and (b) 60 Pa [Roussel et al., 2007(b)].

The general form of the model is

$$\tau = (1 + \lambda)\tau_0 + k\dot{\gamma}^n \quad (2.3)$$



$$\frac{\partial \lambda}{\partial t} = \frac{1}{T \lambda^m} - \alpha \lambda \dot{\gamma} \quad (2.4)$$

Where  $\lambda$  is the flocculation (structuration) state of the concrete that evolves through the flow history and  $T$  (characteristic time of flocculation),  $m$  and  $\alpha$  (a destructuration parameter) are thixotropy parameters. The simplified version of the model assumes that the Bingham model is sufficient for the description of the steady state flow of fresh concrete:  $n=1$ ,  $k= \mu$  (plastic viscosity). It also assumes that the yield stress at rest increases as a linear function of time:  $m=0$ . This reduces the model to the form

$$\tau = (1 + \lambda)\tau_0 + \mu \dot{\gamma} \quad (2.5)$$

$$\frac{\partial \lambda}{\partial t} = \frac{1}{T} - \alpha \lambda \dot{\gamma} \quad (2.6)$$

It is also assumed that the characteristic time of flocculation ( $T$ ) is long compared to the characteristic time of de-flocculation. So,

$$\frac{\partial \lambda}{\partial t} \approx -\alpha \lambda \dot{\gamma} \quad (2.7)$$

On integration,

$$\lambda = \lambda_0 e^{-\alpha \dot{\gamma} t} \quad (2.8)$$

$$\tau = (1 + \lambda_0 e^{-\alpha \dot{\gamma} t})\tau_0 + \mu \dot{\gamma} \quad (2.9)$$

$$\tau_0(t) = (1 + \lambda_0)\tau_0 = \tau_0 + \tau_0 \left( \frac{t}{T} \right) = \tau_0 + A_{\text{thix}} t \quad (1)$$

$$\text{With } A_{\text{thix}} = \frac{\tau_0}{T} \quad (2.11)$$

Where  $A_{\text{thix}}$  is the re-structuration (flocculation) rate (Pa/s) of the SCC at rest and

$$\lambda_0 = \lambda(\dot{\gamma} = 0).$$

A classification of SCC based on their flocculation rate  $A_{thix}$  has been proposed as shown in Table 2.1.

Table 2.1: Classification of SCC According to their Flocculation Rate  $A_{thix}$  [Roussel 2006].

$A_{thix}(\text{Pa/s})$	SCC type
$A_{thix} < 0.1$	Non-Thixotropic
$0.1 \leq A_{thix} \leq 0.5$	Thixotropic
$A_{thix} > 0.5$	Highly Thixotropic

This model was used to study the following two phenomena:

- During placing, the fresh SCC behaves as a fluid but, if cast slowly enough or if at rest, it flocculates and builds up an internal structure and has the ability to withstand the load from concrete cast above it without increasing the lateral stress against the formwork.
- During placing, a layer of SCC often has a short time to rest and flocculate before a second layer of concrete is cast above it. If the fine particles flocculate too much and the apparent yield stress of the concrete increases above a critical value, the two layers do not combine at all and a weak interface is formed (Figure 2.9 (b)), in view of the elimination of vibration in the casting of SCC.

It can be observed from Figure 2.9 that for a 5-min resting time, the two layers mix perfectly. On the other hand, for a 20-min resting time, the two layers do not mix at all.

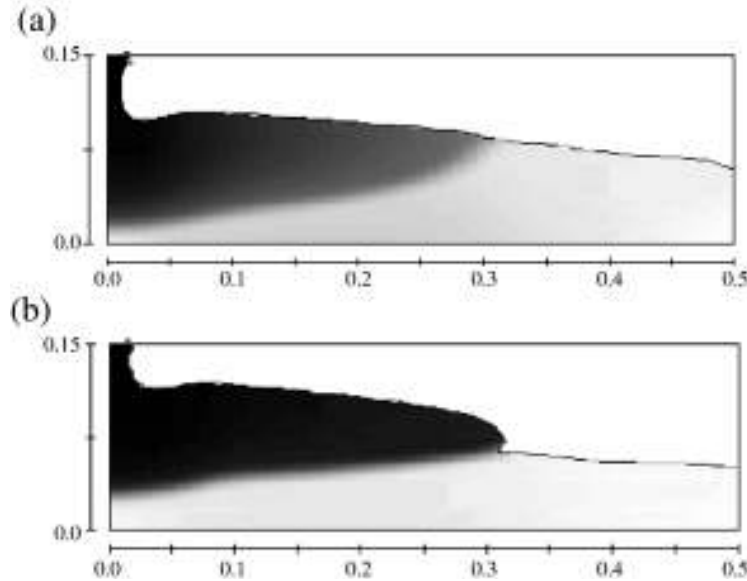


Figure 2.9: Numerical Simulations of the Multi-Layer Casting Phenomenon with  $\tau_0 = 50 \text{ Pa}$ ,  $\mu_p = 50 \text{ Pa s}$ ,  $A_{\text{thix}} = 0.5 \text{ Pa/s}$ ,  $\alpha=0.005$ . (a) 5-min resting time (b) 20-min resting time [Roussel, 2006].

## 2.4 SIMULATION OF FORMWORK PRESSURE DUE TO SELF COMPACTING CONCRETE

One of the setbacks to the high flowability of this material is mostly attributed to the significant increase in the lateral pressure exerted on formwork. As reported by many researchers, the formwork pressure due to SCC can be as high as the hydrostatic pressure. As a result, SCC needs a stronger formwork that can resist the higher lateral pressure than cases that use ordinary concrete [Kim et al., 2011]. Hence, the economical and safe design of these formworks may be affected.

Results from various authors, however, reported that when adjustments are made in the concrete mix design and casting operations the developed lateral pressure can be lower than the hydrostatic pressure. Kim et al. (2011) reported that the reduction in formwork pressure can be increased by incorporating chemical and mineral admixtures, such as viscosity-modifying admixtures. Varying the amounts of these new materials will result

in the variation of thixotropic properties and behavior of SCC. With regards to the influence of casting process, Ovalez and Roussel (2005) explained that during placing, the material behaves as a fluid but, if cast slowly enough or if at rest it builds up an internal structure and has the ability to withstand the load from concrete cast above it without increasing the lateral stress against the formwork. Good recommendations on the measurement systems for determining formwork pressure of SCC were provided by Khayat and Assaad (2007).

To explore more into the lateral formwork pressure evolution and the likely factors affecting it more researches (both experimental and numerical) are needed in addition to the existing ones. However, the importance of the latter is highly an invaluable one since they form the basis upon which likely future researches will be built on.

Gregori et al. (2008) planned and developed an experimental program for simulation of self-consolidating concrete formwork pressure. They developed a laboratory device to study the effects of casting rate and mixture composition by pressurizing a volume of material inside a cylinder and recording the lateral pressure evolution. Columns heights up to 14 m were simulated using this approach for two different rates of casting. Their results proved that it is possible to achieve a formwork pressures less than hydrostatic.

Figure 2.11 compares the evolution of the total and pore water pressure for a column in which the load was applied instantaneously (that is, extremely fast casting rate) as studied by Gregori et al. (2008).

Assaad and Khayat (2006) studied the effect of a mixture's consistency on the lateral pressure that can be developed by highly flowable concrete. Use was made of high-range water-reducing admixtures to study their effect. They found that concretes with lower

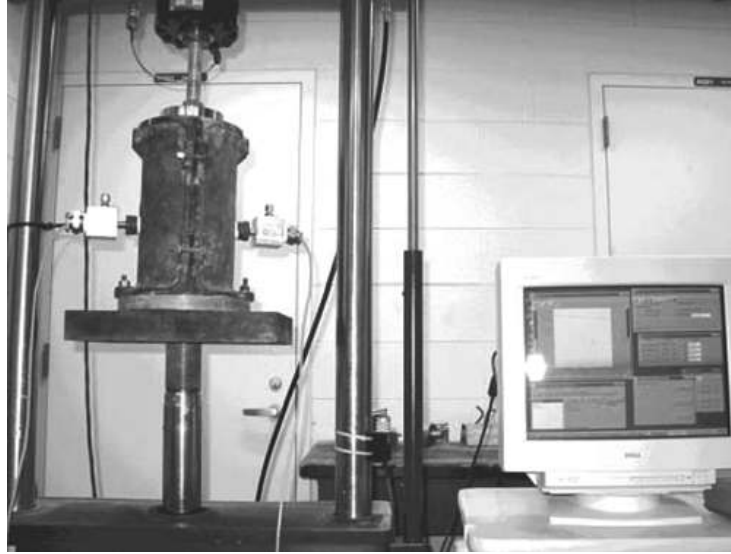


Figure 2.10: Hydraulic Press and System of Automatic Data Acquisition [Gregori et al. (2008)].

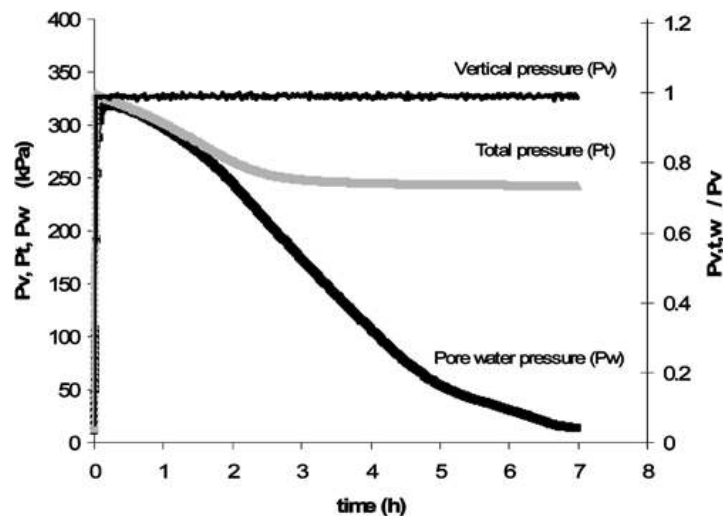


Figure 2.11: Instantaneous Simulation of 14 m High Concrete Column [Gregori et al., 2008].

consistency exert lower initial lateral pressure and had faster rates of pressure drop with time (Figure 2.12). They attributed this to the increased degree of shear strengths that enables the fresh concrete to further resist vertical stresses, hence precluding the development of high lateral pressure.

Other researches made to study the behavior of formwork pressure due to variation of internal and/or external factors on this highly flowable material have been reported by

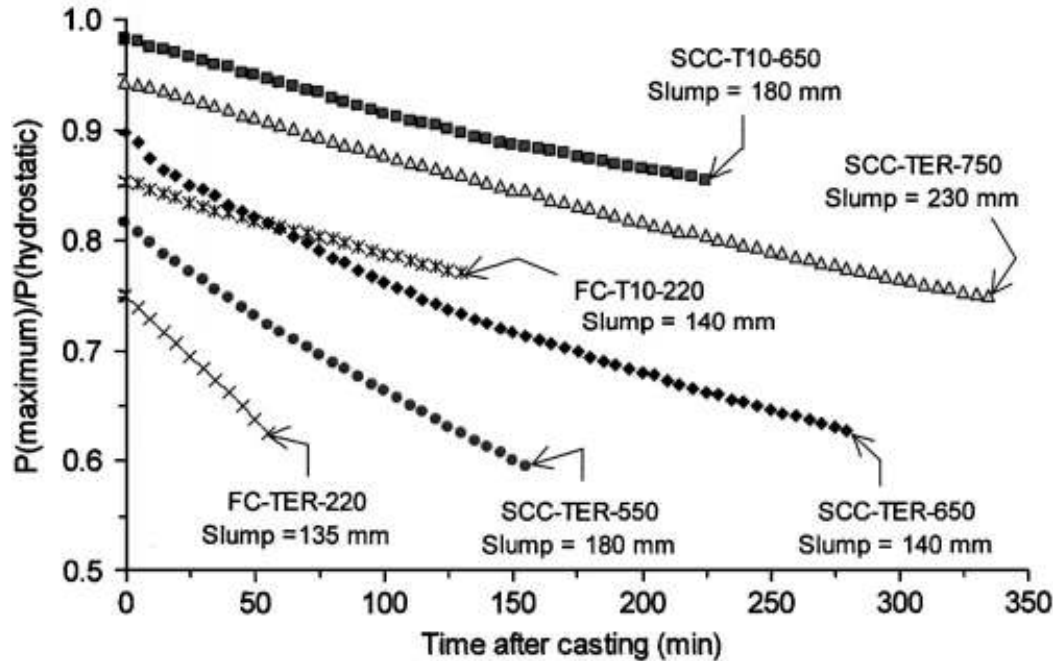


Figure 2.12: Effect of Mixture Consistency on  $P_{\text{max}}/P_{\text{hyd}}$ . Values Determined on the 2.8m High Experimental Column [Assaad and Khayat (2006)].

Assaad et al. (2003), Khayat and Assaad (2008), Kim et al. (2010), Andriamanantsilavo and Amziane (2004), Khayat et al. (2005), Kwon et al. (2010), Vanhove et al. (2003).

Although developed mainly for conventional concrete, however, the finite element model reported by Gallego et al. (2010) for assessing the lateral formwork pressure exerted by a concrete particularly with respect to tall formworks provided promising results. They confirmed this by a preliminary validation of the model using experimental values obtained by Arslan et al. (2005). Incorporated in their model were some fresh concrete mechanical parameters such as the angle of internal friction, cohesion, dilatancy, modulus of elasticity, Poisson coefficient and concrete-to-wall friction coefficient.

Gallego et al. (2011) developed a three-dimensional numerical model with the ANSYS finite element software package, which simulates the behavior of fresh concrete and formwork walls to obtain the resulting pressures in complex-shaped formworks. Based

on the results obtained from their model they highlighted the influence of the inclination of a formwork on the lateral pressures exerted on its walls by fresh concrete. Easier examination of the load distributions in complex-shaped formworks was made possible by their proposed computer model, which is not contemplated in current standards.

Figure 2.14 shows the distribution curves reported by Gallego et al. (2011) for the pressure exerted by the fresh concrete against the formwork wall in the central section of the bridge deck section shown in Figure 2.13. The results obtained with their numerical models show that the maximum foreseeable pressures are below those suggested by the international standards for formwork calculation (Figure 2.14).

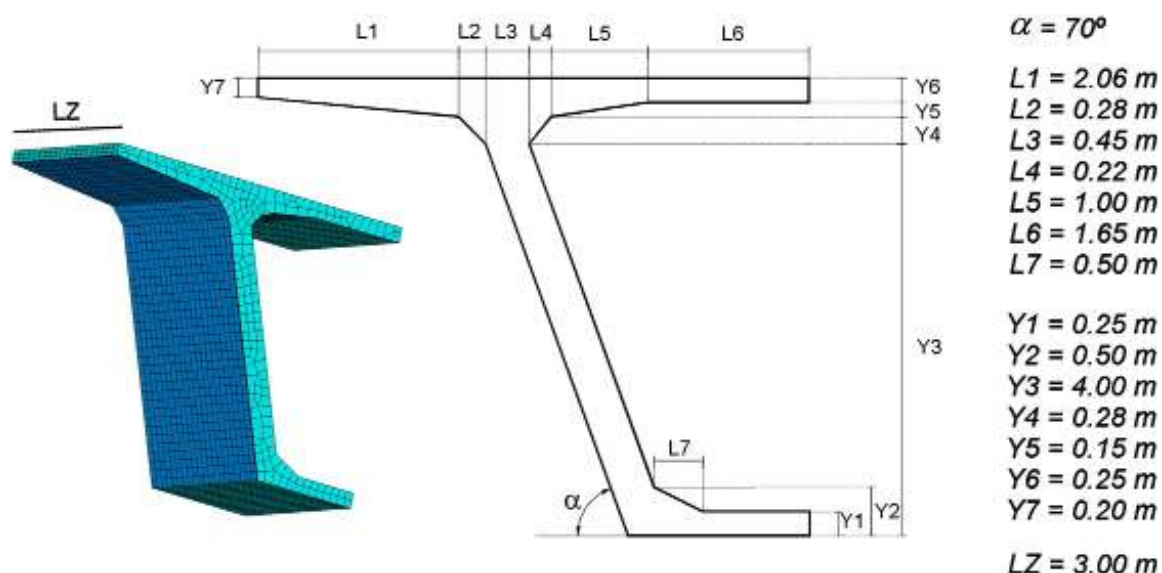


Figure 2.13: Shape of the Formwork Considered for Analyses [Gallego et al. (2011)].

Ovalez and Roussel (2006) presented a physical model for lateral stress exerted by SCC and justified its physical meaning based on a theoretical point of view. Their approach considered that SCC is characterized by yield stress  $\tau_0$  (an increasing function of the

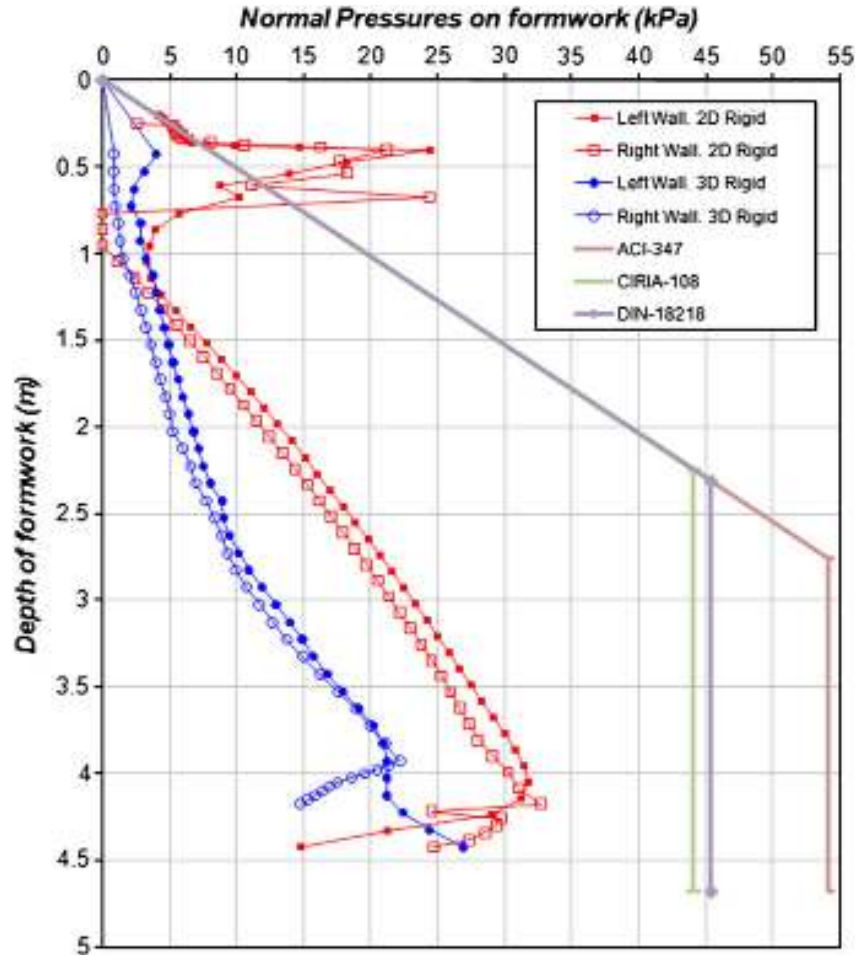


Figure 2.14: Comparison of Lateral Pressures obtained with the 2-D and 3-D Numerical Models and the Equations of the Current Standards [Gallego et al. (2011)].

resting time). They simplified the problem by using Tresca criterion as the yield criterion (with  $\tau_0$  as the maximum shear stress sustainable by an internal plane). Thus, treating the SCC as an elastic material below this stress level they started with the basic elastic theory, which gives a linear relation between the stress tensor components  $\sigma_{ij}$  and the strain tensor components  $\varepsilon_{ij}$  as follows

$$E\varepsilon_{ij} = (1 + \nu_p)\sigma_{ij} - \nu_p\delta_{ij}\sigma_{kk} \quad (2.12)$$

Where, E is the young modulus, and  $\nu_p$  the Poisson ratio.



In the geometry of the formwork considered by Ovarlez and Roussel (2006), they used the coordinates  $x$  in the width direction,  $y$  in the thickness direction; the vertical direction  $z$  is oriented downwards. The top surface is the plane  $z = 0$ ; the walls are the planes  $x = L/2$  and  $y = e/2$ .

Finally, they showed that the expression for the maximum pressure during casting can be written as follows.

For a rectangular formwork of width  $e$

$$\sigma_{xx} = \sigma_{yy} = K \left( \rho g H - \frac{(H - e) A_{thix}}{eR} \right) \quad (2.13)$$

For a circular column of radius  $r$

$$\sigma_{xx} = \sigma_{yy} = K \left( \rho g H - \frac{(H - r)^2 A_{thix}}{rR} \right) \quad (2.14)$$

Where  $A_{thix}$  is the flocculation coefficient,  $\rho$  is the mass density of SCC and  $K$  is the ratio of horizontal to vertical stresses. They showed that in the case of SCC  $K$  value is near 1 ( $K=0.97$  and  $0.945$  for the air contents of 2% and 4% respectively).

Validation of their above proposed model was achieved using results published by Billberg (2003) and Khayat et al. (2005) (Figure 2.15). Figure 2.15 shows the existence of two regimes as reported by Ovarlez and Roussel (2006); the casting rate plays a significant role on the variation of the relative lateral stress within the first regime, whereas the second regime shows negligible effect of this parameter.

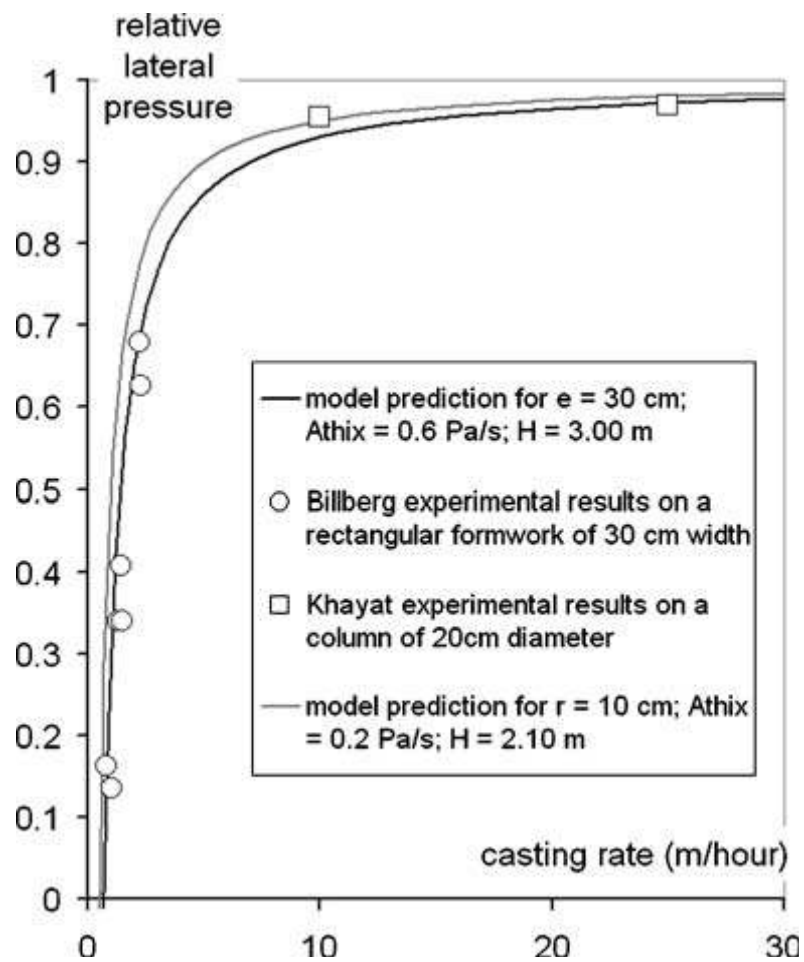


Figure 2.15: Comparison between Experimental Results and Predictions by Eqs. 2.2 and 2.3 in the Case of a Rectangular Formwork and a Column [Ovalez and Roussel, 2006].

# **CHAPTER THREE**

## **PRINCIPLES OF COMPUTATIONAL FLUID DYNAMICS (CFD) AND EQUATIONS GOVERNING THE MOTION OF A FLUID**

### **3.1 NAVIER-STOKES AND CONTINUITY EQUATIONS FOR INCOMPRESSIBLE FLOW IN CARTESIAN COORDINATES**

Analysis of most fluids' flow can be achieved using two equations. The first, referred to as the Continuity Equation, requires that the mass of fluid entering a fixed control volume either leaves that volume or accumulates within it. In other words, it is a "mass balance" requirement posed in a mathematical form, and is a scalar equation. The other governing equation is the Momentum Equation, or Navier-Stokes Equation. Named after Claude-Louis Navier and George Gabriel Stokes, the Navier–Stokes equations describe the motion of fluid substances. These equations arise from applying Newton's second law to fluid motion, together with the assumption that the fluid stress is the sum of a diffusing viscous term (proportional to the gradient of velocity), plus a pressure term.

The Navier-Stokes equations dictate not position but rather velocity. A solution of the Navier-Stokes equations is called a velocity field or flow field, which is a description of the velocity of the fluid at a given point in space and time. Once the velocity field is solved for, other quantities of interest (such as flow rate or drag force) may be found.

This is different from what is normally seen in classical mechanics, where solutions are typically trajectories of position of a particle or deflection of a continuum. Studying velocity instead of position makes more sense for a fluid, however for visualization purposes one can compute various trajectories.

There are many methods to derive these equations. However, a *control volume approach* is used here to demonstrate the origin of each term. These equations are extremely difficult to solve in their raw form. The Navier-Stokes equations are second order, non-homogenous, non-linear partial differential equations that require at least two boundary conditions for solution. Most solutions that exist are for highly simplified flow situations where certain terms in the equations have been eliminated through some rational process.

### 3.1.1 Derivation of the Continuity Equation

Consider a small, fixed volume of fluid of lengths  $\Delta x$ ,  $\Delta y$  and  $\Delta z$  somewhere in the middle of a flow stream (Figure 3.1).

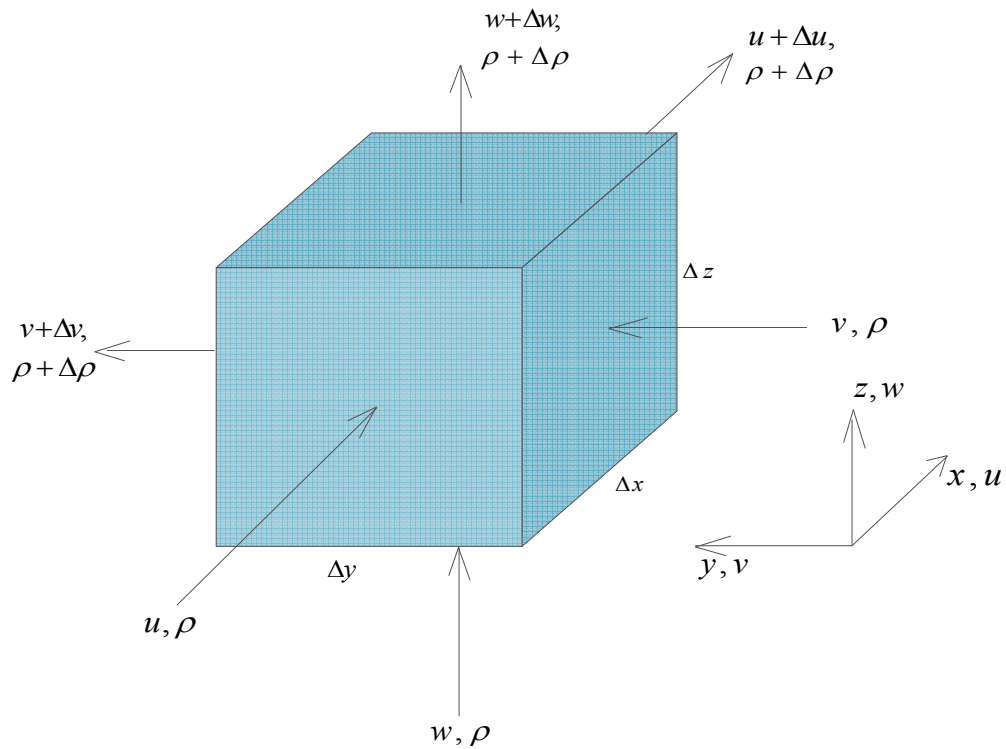


Figure 3.1: Elemental Fluid Volume for Derivation of the Fluid Equations in Cartesian Coordinates.

These lengths are short enough so that changes in all fluid properties across the volume may be well approximated with linear functions. On the other hand, these dimensions must be large enough so that the fluid may be considered as a continuum (i.e., much larger than the molecular scale). The mass of fluid in this elemental volume depends on the amount of fluid entering and leaving through the faces. The difference between these two is the rate of mass that accumulates in the volume. The rate of mass entering a face is the product of the density, the fluid velocity and the face area.

The mass flux entering the volume through the face perpendicular to the x-direction is

$$\text{Mass flux in} = \rho u \Delta y \Delta z \quad (3.1)$$

The mass leaving the volume on the opposite side of the volume is again the product of density, velocity and area. The mass flux leaving that face is thus

$$\text{Mass flux out} = -(\rho + \Delta\rho)(u + \Delta u) \Delta y \Delta z \quad (3.2)$$

Where  $\Delta\rho$  and  $\Delta u$  are the small changes in the density and velocity as the fluid passed through the volume. The negative sign signifies the fact that the mass is leaving the control volume. Performing the same analysis on the mass entering the volume through the other faces of the volume results in the following

$$\text{y-direction, Mass flux in} = \rho v \Delta x \Delta z \quad (3.3)$$

$$\text{z-direction, Mass flux in} = \rho w \Delta x \Delta y \quad (3.4)$$

where  $v$  and  $w$  are the velocities in  $y$  and  $z$  directions respectively. Similarly, the mass fluxes leaving the volume on the opposite faces are

$$\text{y-direction, Mass flux out} = -(\rho + \Delta\rho)(v + \Delta v)\Delta x\Delta z \quad (3.5)$$

$$\text{z-direction, Mass flux out} = -(\rho + \Delta\rho)(w + \Delta w)\Delta x\Delta y \quad (3.6)$$

All of these added together must equal the mass of fluid accumulating in the volume,  $\Delta x\Delta y\Delta z$ . This mass is given by,

$$\text{Mass accumulating} = \left(\frac{\Delta\rho}{\Delta t}\right)\Delta x\Delta y\Delta z \quad (3.7)$$

Putting all of these together, we have

$$\begin{aligned} \left(\frac{\Delta\rho}{\Delta t}\right)\Delta x\Delta y\Delta z = & \rho u\Delta y\Delta z + \rho v\Delta x\Delta z + \rho w\Delta x\Delta y - (\rho + \Delta\rho)(u + \Delta u)\Delta y\Delta z \\ & - (\rho + \Delta\rho)(v + \Delta v)\Delta x\Delta z - (\rho + \Delta\rho)(w + \Delta w)\Delta x\Delta y \end{aligned} \quad (3.8)$$

Multiplying out the quantities in the parentheses and neglecting terms with at least four products of the quantities in  $\Delta$  results in

$$\left(\frac{\Delta\rho}{\Delta t}\right)\Delta x\Delta y\Delta z = -(u\Delta\rho + \rho\Delta u)\Delta y\Delta z - (\rho\Delta v + v\Delta\rho)\Delta x\Delta z - (\rho\Delta w + w\Delta\rho)\Delta x\Delta y \quad (3.9)$$

or

$$\left(\frac{\Delta\rho}{\Delta t}\right)\Delta x\Delta y\Delta z = -\Delta(\rho u)\Delta y\Delta z - \Delta(\rho v)\Delta x\Delta z - \Delta(\rho w)\Delta x\Delta y \quad (3.10)$$

Dividing both side by  $\Delta x\Delta y\Delta z$  and rearranging, yields

$$\frac{\Delta\rho}{\Delta t} + \frac{\Delta(\rho u)}{\Delta x} + \frac{\Delta(\rho v)}{\Delta y} + \frac{\Delta(\rho w)}{\Delta z} = 0 \quad (3.11)$$

Taking the limit as  $\Delta t$  tends to 0, the above equation can be written as

$$\frac{\partial\rho}{\partial t} + \frac{\partial(\rho u)}{\partial x} + \frac{\partial(\rho v)}{\partial y} + \frac{\partial(\rho w)}{\partial z} = 0 \quad (3.12)$$

Where the partial derivatives,  $\frac{\partial}{\partial t}$ , are used because the function (velocity or density) depends on several variables (3 position or spatial variables and time). It should be noted that in this equation, the density and velocities are still functions of the spatial coordinates  $x, y$  and  $z$ .

For an incompressible fluid, the density will be constant and, hence, the Continuity Equation becomes

$$\frac{\partial u}{\partial x} + \frac{\partial v}{\partial y} + \frac{\partial w}{\partial z} = 0 \quad (3.13)$$

### 3.1.2 Derivation of the Momentum (Navier-Stokes) Equations

Starting with the same small, fixed volume of fluid somewhere in the middle of a flow stream with sides of lengths  $\Delta x, \Delta y$  and  $\Delta z$  (Figure 3.1): The law of the conservation of momentum states that the rate of change of momentum in the control volume must equal the net momentum flux into the control volume plus any external forces acting on the control volume. The derivation will be based on the momentum in the  $x$  direction.

Similar derivations may be shown for the y and z direction. Hence, there are three different momentum equations that together comprise the Navier-Stokes Equations.

### 3.1.2.1 Momentum Change and Flux

The time rate of change of momentum within the control volume is

$$\frac{\partial p}{\partial t} = \frac{\partial}{\partial t} (\rho u) \Delta x \Delta y \Delta z \quad (3.14)$$

The flux of momentum in the x direction into each face of the control volume is the product of the mass flux per unit area,  $mf$  multiplied by  $\Delta A$  and the x direction velocity,

$$\text{Momentum flux} = mf \times u \Delta A \quad (3.15)$$

Where,  $\Delta A$  is the surface area. For the side in the negative x-direction, the momentum flux is thus

$$x \text{ momentum flux in} = \rho u u \Delta y \Delta z \quad (3.16)$$

The momentum flux out the opposite side is

$$x \text{ momentum flux out} = -(\rho u u + \frac{\partial}{\partial x} (\rho u u) \Delta x) \Delta y \Delta z \quad (3.17)$$

The momentum flux into the face with normal vector in the negative y direction is

$$y \text{ momentum flux in} = \rho v u \Delta x \Delta z \quad (3.18)$$

For the face opposite, the momentum flux out is



$$y \text{ momentum flux out} = -(\rho v u + \frac{\partial}{\partial y}(\rho v u)\Delta y)\Delta x\Delta z \quad (3.19)$$

Using a similar analysis, it can be shown that the momentum flux into and out of the faces with normal vectors in the z direction are, respectively,

$$z \text{ momentum flux in} = \rho w u \Delta x \Delta y \quad (3.20)$$

and

$$z \text{ momentum flux out} = -(\rho w u + \frac{\partial}{\partial z}(\rho w u)\Delta z)\Delta x \Delta y \quad (3.21)$$

As expressed in the law of conservation of momentum, the momentum equation comes from adding all of these terms together.

$$\begin{aligned} \frac{\partial(\rho u)}{\partial t} \Delta x \Delta y \Delta z = & \rho u u \Delta y \Delta z - (\rho u u + \frac{\partial}{\partial x}(\rho u u)\Delta x)\Delta y \Delta z + \rho v u \Delta x \Delta z \\ & - (\rho v u + \frac{\partial}{\partial y}(\rho v u)\Delta y)\Delta x \Delta z + \rho w u \Delta x \Delta y - (\rho w u + \frac{\partial}{\partial z}(\rho w u)\Delta z)\Delta x \Delta y + \sum F_x \end{aligned} \quad (3.22)$$

Where,  $\sum F_x$  is the sum of the external forces on the control volume. Expanding the terms in the bracket and rearranging gives

$$\sum F_x = (\frac{\partial(\rho u)}{\partial t} + \frac{\partial}{\partial x}(\rho u u) + \frac{\partial}{\partial y}(\rho v u) + \frac{\partial}{\partial z}(\rho w u))\Delta x \Delta y \Delta z \quad (3.23)$$

Using the product rule, the momentum change and fluxes can be expanded to

$$\begin{aligned} \sum F_x = & \left( \rho \frac{\partial u}{\partial t} + \rho u \frac{\partial u}{\partial x} + \rho v \frac{\partial u}{\partial y} + \rho w \frac{\partial u}{\partial z} + u \frac{\partial \rho}{\partial t} + u \frac{\partial(\rho u)}{\partial x} \right. \\ & \left. + u \frac{\partial(\rho v)}{\partial y} + u \frac{\partial(\rho w)}{\partial z} \right) \Delta x \Delta y \Delta z \end{aligned} \quad (3.24)$$

Identifying the last four terms in parentheses as the continuity equation (which must be zero) times u, leaves

$$\sum F_x = \left( \rho \frac{\partial u}{\partial t} + \rho u \frac{\partial u}{\partial x} + \rho v \frac{\partial u}{\partial y} + \rho w \frac{\partial u}{\partial z} \right) \Delta x \Delta y \Delta z \quad (3.25)$$

In the same manner the forces in the y and z directions can be obtained thus:

$$\sum F_y = \left( \rho \frac{\partial v}{\partial t} + \rho u \frac{\partial v}{\partial x} + \rho v \frac{\partial v}{\partial y} + \rho w \frac{\partial v}{\partial z} \right) \Delta x \Delta y \Delta z \quad (3.26)$$

$$\sum F_z = \left( \rho \frac{\partial w}{\partial t} + \rho u \frac{\partial w}{\partial x} + \rho v \frac{\partial w}{\partial y} + \rho w \frac{\partial w}{\partial z} \right) \Delta x \Delta y \Delta z \quad (3.27)$$

### 3.1.2.2 Derivation of Forces

There are two types of forces to be included: body forces and surface forces. Body forces act on the entire control volume. The most common body force is that due to gravity. The body force due to gravity is the component of the acceleration due to gravity in the x-direction ( $g_x$ ) times the mass of the fluid control volume (density times volume), or

$$F_b = g_x \rho \Delta x \Delta y \Delta z \quad (3.28)$$

Surface forces act on only one particular surface of the control volume at a time, and arise due to pressure or viscous stresses. The stress on a surface of the control volume

acts in the outward direction, and is given the symbol  $s_{ij}$ , with two subscripts. The first subscript  $i$  indicates the normal direction of the face on which the stress acts, while the second subscript  $j$  indicates the direction of the stress. The force due to the stress is the product of the stress and the area over which it acts. Thus, on the faces with normals in the  $x$ -direction ( $\Delta y \Delta z$ ), the forces acting in the  $x$ -direction due to the direct stresses are

$$F_{b-x}^{in} = -\sigma_{xx} \Delta y \Delta z \quad \text{and} \quad F_{b-x}^{out} = (\sigma_{xx} + \frac{\partial \sigma_{xx}}{\partial x} \Delta x) \Delta y \Delta z \quad (3.29)$$

The sum of these two forces is

$$F_{b-x} = \frac{\partial \sigma_{xx}}{\partial x} \Delta x \Delta y \Delta z \quad (3.30)$$

Similarly, on the faces with normals in the  $y$ -direction ( $\Delta x \Delta z$ ), the forces in the  $x$ -direction due to shear stresses sum to

$$F_{b-y} = \frac{\partial \sigma_{yx}}{\partial y} \Delta x \Delta y \Delta z \quad (3.31)$$

and on the faces with normals in the  $z$ -direction ( $\Delta x \Delta y$ ), the forces in the  $x$ -direction due to shear stresses sum to

$$F_{b-z} = \frac{\partial \sigma_{zx}}{\partial z} \Delta x \Delta y \Delta z \quad (3.32)$$

The sum of all surface forces in the  $x$ -direction is thus,

$$F_{b-x}^{sum} = \left( \frac{\partial \sigma_{xx}}{\partial x} + \frac{\partial \sigma_{yx}}{\partial y} + \frac{\partial \sigma_{zx}}{\partial z} \right) \Delta x \Delta y \Delta z \quad (3.33)$$

The stress  $\sigma_{xx}$  includes the pressure  $p$  (acting inward, and, hence, has a negative sign) and the normal viscous stress  $\tau_{xx}$ . The stresses  $\sigma_{yx}$  and  $\sigma_{zx}$  include only viscous shearing stresses  $\tau_{yx}$  and  $\tau_{zx}$ . This gives the force in the x-direction as

$$F_{b-x}^{sum} = \left( -\frac{\partial p}{\partial x} + \frac{\partial \tau_{xx}}{\partial x} + \frac{\partial \tau_{yx}}{\partial y} + \frac{\partial \tau_{zx}}{\partial z} \right) \Delta x \Delta y \Delta z \quad (3.34)$$

### 3.1.2.3 Newtonian/Non-Newtonian Fluids

A Newtonian fluid is one in which the viscous stress is linearly proportional to the rate of deformation ( $\tau \sim \frac{\partial u}{\partial y}$ ). The constant of proportionality is the viscosity,  $\mu$ . For an

incompressible Newtonian fluid, the viscous stresses are

$$\tau_{xx} = 2\mu \frac{\partial u}{\partial x} \quad (3.35)$$

$$\tau_{yx} = \mu \left( \frac{\partial v}{\partial x} + \frac{\partial u}{\partial y} \right) \quad (3.36)$$

$$\tau_{zx} = \mu \left( \frac{\partial w}{\partial x} + \frac{\partial u}{\partial z} \right) \quad (3.37)$$

Some of these terms can be cancelled out using the continuity equation. The remaining terms, combined with the body force term and put into the equation for the force in the x-direction, give

$$\sum F_x = \left\{ \rho g_x - \frac{\partial p}{\partial x} + \mu \left( \frac{\partial^2 u}{\partial x^2} + \frac{\partial^2 u}{\partial y^2} + \frac{\partial^2 u}{\partial z^2} \right) \right\} \Delta x \Delta y \Delta z \quad (3.38)$$

This gives, as the final expression of the x-momentum equation,

$$\rho \left( \frac{\partial u}{\partial t} + u \frac{\partial u}{\partial x} + v \frac{\partial u}{\partial y} + w \frac{\partial u}{\partial z} \right) = \rho g_x - \frac{\partial p}{\partial x} + \mu \left( \frac{\partial^2 u}{\partial x^2} + \frac{\partial^2 u}{\partial y^2} + \frac{\partial^2 u}{\partial z^2} \right) \quad (3.39)$$

The corresponding momentum equations in the y and z directions, respectively, are

$$\rho \left( \frac{\partial v}{\partial t} + u \frac{\partial v}{\partial x} + v \frac{\partial v}{\partial y} + w \frac{\partial v}{\partial z} \right) = \rho g_y - \frac{\partial p}{\partial y} + \mu \left( \frac{\partial^2 v}{\partial x^2} + \frac{\partial^2 v}{\partial y^2} + \frac{\partial^2 v}{\partial z^2} \right) \quad (3.40)$$

and

$$\rho \left( \frac{\partial w}{\partial t} + u \frac{\partial w}{\partial x} + v \frac{\partial w}{\partial y} + w \frac{\partial w}{\partial z} \right) = \rho g_z - \frac{\partial p}{\partial z} + \mu \left( \frac{\partial^2 w}{\partial x^2} + \frac{\partial^2 w}{\partial y^2} + \frac{\partial^2 w}{\partial z^2} \right) \quad (3.41)$$

## 3.2 NAVIER-STOKES AND CONTINUITY EQUATIONS FOR INCOMPRESSIBLE FLOW IN CYLINDRICAL COORDINATES

### 3.2.1 Continuity Equation

For cylindrical coordinates, a convenient control volume (whose sides are parallel to the coordinates) may be selected as shown in Figure 3.2.

The aim is to account for all the fluid that is accumulating, and flowing through this control volume, namely:

$$\text{Rate of Accumulation} + \text{Rate of Flow In} = \text{Rate of Flow Out}$$

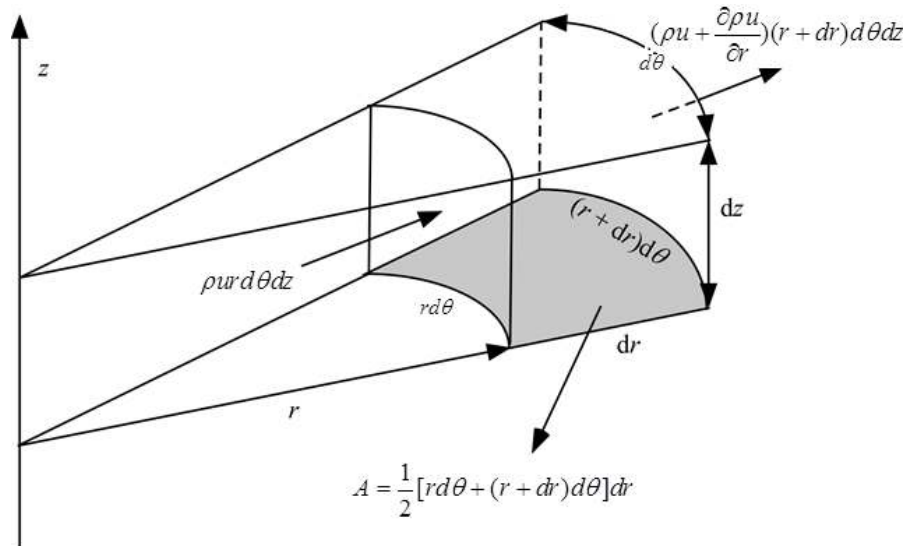


Figure 3.2: Elemental Fluid Volume for Derivation of the Fluid Equations in Cylindrical Coordinates.

The velocity field will be described as

$$u = v_r e_r + v_\theta e_\theta + v_z e_z \quad (3.42)$$

The volume of the differential control volume is

$$dV = r dr d\theta dz \quad (3.43)$$

The mass of fluid in the control volume is

$$dM = \rho dV \quad (3.44)$$

The rate of change of mass or accumulation in the control volume is then

$$\text{Mass accumulating} = \frac{\partial \rho}{\partial t} r dr d\theta dz \quad (3.45)$$

For the net flow through the control volume (dealing with one face at a time), considering the r faces, the net inflow is

$$\dot{m}_{r,in} = \rho u r d\theta dz \quad (3.46)$$

while the outflow in the r direction is

$$\dot{m}_{r,out} = \left(\rho u + \frac{\partial \rho u}{\partial r} dr\right)(r + dr) d\theta dz \quad (3.47)$$

So that the net flow in the r direction is

$$\dot{m}_{r,out} - \dot{m}_{r,in} = \rho u dr d\theta dz + \frac{\partial \rho u}{\partial r} r dr d\theta dz + \frac{\partial \rho u}{\partial r} dr^2 d\theta dz \quad (3.48)$$

The last term in this equation can be dropped (higher order) so that the net flow on the r faces is

$$\dot{m}_{r,out} - \dot{m}_{r,in} = \frac{1}{r} \rho u dV + \frac{\partial \rho u}{\partial r} dV \quad (3.49)$$

The net flow in the theta direction is slightly easier to compute since the areas of the inflow and outflow faces are the same. At the outset, the net flow in the theta direction is

$$\dot{m}_{\theta,net} = \frac{1}{r} \frac{\partial \rho v_{\theta}}{\partial \theta} dV \quad (3.50)$$

Considering the z direction, the face area is that of a sector of angle  $d\theta$  :

$$\begin{aligned}
A_z &= \frac{1}{2}(r + dr)^2 d\theta - \frac{1}{2}r^2 d\theta \\
&= r dr d\theta + \frac{1}{2} dr^2 d\theta \quad (\text{i.e neglecting the higher order term}) \\
&= r dr d\theta
\end{aligned} \tag{3.51}$$

The inflow at the lower z face is

$$\dot{m}_{z,in} = \rho w A_z = \rho w r dr d\theta \tag{3.52}$$

while the outflow at the upper z face is

$$\begin{aligned}
\dot{m}_{z,out} &= \left( \rho w + \frac{\partial \rho w}{\partial z} dz \right) A_z \\
&= \rho w r dr d\theta + \frac{\partial \rho w}{\partial z} r dr d\theta dz
\end{aligned} \tag{3.53}$$

Finally, the net flow in the z direction is

$$\dot{m}_{z,out} - \dot{m}_{z,in} = \frac{\partial \rho w}{\partial z} r dr d\theta dz \tag{3.54}$$

Now, putting things together to obtain the continuity equation

$$\frac{\partial \rho}{\partial t} dV + \frac{1}{r} \rho u dV + \frac{\partial \rho u}{\partial r} dV + \frac{1}{r} \frac{\partial \rho v}{\partial \theta} dV + \frac{\partial \rho w}{\partial z} dV = 0 \tag{3.55}$$

Dividing by dV and rearranging the r components of the velocity

$$\frac{\partial \rho}{\partial t} + \frac{1}{r} \frac{\partial (r \rho v_r)}{\partial r} + \frac{1}{r} \frac{\partial (\rho v_\theta)}{\partial \theta} + \frac{\partial \rho v_z}{\partial z} = 0 \tag{3.56}$$



For an incompressible fluid,

$$\frac{1}{r} \frac{\partial(rv_r)}{\partial r} + \frac{1}{r} \frac{\partial(rv_\theta)}{\partial \theta} + \frac{\partial v_z}{\partial z} = 0 \quad (3.57)$$

### 3.2.2 Momentum (Navier-Stokes) Equations

A change of variables on the Cartesian equations will yield the following momentum equations for  $r$ ,  $\varphi$ , and  $z$ :

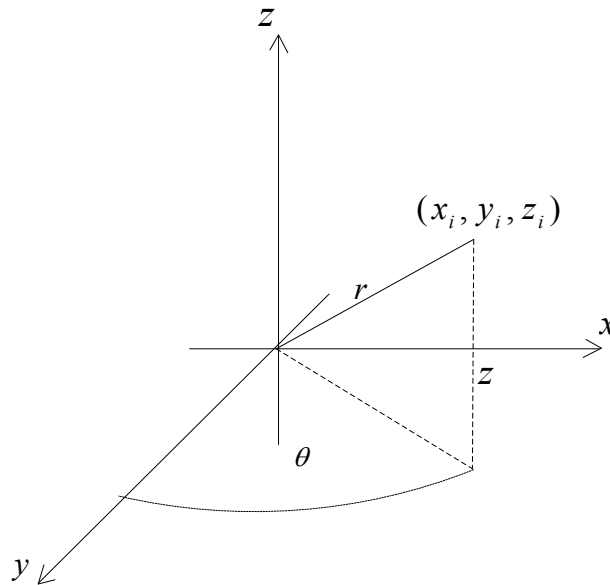


Figure 3.3: Change of Variables from Cartesian to Cylindrical Coordinates.

**r-component:**

$$\begin{aligned} \rho \left( \frac{\partial v_r}{\partial t} + v_r \frac{\partial v_r}{\partial r} + \frac{v_\theta}{r} \frac{\partial v_r}{\partial \theta} + v_z \frac{\partial v_r}{\partial z} - \frac{v_\theta^2}{r} \right) &= -\frac{\partial p}{\partial r} + F_r \\ + \mu \left( \frac{\partial^2 v_r}{\partial r^2} + \frac{1}{r} \frac{\partial v_r}{\partial r} + \frac{1}{r^2} \frac{\partial^2 v_r}{\partial \theta^2} + \frac{\partial^2 v_r}{\partial z^2} - \frac{v_r}{r^2} - \frac{2}{r^2} \frac{\partial v_\theta}{\partial \theta} \right) & \end{aligned} \quad (3.58)$$

**$\theta$ -component:**

$$\rho \left( \frac{\partial v_\theta}{\partial t} + v_r \frac{\partial v_\theta}{\partial r} + \frac{v_\theta}{r} \frac{\partial v_\theta}{\partial \theta} + v_z \frac{\partial v_\theta}{\partial z} + \frac{v_r v_\theta}{r} \right) = -\frac{1}{r} \frac{\partial p}{\partial \theta} + F_\theta$$

$$+ \mu \left( \frac{\partial^2 v_\theta}{\partial r^2} + \frac{1}{r} \frac{\partial v_\theta}{\partial r} + \frac{1}{r^2} \frac{\partial^2 v_\theta}{\partial \theta^2} + \frac{\partial^2 v_\theta}{\partial z^2} - \frac{v_\theta}{r^2} + \frac{2}{r^2} \frac{\partial v_r}{\partial \theta} \right)$$
(3.59)

**Z-component:**

$$\rho \left( \frac{\partial v_z}{\partial t} + v_r \frac{\partial v_z}{\partial r} + \frac{v_\theta}{r} \frac{\partial v_z}{\partial \theta} + v_z \frac{\partial v_z}{\partial z} \right) = -\frac{\partial p}{\partial z} + F_z$$

$$+ \mu \left( \frac{\partial^2 v_z}{\partial r^2} + \frac{1}{r} \frac{\partial v_z}{\partial r} + \frac{1}{r^2} \frac{\partial^2 v_z}{\partial \theta^2} + \frac{\partial^2 v_z}{\partial z^2} \right)$$
(3.60)

### 3.3 PRINCIPLES OF COMPUTATIONAL FLUID DYNAMICS (CFD)

Applying the laws of mechanics to a fluid results in the set of non-linear partial differential equations as derived above and summarized below.

Conservation of mass/continuity equation,

$$\frac{\partial \rho}{\partial t} + \nabla \cdot (\rho \vec{V}) = 0$$
(3.61)

and Conservation of momentum/Navier-Stokes equation,

$$\rho \frac{\partial \vec{V}}{\partial t} + \rho (\vec{V} \cdot \nabla) \vec{V} = -\nabla p + \rho \vec{g} + \nabla \cdot \tau_{ij}$$
(3.62)

Obtaining the exact (analytical) solutions to these equations is impossible [Bhaskaran and Collins, 2002]. With the advent of computers, however, it becomes possible to obtain approximate solutions to these equations.

The main strategy of CFD is to replace the continuous problem domain with a discrete domain using a grid [Bhaskaran and Collins, 2002]. Each flow variable (velocity,

pressure, e.t.c.) is defined at every point in the case of the continuous domain. A variable named velocity, for instance, would be given in the continuous 1D domain as

$$v = v(x), \quad 0 < x < 5 \quad (3.63)$$

In contrast, each flow variable is defined at the grid points in the case of discrete domain system. For the same velocity mentioned above, this will be defined on a finite number of  $N$  grid points as follows.

$$v_i = v(x_i), \quad i = 1, 2, \dots, N \quad (3.64)$$



Figure 3.4: Continuous Domain : PDEs + Boundary Conditions in Continuous Variables.

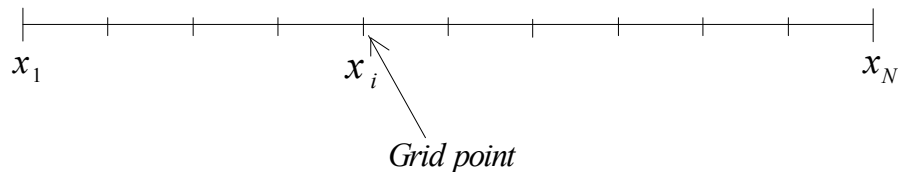


Figure 3.5: Discrete Domain ( $x_1, x_2, \dots, x_N$ ): Algebraic Equations in Discrete Variables.

The discretization makes it possible to directly solve for the relevant flow variables only at the grid points. Interpolation of the discrete values must be carried out in order to determine the values at other locations. The governing partial differential equations are usually expressed in terms of the variables ( $\vec{V}, p$  e.t.c.) in the continuous domain.

## **CHAPTER FOUR**

### **EXPERIMENTAL INVESTIGATIONS AND RESULTS**

#### **4.1 EXPERIMENTAL PROGRAM**

The experimental tests consisted of the following.

- 1) Standard tests on SCC mixes: Slump flow, L-box and V-funnel tests.
- 2) Rheological investigations on SCC mixes.
- 3) Flow profile during a full-scale slab casting.
- 4) Determination of lateral pressure exerted on a formwork during a full-scale casting of a vertical wall.

Table 4.1 shows the mix-proportions of the SCC tested. FA1 10% and FA2 10% represent mixes made of 10% fly ash with and without retarder (PR150) respectively. Similarly, SF1 10% and SF2 10% represent mixes made of 10% silica fume with and without retarder respectively, whereas SF3 10% represent mix with retarder but measurements were not taken until after the time (about 2 hours) when the retarder has lost its effectiveness.

In addition, the tests conducted at KFUPM by Malik (2011) was used for the verification of CFD modeling of various standard tests.

##### **4.1.1 Preparation of SCC Mixes**

A horizontal pan mixer was used in for all the mixes tested in this research while

Table 4.1: Mix Proportions used for Casting of Slab and Wall Elements.

Mix #	Cement (kg/m <sup>3</sup> )	SF- 10% (kg/m <sup>3</sup> )	Water (kg/m <sup>3</sup> )	Coarse Aggregates (kg/m <sup>3</sup> )			Fine Aggregate (kg/m <sup>3</sup> )	Admixture	
								VISCO (L/m <sup>3</sup> )	PR 150 (L/m <sup>3</sup> )
				20 mm	10 mm	5 mm			
FA1 10%	450	50	150	150	715	300	600	4.0	2.0
FA2 10%	450	50	150	150	715	300	600	4.0	0.0
SF1 10%	450	50	150	150	715	300	600	4.0	2.0
SF2 10%	450	50	150	150	715	300	600	4.0	0.0
SF3 10%	450	50	150	150	715	300	600	4.0	2.0

identifying the ones giving satisfactory flow and rheological properties. Coarse aggregate was placed followed by cement, mineral filler and sand respectively. These ingredients were mixed for 60 sec. Water and superplasticizer were then added slowly during the mixing process. Extra care and patience were exercised to make sure that the superplasticizer was added in small increments to prevent bleeding.

#### 4.1.2 Slump Flow and T500 Test

This test is a measurement for the filling ability of SCC. It measures two parameters: flow spread and flow time T500. A cleaned base plate was placed in a stable and level position. The inner surface of the cone and the test surface of the base plate were pre-wet using a moist towel. The cone was then placed in the centre of the base plate. Without any external compacting action, the cone was filled with the SCC sample from a bucket.

Any surplus concrete above the top of the cone was struck off. After a short rest (no more than 30 seconds) the cone was lifted perpendicular to the base plate in a single movement in such a manner that the concrete was allowed to flow out freely without obstruction from the cone. A stopwatch was started immediately the cone loses contact with the base plate and was stopped when the front of the concrete first touched the circle of diameter 500mm. The stop watch reading was recorded as the T500 (or T50) value. The test was completed when the concrete flow ceased (Figure 4.1). The largest diameter of the flow spread and the one perpendicular to it were measured and the average taken and recorded as the slump flow spread.



Figure 4.1: Slump Flow and T500 Test.

#### **4.1.3 V-funnel Test**

The V-funnel test is a measurement for the filling ability of SCC. The cleaned V-funnel was placed vertically on a stable and flat ground, with the top opening horizontally

positioned. The inner side of the funnel was kept under ‘just wet’ condition. The gate was closed and a bucket was placed under it in order to retain the concrete to be passed. The funnel was filled completely with a representative sample of SCC without applying any compaction or rodding. Any surplus concrete was removed from the top of the funnel using a straight edge. The gate was opened after a waiting period of few seconds. The stopwatch was started at the same moment the gate opens. The time was stopped at the moment a clear space was visible through the opening of the funnel. The stop watch reading was recorded as the V-funnel flow time.



Figure 4.2: V-funnel Test.

#### 4.1.4 L-box Test

This test is a measurement for the passing ability of SCC. The L-box was supported on a level horizontal base and the gate between the vertical and horizontal sections was closed. The SCC was poured from a container into the filling hopper of L-box and allowed to stand for few seconds. The gate was raised so that the SCC was allowed to flow into the horizontal section of the box. When movement ceased, the vertical height of SCC at the end of the horizontal section of the box was measured at three different positions across the width of the box. These three measurements were used to calculate the mean depth of the concrete as  $h_2$  (mm). The same procedure was used to calculate the depth of SCC immediately behind the gate as  $h_1$  (mm).



Figure 4.3: L-box Test.



#### 4.1.5 Determination of Rheological Parameters of Yield Stress and Viscosity

Figure 4.4 shows the ICAR rheometer used to measure the rheology of SCC [ICAR, 2008]. The fresh concrete is held in a container. Other components of the rheometer include a driver head housing an electric motor and torque meter, a chuck on the driver holding a four-blade vane (having diameter and height of 127 mm), and a laptop computer to operate the driver, record the torque during the test, and calculate the flow parameters. The driver/vane assembly was attached to the top of the container by means of a frame. A series of vertical rods are arranged around the perimeter of the container to prevent slipping of the concrete during the test. The nominal maximum size of the aggregate dictates the selection for the size of the container and length of the vane shaft.



Figure 4.4: ICAR Rheometer.

##### 4.1.5.1 Stress Growth Test

This test provides the information required (the maximum torque) to calculate the static yield stress of the SCC material. The test consists of rotating the vane at a constant speed of 3.76 rad/sec. The build of torque is measured as a function of time. Figure 4.5 shows the results of a typical stress growth test.

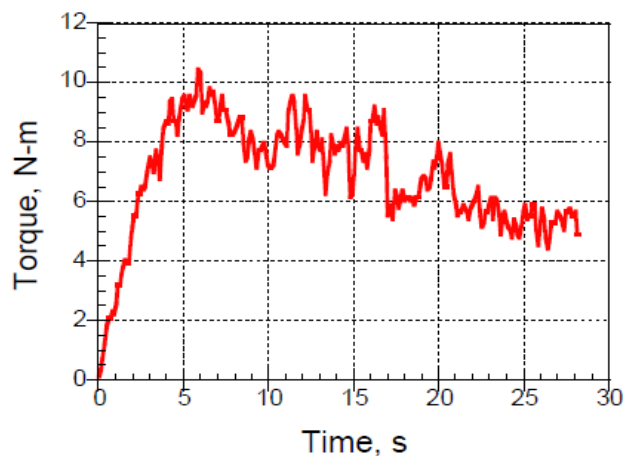


Figure 4.5: Stress Growth Test.

Calculation of the static yield stress is achieved using the peak torque and this value is displayed at the bottom of the computer display (Figure 4.6).

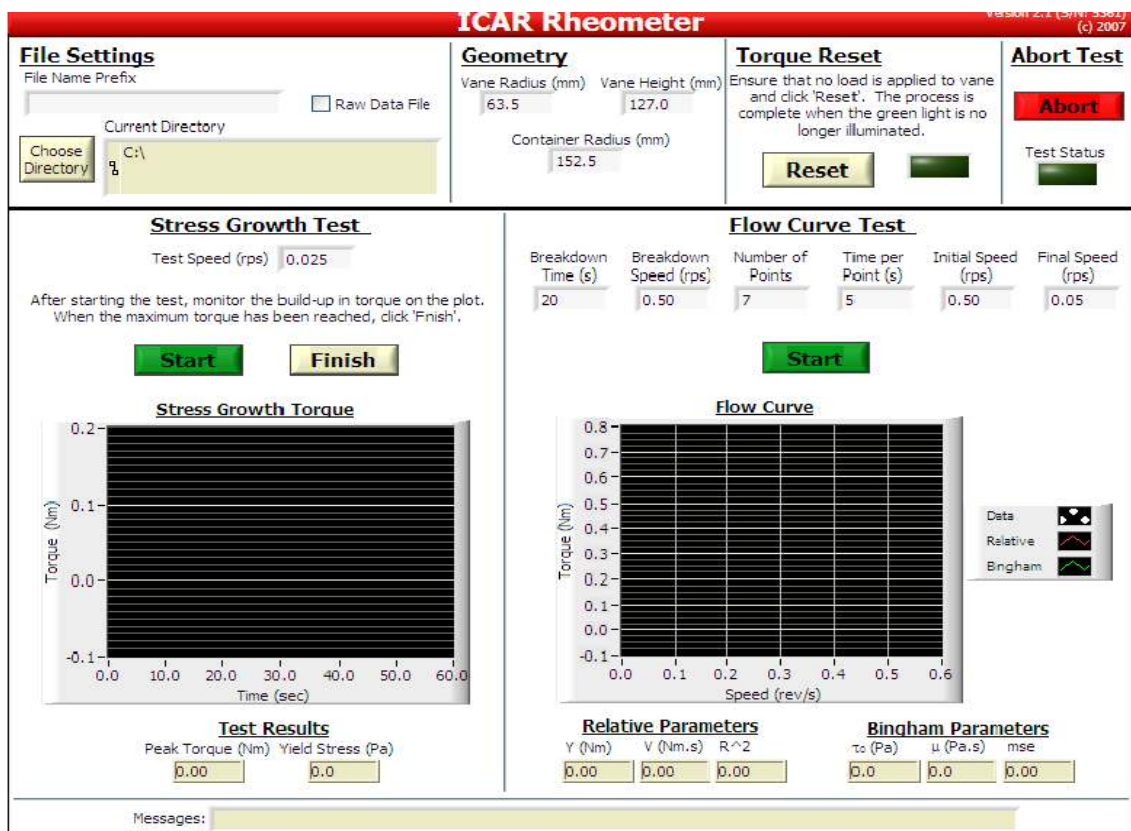


Figure 4.6: ICAR Rheometer Software Window [ICAR, 2008].

Depending on whether or not all the material in the container is flowing, Reiner-Riwlin equations were used to calculate the stress at the other points in the stress growth test.

For the case for where all material flows, the Reiner-Riwlin equation is

$$\dot{\gamma} = \frac{T}{4\pi h \mu} \left( \frac{1}{R_1^2} - \frac{1}{R_2^2} \right) - \frac{\tau_0}{\mu} \ln \left( \frac{R_2}{R_1} \right) \quad (4.1)$$

For the case where not all material flows:

$$\dot{\gamma} = \frac{T}{4\pi h \mu} \left( \frac{1}{R_1^2} - \frac{2\pi h \tau_0}{T} \right) - \frac{\tau_0}{2\mu} \ln \left( \frac{T}{2\pi h \tau_0 R_1^2} \right) \quad (4.2)$$

Where  $\dot{\gamma}$  is the shear rate (rad/s), T is the torque (Nm), h is the vane height (m),  $\mu$  is the plastic viscosity (Pas),  $\tau_0$  is the yield stress threshold (Pa),  $R_1$  is the vane radius, and  $R_2$  is the outer container radius.

To identify the applicable case under consideration, the effective radius that separates the flowing region from the non-flowing region was used thus.

$$R_{2,eff} = \sqrt{\frac{T}{2\pi h \tau_0}} \quad (4.3)$$

The material does not flow in the region where the shear stress of the material is below the yield stress and, hence, the effective radius is less than the container radius. On the other hand, the material flows completely when the shear stress is higher than the yield stress thereby resulting in the effective radius to be more than the container radius. At the early part of the stress growth test, the material only flows partially in the container. But as the test proceeds and the effective radius goes beyond the threshold value, the material flows completely in the container.

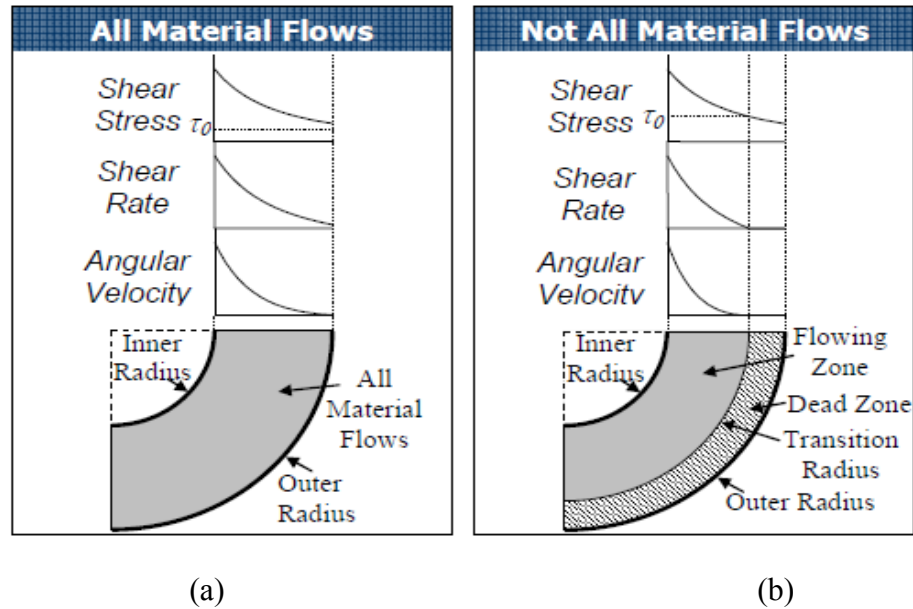


Figure 4.7: Cases where (a) All Material Flows and (b) Not all Material Flows [ICAR, 2008].

#### 4.1.5.2 Flow Curve Test

In order to model the SCC in a FLUENT software using Bingham model, two rheological test parameters are needed, namely, the dynamic yield stress and the plastic viscosity. By conducting the flow curve test, the ICAR Rheometer can handle this. For that purpose, this test was conducted in this study. To provide a consistent shearing history and breakdown any thixotropic structure that may exist, the test begins with a “breakdown” period in which the vane is rotated at maximum speed of 3.76 rad/sec. before measuring the Bingham parameters. This speed is then reduced in seven steps. During each step the speed is held constant and the average speed and torque is recorded. The ICAR Rheometer software performs all the necessary functions: operates the drivers, records the torque, computes test results, and stores data. Figure 4.8 shows a typical extract from the software window (Figure 4.6) for the plot of torque versus vane speed.

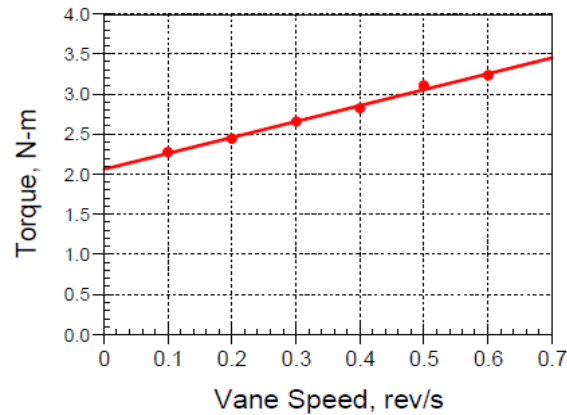


Figure 4.8: Flow Curve Test.

The intercept and slope are reported as relative parameters through computing a best-fit line to the data by the software. The software also computes the Bingham parameters of dynamic yield stress and plastic viscosity.

#### **4.1.6 Full-Scale Casting of a Wall and Determination of Lateral Pressure on the Formwork – Instrumentation and Data Acquisition**

A 200cmX150cmX20cm box, made of a combination of plywood and Plexiglas, was fabricated as a mold for casting the vertical wall element. One side is intentionally made with Plexiglas in order to visually monitor the flow progress during the casting operation. Figure 4.9 shows the picture of the formwork so formed.

The vertical wall formwork was equipped with pressure transducers as follows. Two pieces of PWB-20MPB pressure transducers manufactured by Tokyo Sokki Kenkyujo Company were fixed, one at the base and the other at a distance of 1m from the base respectively. Figure 4.10 shows the picture of the transducer used and the fixing details to the vertical formwork for the wall.



Figure 4.9: A 2mX1.5mX0.2m Fabricated Formwork for the Measurement of Lateral Pressure Exerted by SCC due to Full-Scale Casting of a Wall.

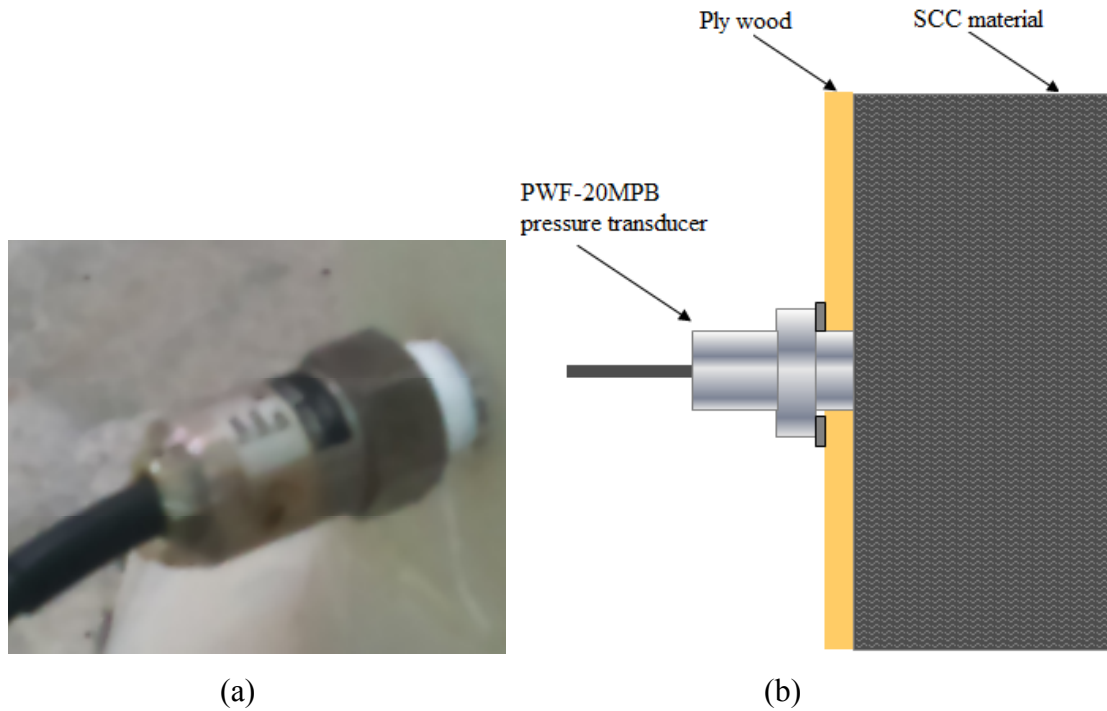


Figure 4.10: (a) PWF-20MPB Pressure Transducer (b) Fixing Details.

Prior to fixing these transducers, a calibration was achieved in the laboratory in which the calibration coefficient was determined for inputting into the data logger. Figure 4.11 (a) shows the calibration process where a known height of water (with a density known) was used to fill a plastic mold and the resulting pressure so exerted read in the data logger (Figure 4.11 (b)). Necessary adjustments on the value of the coefficient were made until a pressure reading approximately equal to the expected hydrostatic value was achieved.

Out of the tested SCC design mixes shown in Table 4.1, SF2 10% was used for the casting of the vertical wall. After a thorough mixing in a truck mixer (Figure 4.12 (a)) for a reasonable period of time, a concrete pump (Figure 4.12 (b)) was used to supply the SCC into the formwork (Figure 4.12 (c)). The pressure transducers attached to the



formwork sense the pressure and the readings were automatically recorded and saved by the data logger.



(a)

(b)

Figure 4.11: Determination of the Calibration Coefficient:  
 (a) Column of Water Confined in a Plastic Mold (b) Portable Data Logger.

#### 4.1.7 Full-Scale Casting of a Slab

A 100cmX100cmX30cm box made of a combination of plywood and Plexiglas was fabricated as a mould for casting the slab element. One side is intentionally made with Plexiglas in order to visually monitor the flow progress during the casting operation. Figure 4.13 shows the picture of the formwork so formed.

The same mix-design (SF2 10%) for the SCC used in casting the vertical wall was used to cast the slab. After a thorough mixing for a reasonable period of time in the truck





(a)

(b)



(c)

Figure 4.12: Operations During the Wall Casting; (a) Mixing using a Truck Mixer (b) Pumping using a Concrete Pump (c) Vertical Wall Formwork.



Figure 4.13: Fabricated Formwork for the Study of Flow Profiles During the Casting of the Slab.

mixture, a concrete pump was used to supply the SCC into the formwork. The progressive flow was monitored until the SCC inside the formwork reached a level of 25 cm.

## **4.2 RESULTS FOR THE EXPERIMENTAL PROGRAM AND DISCUSSION**

Results of the workability tests for slump flow and T500, L-box ratio and V-funnel time conducted to identify the required mix-design for the wall and slab casting are summarized in Table 4.2. The rheological parameters for yield stress and plastic viscosity measured for the trial and finalized mixes are shown in Table 4.3.

### **4.2.1 Slump Flow, T500, L-box and V-funnel Tests**

Result for the slump flow and T500 tests (Table 4.2) shows that all the mixes tested have satisfactory slump flow (650-800mm) and T500 (2-5 sec.) values. The samples

Table 4.2: Fresh Properties of SCC.

Mix	Slump flow (mm)	T-50 (s)	V-funnel(s)	L-Box Ratio
FA1 10%	750	4.16	7.8	1
FA2 10%	730	4.0	10.2	0.9
SF1 10%	690	2.56	11.59	0.8
SF2 10%	700	2.75	7.85	0.96
SF3 10%	680	3.16	9.12	0.82

Table 4.3: Bingham Parameters.

Mix	$\tau_0$ (Pa)	$\mu$ (Pa-s)
FA1 10%	70.3	8.3
FA2 10%	60.1	52.5
SF1 10%	82.2	8.9
SF2 10%	95.1	28.4
SF3 10%	90.4	45.0

containing fly ash (with or without retarder) show more flowability as seen in the slump flow values than those made using silica fume. Also, the T500 values for these mixes are higher than those containing silica fume. However, minor segregation effect was observed in the case of those samples containing fly ash as an admixture.

The range of L-box ratios obtained (0.8-1.0) indicate a good passing ability for all the mixes. Also, as was physically observed at the end of the test, the aggregate blocking was avoided as the SCC flow through the reinforcement.

Flow times within the satisfactory range (6-12 sec.) were obtained in all the mixes tested using the V-funnel. This test method predicts the flowability of the fresh concrete tested

and, hence, reaffirms the result obtained for the slump flow test which also shows that all the mixes are highly flowable.

#### 4.2.2 Rheology and Thixotropy Parameters

The stress growth test was used to determine the thixotropy parameters. It was performed at a constant shear rate of  $3.76 \text{ s}^{-1}$  after allowing the sample to rest for three different times (1 minute, 5 minutes and 15 minutes). Figure 4.14 shows a typical plot of the parameter  $\lambda$  from the stress growth test.

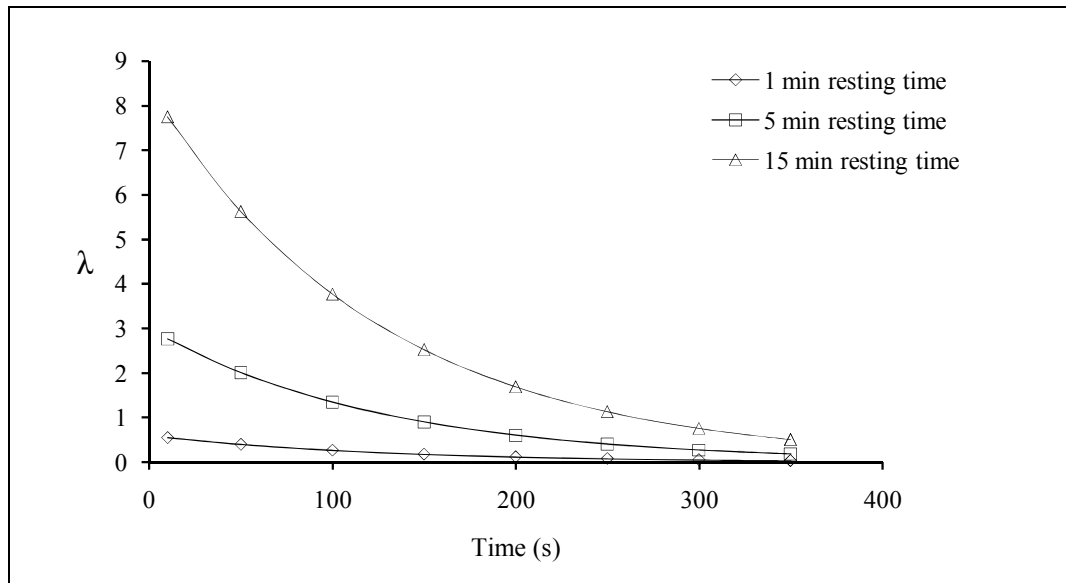


Figure 4.14:  $\lambda$  vs Time at Constant Shear Rate.

The plot shown in Figure 4.14 explains that the static yield stress (related to  $\lambda$  through  $\tau = (1 + \lambda)\tau_0 + \mu\dot{\gamma}$ ) and the time needed to reach steady state increases with increase in resting time. The flocculation resulted during the resting period makes the initial values of  $\lambda$  (i.e.  $\lambda_0$ ) to be high. However, once shearing is started, it decreases with time exponentially towards zero (Malik, 2011). Two parameters are obtainable from the plot

shown in Figure 4.14:  $\lambda_0$  for each resting time and a value of the parameter  $\alpha$  obtained by fitting an exponential function ( $\lambda = \lambda_0 e^{-\alpha t}$ ) in the plot. Reciprocal of the slope of  $\lambda_0$  versus resting time (Figure 4.15) is used to obtain the characteristic flocculation time  $T$  from the relation  $\lambda_0 = \frac{t}{T}$ , whereas the flocculation rate is obtained as  $A_{\text{thix}} = \frac{\tau_0}{T}$ .

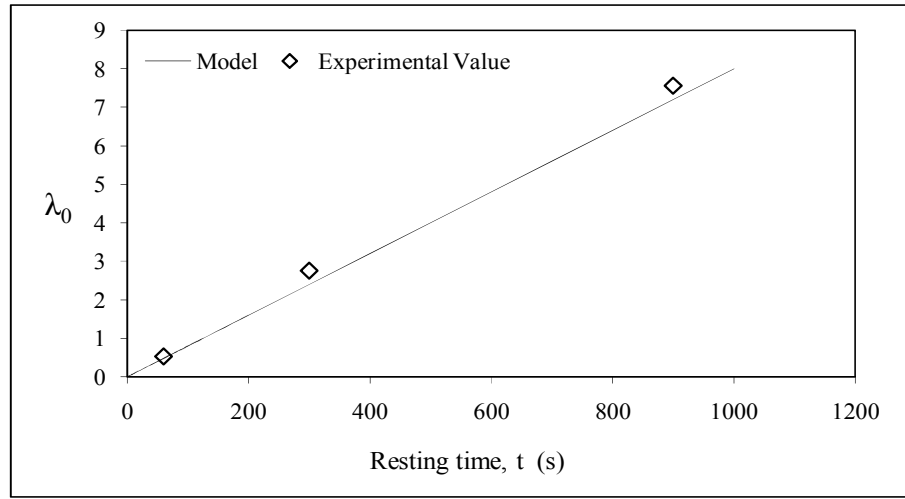


Figure 4.15:  $\lambda_0$  vs Resting Time.

Table 4.4 shows a summary of all the thixotropic parameters for all the mixes tested to identify the most suitable one for casting the slab and wall elements.

The results presented in Table 4.4 show that the first three mixes FA1 10%, FA2 10%, and SF1 10% resulted in very low values of  $A_{\text{thix}}$ . On the other hand, the mixes SF2 10% and SF3 10% gave relatively higher values of  $A_{\text{thix}}$ . However, in both the two cases, these values are on the boarder of the classification of thixotropy ranges proposed by Roussel (2006) (Table 2.1).  $A_{\text{thix}}$  values for the mixes FA1 10%, FA2 10%, and SF1 10% are just within the border for the non-thixotropic and the thixotropic range, whereas

that of the mixes SF2 10% and SF3 10% are just within the border of the thixotropic and the highly thixotropic range.

Table 4.4: Thixotropy Parameters for all Mixes.

Mix	T (s)	$\lambda_0$			$\alpha$	$A_{thix}$ (Pa/s)
		1m	5m	15m		
FA1 10%*	620	0.22	0.64	1.20	0.0037	0.11
FA2 10%	400	0.45	0.91	1.12	0.0025	0.15
SF1 10%*	500	0.52	1.01	1.39	0.007	0.16
SF2 10%	200	1.60	2.98	4.33	0.004	0.48
SF3 10%**	166.8	1.98	2.67	2.90	0.0047	0.54

\* With Retarder and tested immediately

\*\* With Retarder and tested after 2 hours

Two reasons were observed to result in significantly lower values of the flocculation parameter  $A_{thix}$ ; the use of fly ash as the mineral admixture and the use of a retarder (PR150) in the mix. Fly ash was used in both FA1 10% and FA2 10% mixes and all resulted in very low thixotropy. Also, even between the two fly ash mixes, the one containing the retarder PR150 (FA1 10%) is seen to result in lower thixotropy than the one containing no retarder (FA2 10%). In addition, although the use of silica fume was observed to result in relatively more thixotropic mixes but still the use of the retarder PR150 and silica fume is seen to result into a very low thixotropic mix when  $A_{thix}$  is measured immediately after mixing (SF1 10%). However, if one waits for about 2 hours prior to testing, the influence of retarder is negated and the  $A_{thix}$  value of SF 3 10% becomes quite close to the  $A_{thix}$  value of SF2 10%. Another noticeable effect of the use of retarder is that of very low value of plastic viscosity. This can be seen in Table 4.3 where

the viscosity values obtained were 8.3 Pa-s and 8.9 Pa-s for FA1 10% and SF1 10% respectively. In order to offset the effect of using the retarder, a mix (SF3 10%) was tested containing silica fume and PR150 but rheological measurements were not taken until after a waiting time of about 2 hours from the initial mixing period. This was done to ensure that the retarder have lost its effectiveness at that time. As can be seen from the result, the  $A_{thix}$  value computed for this mix (0.54) appear to be in close agreement with that of the mix (SF2 10%) in which no retarder was used (0.48). Also, as can be seen in Table 4.3 the value of the plastic viscosity (45.0Pas) obtained in SF23 10% is seen to increase significantly over that obtained (8.9Pas) when the retarder was still effective (SF1 10%). Significant lowering of  $A_{thix}$  in the presence of retarders would result in high formwork pressure for such SCC mixes when used in vertical wall construction.

#### 4.2.3 Flow Profiles during Slab Casting and Lateral Formwork Pressure

Table 4.5 shows the result for the change in level/height of the SCC specimen at the end of the slab casting operation. This result will be utilized for comparison with that of the CFD simulation discussed in chapter five.

Table 4.5: Experimental Result for the Full-Scale Slab Casting.

H (cm)	5	10	15	20	25
Time (s)	19.1	34.5	53.3	86.2	114.5

Similarly, the pressure readings at the end of the full-scale casting of the wall element are shown in Table 4.6 and these will be utilized for comparison with the CFD and the proposed finite element model simulations discussed in chapters five and six respectively.

Table 4. 6: Experimental Result for the Pressure exerted on Formwok during the Full-Scale Wall Casting.

Height (m)	0	0.06	0.16	0.32	0.50	0.53	0.75	0.72	0.79	0.85	1.0
Lateral Pressure (Kpa)	0	1.3	3.4	6.9	11	11.7	16.5	15.8	17.2	18.6	20.8



## **CHAPTER FIVE**

### **COMPUTATIONAL FLUID DYNAMICS SIMULATION OF SCC FLOW AND RESULTS**

#### **5.1 GENERAL**

Validation of the computational fluid dynamics simulation in this study includes the use of the available experimental data reported in [Malik, 2011], where a series of experiments were conducted using different SCC mixes to obtain the critical range of rheological parameters of yield stress and viscosity where segregation is minimized, yet the material will retain its fluidity. Nine mix designs were made by varying the amount of Silica Fume, Limestone powder and Fly ash. Water/powder ratio was kept constant at 0.3. Tables 5.1 and 5.2 show, respectively, the mix proportions and the thixotropy and Bingham parameters of the SCC tested by Malik (2011).

#### **5.2 NUMERICAL (CFD) SIMULATION OF SCC CONVENTIONAL TESTS**

In this chapter, computer-aided numerical simulation of the flow of SCC given in table 5.1 was carried out to verify its constitutive material behavior for each of the following SCC flow tests:

- Slump Flow and T500 Test
- L-Box Test
- V-funnel Test

Table 5.1: Mix Proportions [Malik, 2011].

	Cement (kg/m <sup>3</sup> )	Filler (kg/m <sup>3</sup> )	Water (kg/m <sup>3</sup> )	Coarse Aggregates (kg/m <sup>3</sup> )			Fine Aggregate (kg/m <sup>3</sup> )	Viscocrete (kg/m <sup>3</sup> )
				20 mm	10 mm	5 mm		
REF	485	0	144	456	341	270	690	4.47
SF 2.5%	473	12	144	456	341	270	690	3.55
SF 5%	461	24	144	456	341	270	690	5
SF 7.5%	449	36	144	456	341	270	690	5.26
LSP 5%	461	24	144	456	341	270	690	6.31
LSP 10%	437	48	144	456	341	270	690	5
LSP 15%	413	72	144	456	341	270	690	4.2
FA 5%	461	24	144	456	341	270	690	3.42
FA 7.5%	449	36	144	456	341	270	690	3.55
FA 10%	437	48	144	456	341	270	690	3.68

Table 5.2: Thixotropy and Bingham Parameters for all mixes [Malik, 2011].

Mix	$\tau_0$ (Pa)	$\mu$ (Pa-s)	T (s)	$\lambda_0$			$\alpha$	$A_{thix}$ (Pa/s)
				1m	5m	15m		
REF	56.3	48.4	125	2.1	3	6.8	0.0038	0.46
SF 2.5%	65.1	52.5	90.9	3.5	5.6	9.6	0.0025	0.715
SF 5%	65.5	54.9	111	0.5	2.7	7.5	0.0019	0.53
SF 7.5%	58.4	71.2	111	3	4.4	7.5	0.0037	0.52
LSP 5%	39.3	59.2	76.9	4	6.5	11.5	0.0027	0.51
LSP 10%	45.5	53.1	71.4	4.8	7.5	11.2	0.0037	0.63
LSP15%	36	63	52.6	5	7.8	16.5	0.0039	0.68
FA 5%	34	48.9	111	2	5	8	0.0039	0.3
FA 7.5%	47.4	62.9	67	3.5	7.4	13	0.0027	0.7
FA 10%	32.2	58.6	20	8	20	42	0.0027	1.6

## 5.2 NUMERICAL (CFD) SIMULATION OF SCC CONVENTIONAL TESTS

In this chapter, computer-aided numerical simulation of the flow of SCC given in table 5.1 was carried out to verify its constitutive material behavior for each of the following SCC flow tests:

- Slump Flow and T500 Test
- L-Box Test
- V-funnel Test

### 5.2.1 Discretization Scheme

The domain of interest for each of the above mentioned test was decided and the boundary conditions identified. The geometric modeling of the same was achieved using the GAMBIT program [Fluent inc., 2003].

The *Set Face Element Type* command was used to specify the mesh node configuration associated with either of two available face element shapes.

To set the face element type, it was necessary to specify the node pattern associated with each of the face element shapes. There are two face element shapes available in GAMBIT:

- Quadrilateral
- Triangle

Each face element shape is associated with three different node patterns, and each node pattern is characterized by the number of nodes in the pattern. Figures 5.1 and 5.2 show the node patterns associated with the quadrilateral and triangular face element types, respectively.

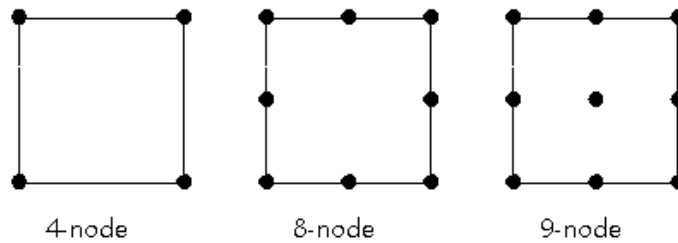


Figure 5.1: Quadrilateral Face Element Types.

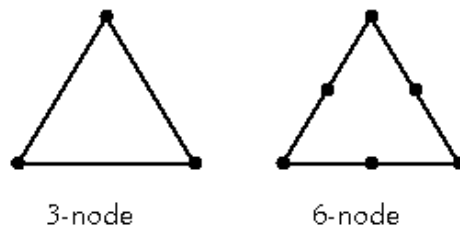


Figure 5.2: Triangular Face Element Types.

When a face element type is set, GAMBIT applies the type to all face elements of the specified shape. For example, if 8-node quadrilateral face elements are specified, GAMBIT locates mesh nodes according to the 8-node pattern for all quadrilateral face elements produced in the subsequent face meshing operation.

The specification of the face element type was achieved using the *Set Face Element Type* form (Figure 5.3) by simply clicking the *Set Face Element Type* command button on the *Mesh/Face* subpad in the GAMBIT environment.

The 'Set Face Element Type' dialog box is divided into two columns. The left column is titled 'Quadrilateral' and contains three radio button options: '4 node' (selected), '8 node', and '9 node'. The right column is titled 'Triangle' and contains two radio button options: '3 node' (selected) and '6 node'. At the bottom of the dialog, there are three buttons: 'Apply', 'Reset', and 'Close'.

Figure 5.3: The Set Face Element Type Form.

The *Set Face Element Type* form contains the specifications shown in Table 5.3.

Table 5.3: Specifications for the Set Face Element Type Form.

Quadrilateral	Allows the specification of the quadrilateral face element node pattern. The available node patterns include 4 node, 8 node, and 9 node.
Triangle	Allows the specification of the triangular face element node pattern. The available node patterns include 3 node and 6 node.

It would be wise to mention that although it is possible to set the higher-order element types (for example, 8-node and 9-node quadrilateral elements) while modeling the geometry of concern in GAMBIT, Finite-volume solvers, such as FLUENT, employ only linear elements (for example, 4-node quadrilateral elements). For this reason, only the linear element types were used in this study.

For ease of identifying the initial conditions (those regions initially occupied by SCC and air), two domains were created and named as appropriate for the SCC and air in the GAMBIT environment. This way, it was easy to specify, in the FLUENT environment, the respective initial locations of the two phases (SCC and air).

Figures 5.4, 5.5 and 5.6 show the discretization of these domains for the Slump, L-box, and V-funnel tests respectively as exported to the FLUENT environment. It is important to note that although at the start of the V-funnel test the phase representing air is not present, it is still necessary to define the number of phases as two (2) in the FLUENT program (doing so in the GAMBIT is not necessary). This is because as the test simulation starts, the portion initially ( $t = 0$ ) defined to be occupied by SCC alone should

start to have a combination of both air and SCC (separated by the interface) at  $t > 0$ . Otherwise, if only one phase is to be defined in the FLUENT program, no air will be displacing the SCC material.

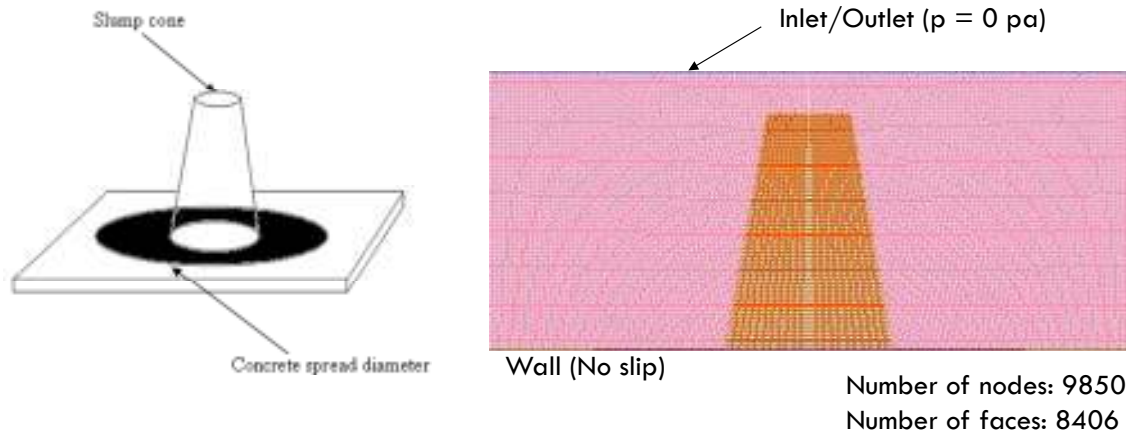


Figure 5.4: Grid for the Axisymmetric Simulation of Slump Test.

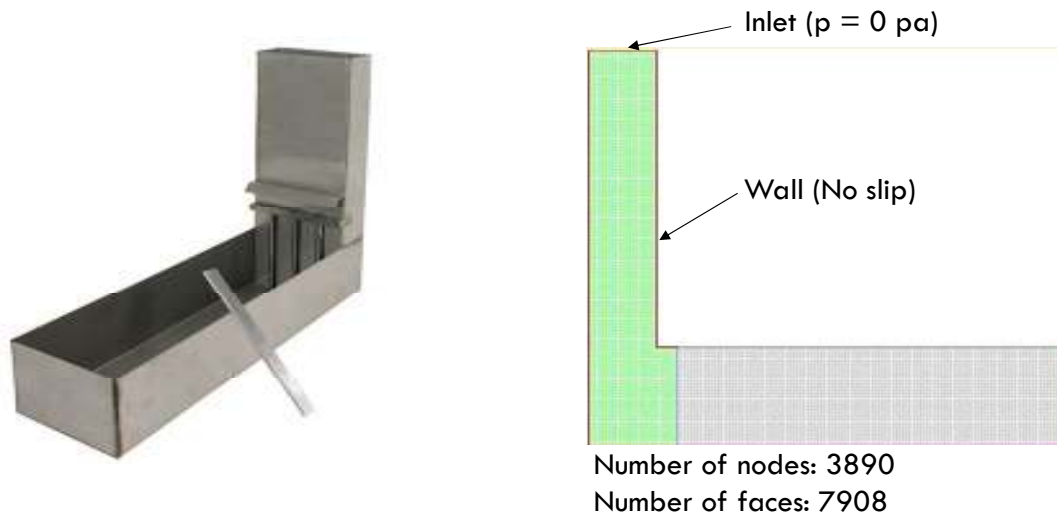


Figure 5.5: Grid for the 2D Simulation of L-box Test.

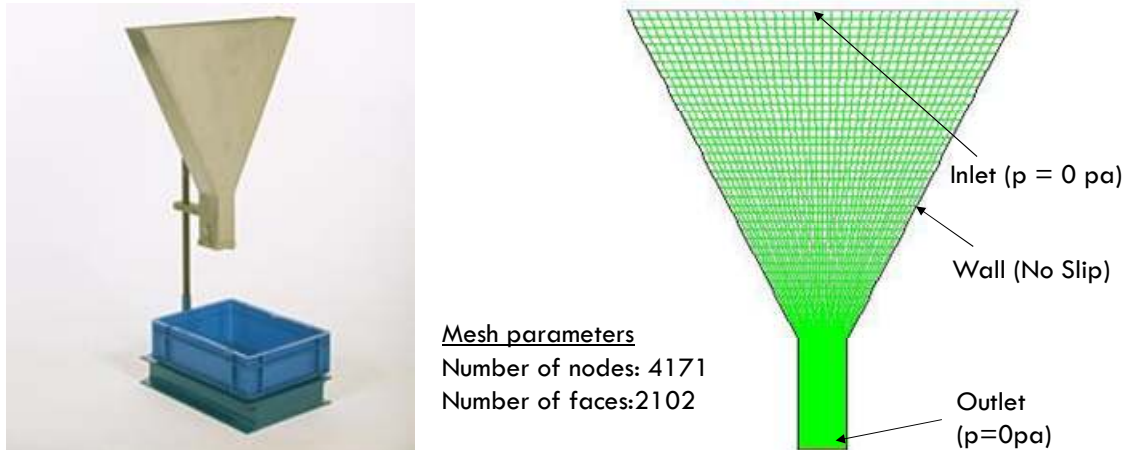


Figure 5.6: Grid for the 2D Simulation of V-funnel Test.

### 5.2.2 FLUENT Multiphase Modeling-The VOF Model [Fluent inc., 2003]

FLUENT code was used to carry out the numerical simulations in the flow tests of this research. The software has the capabilities to model fresh concrete flow behavior as carried out by Baluch et al. (2011), Nguyen et al. (2006), and De Schutter (2008). The simulation was achieved using the Volume of fluid (VOF) model. This model is a surface-tracking technique applied to a fixed Eulerian mesh. It is designed for two or more immiscible fluids where the position of the interface between the fluids is of interest. In the case of this study, the two fluids are SCC and air. The surface is reconstructed based on the volume fraction of concrete already filling a calculation cell.

In the VOF model, a single set of momentum equations is shared by the fluids, and the volume fraction of each of the fluids in each computational cell is tracked throughout the domain. A pressure-based solver was used (as the density-based solvers are not available when using the VOF model). In this scheme all control volumes must be filled with either a single fluid phase or a combination of phases. The model does not allow for void

regions where no fluid of any type is present. The VOF formulation relies on the fact that two or more fluids (or phases) are not interpenetrating. For each additional phase added to the model, a variable is introduced: the volume fraction of the phase in the computational cell. In each control volume, the volume fractions of all phases sum to unity. The fields for all variables and properties are shared by the phases and represent volume-averaged values, as long as the volume fraction of each of the phases is known at each location. Thus the variables and properties in any given cell are either purely representative of one of the phases, or representative of a mixture of the phases, depending upon the volume fraction values. In other words, if the  $q^{\text{th}}$  fluid's volume fraction in the cell is denoted as  $\alpha_q$ , then the following three conditions are possible:

$\alpha_q = 0$ : The cell is empty (of the  $q^{\text{th}}$  fluid).

$\alpha_q = 1$ : The cell is full (of the  $q^{\text{th}}$  fluid).

$0 < \alpha_q < 1$ : The cell contains the interface between the  $q^{\text{th}}$  fluid and one or more other fluids.

Based on the local value of  $\alpha_q$ , the appropriate properties and variables are assigned to each control volume within the domain.

The properties appearing in the transport equations are determined by the presence of the component phases in each control volume. In the two-phase system, if the volume fraction of the second of these is being tracked, and the phases are represented by the subscripts 1 and 2, then the density in each cell is given by

$$\rho = \alpha_2 \rho_2 + (1 - \alpha_2) \rho_1 \quad (5.1)$$



In general, for an n-phase system, the volume-fraction-averaged density takes on the following form:

$$\rho = \sum \alpha_q \rho_q \quad (5.2)$$

All other properties (e.g., viscosity) are computed in this manner.

The tracking of the interface(s) between the phases is accomplished by the solution of a continuity equation for the volume fraction of one (or more) of the phases. For the q<sup>th</sup> phase, this equation has the following form:

$$\frac{1}{\rho_q} \left[ \frac{\partial}{\partial t} (\alpha_q \rho_q) + \nabla \cdot (\alpha_q \rho_q \vec{v}_q) \right] = S_{\alpha_q} + \sum_{p=1}^n (\dot{m}_{pq} - \dot{m}_{qp}) \quad (5.3)$$

where  $\dot{m}_{qp}$  is the mass transfer from phase q to phase p and  $\dot{m}_{pq}$  is the mass transfer from phase p to phase q. By default, the source term on the right-hand side of the above equation,  $S_{\alpha_q}$ , is zero, although a constant or user-defined mass source can be specified for each phase.

The volume fraction equation is not solved for the primary phase; the primary-phase volume fraction is computed based on the following constraint:

$$\sum_{q=1}^n \alpha_q = 1 \quad (5.4)$$

A single momentum equation is solved throughout the domain, and the resulting velocity field is shared among the phases. The momentum equation, shown below, is dependent on the volume fractions of all phases through the properties  $\rho$  and  $\mu$ .

$$\frac{\partial}{\partial t}(\rho \vec{v}) + \nabla \cdot (\rho \vec{v} \vec{v}) = -\nabla_p + \nabla \cdot [\mu(\nabla \vec{v} + \nabla \vec{v}^T)] + \rho \vec{g} \quad (5.5)$$

### 5.2.3 Defining the Input File

#### 5.2.3.1 Solver Type and Number of Phases

Under this, the solver type needs to be defined which includes setting the type of space (2D, 3D or axisymmetric), type of problem (steady or unsteady), e.t.c. The number of phases required to solve the problem (SCC and air) also needs to be inputted under the model's set-up.

#### 5.2.3.2 Materials

Here, commands are given to let the FLUENT know the kind of materials whose solution should be obtained. By default, a database of materials including air will be found. Hence, the user only needs to select and add air to the model.

The next step is to define the SCC material whereby its rheological properties should be used as the input.

#### 5.2.3.3 Phases

Defining the lighter of the two materials as the primary phase is recommended by [Fluent inc., 2003] and, for that reason, was adopted here. Air being lighter than SCC was identified as the primary phase and the SCC as the secondary phase.

#### 5.2.3.4 Boundary Conditions

Depending on the test method being modeled, various types of boundaries can be specified as available in the FLUENT software. The screen shot shown in Figure 5.7

shows a typical boundary condition specification.

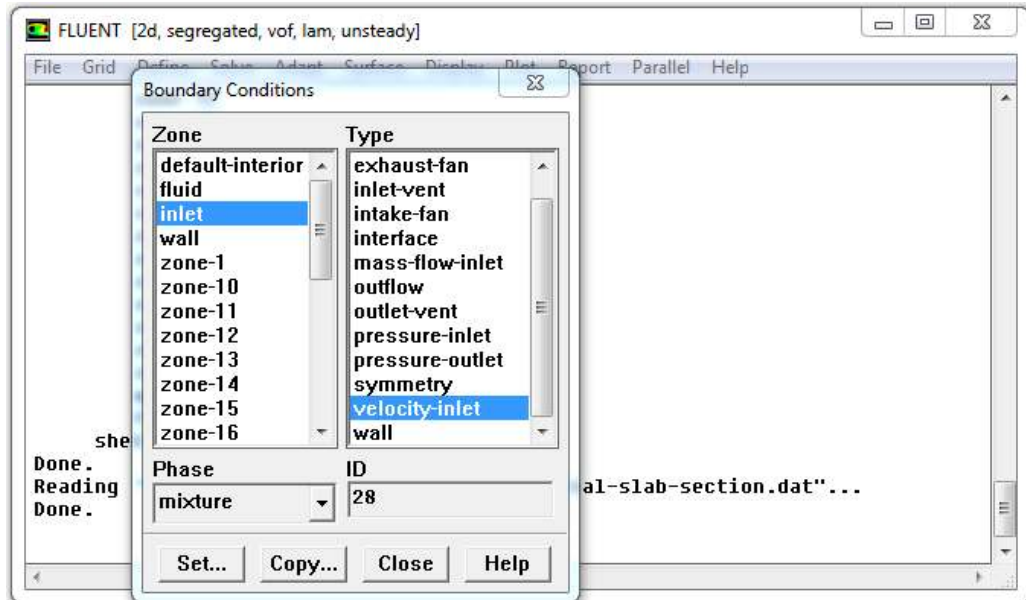


Figure 5.7: Defining the Boundary Conditions.

#### 5.2.3.5 Operating Conditions

The direction and magnitude of the acceleration due to gravity, atmospheric pressure, operating density, e.t.c were specified under this section.

#### 5.2.3.6 Initialization and Patching

By initialization, we mean notifying the software that the current definitions should be assumed as the initial stage (time=0) in the solution process. Options exist as to the initial values to be used. In addition, it is important to specify the exact initial location of the SCC material for any test to be modeled. The term used for this is patching. It allows the use of a value for volume fraction (0 to 1) present in the location we are patching. This was achieved by, first, specifying a continuum named “Concrete” in the GAMBIT. It made it easier to locate (especially when there are many zones to patch) and patch.

Figure 5.8 shows how this was achieved.

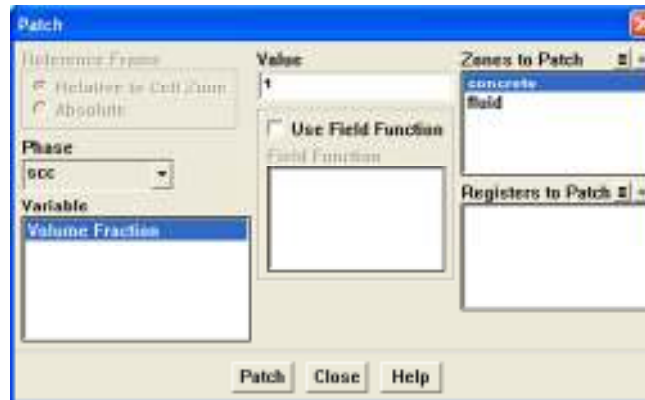


Figure 5.8: Patching the Initial Location of SCC.

#### **5.2.3.7 Monitoring the Residual**

This is an optional but very important step that will enable one to set and monitor the convergence criteria for the solution. In order to select the monitoring option, the Plot check should be checked.

#### **5.2.3.8 Time-Stepping and Size**

One of the necessary steps to obtain a solution is the specification of time step size and number of time steps. It is worth mentioning that the use of large time-step values leads to errors and abortion of the computation process. Very small values of time-steps were used in modeling each of the tests on SCC. At this stage, both the case and data files for each of the test modeled were saved and the iteration process was started from here.

#### **5.2.4 Modeling the Thixotropy of SCC: User-Defined Viscosity Function**

While the rheological behaviour of SCC can be described by means of a Bingham model, some extra phenomenons occurs, like shear thickening and sometimes significant thixotropy. This is because of presence of more ingredients, more complex mix design,

and low yield stress and viscosity. For that reason, the Bingham behavior in combination with shear thickening and thixotropy was modeled in the software package FLUENT by means of a user-defined thixotropy model proposed by Roussel (2006);

$$\tau = (1 + \lambda_0 e^{-\alpha \dot{\gamma} t}) \tau_0 + \mu_p \dot{\gamma} \quad (5.6)$$

Where  $\alpha$  is a destructurement parameter.  $\lambda$  is the flocculation state (also structuration state) of the concrete that evolves through the flow history.

Substituting  $\tau = \eta \dot{\gamma}$  into the above relation yields,

$$\eta = \frac{(1 + \lambda_0 e^{-\alpha \dot{\gamma} t}) \tau_0 + \mu_p \dot{\gamma}}{\dot{\gamma}} \quad (5.7)$$

The above equation gives the expression for the cell viscosity as a function of the thixotropic parameters, hence the thixotropy modeling.

In order to specify the cell viscosity equation above as a user-defined function in the FLUENT software, the use of C programming language was made. The variables were represented in the program as follows.

$$\eta = mu, \quad t = tim, \quad \tau_0 = tau0, \quad \mu_p = mup, \quad \lambda_0 = lam0, \quad \dot{\gamma} = shear\_rate$$

The following lines show the written program used as the user-defined viscosity function;

```
#include "udf.h"

DEFINE_PROPERTY(cell_viscosity, cell, thread)
{
    real mu, shear_rate, a1;
    real tim, lam0, alp, tau0, mup;
```

```

lam0=5.31;
tau0=39.3;
mup=59.2;
alp=0.0053;

tim=CURRENT_TIME;

shear_rate=C_U_G(cell,thread)[0];
a1=exp(-1*alp*shear_rate*tim);
mu=((1+lam0*a1)*tau0+mup*shear_rate)/shear_rate;
return mu;
}

```

The use of *CURRENT\_TIME* for *t* is an in-built function in the FLUENT and is recognized as the time at which the iteration being solved is computed.

$\dot{\gamma} = C\_U\_G(cell,thread)[0]$  is the expression for the derivative  $\frac{du}{dy}$  used for the shear rate. The values  $lam0=5.31$ ;  $tau0=39.3$ ;  $mup=59.2$ ;  $alp=0.0053$  used are just typical inputs for the SCC mix being modeled. Each time another mix needs to be modeled, appropriate values have to be used depending on the parameters obtained through rheology test.

The summary of the steps needed to carry out the CDF numerical simulation is shown in Figure 5.9 and a typical required data entered in the FLUENT input file is given in Table 5.4.

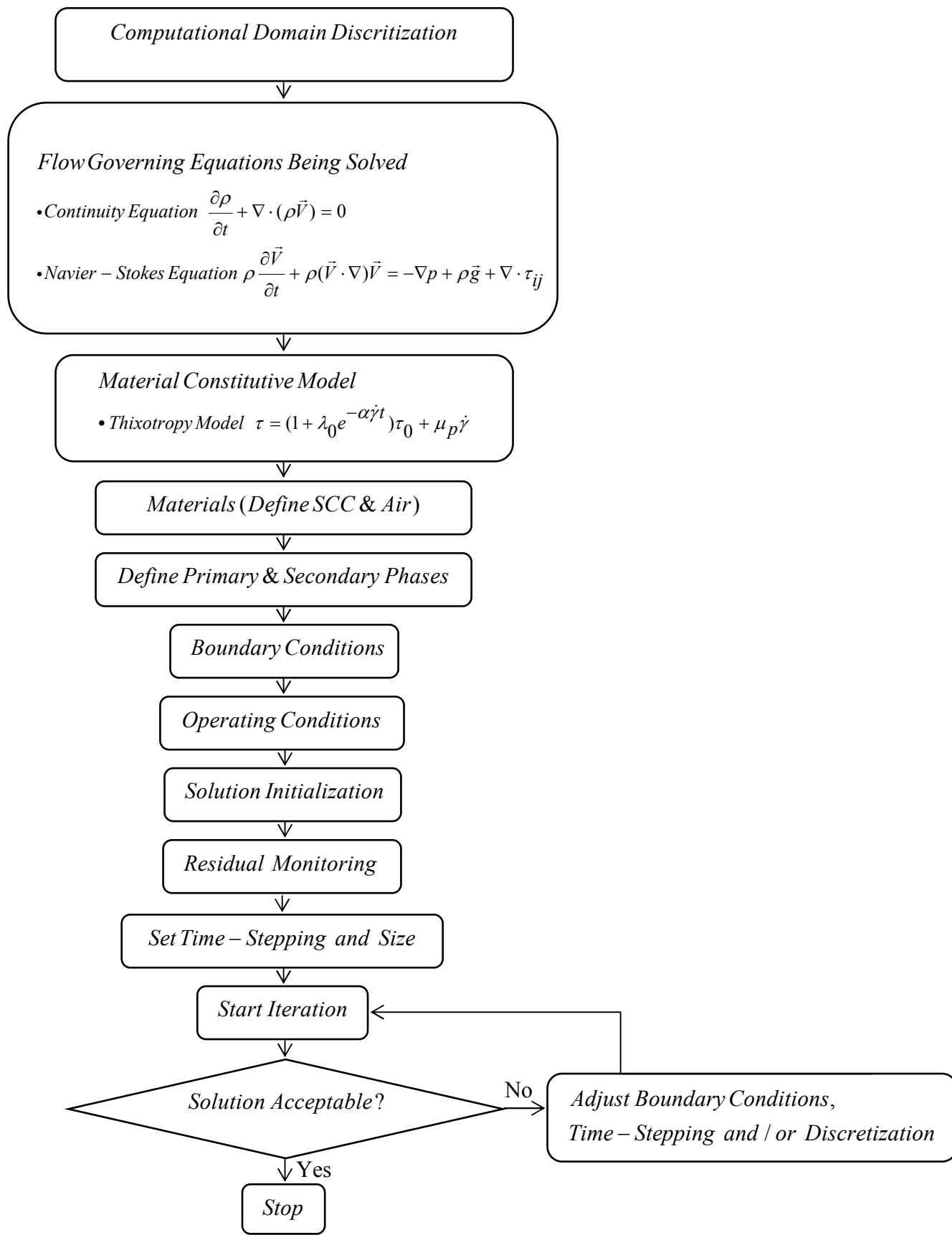


Figure 5.9: Summary of the Steps Needed to Obtain a CFD Solution.

Table 5.4: FLUENT Model Parameters.

FLUENT Dialogue Box	FLUENT Expression/Parameter		Value/Setting		
Solver Settings	Solver Type		Segregated		
	Space		2D, Axisymmetric or 3D		
	Time		Unsteady		
Multiphase Model	Model		Volume of Fluid		
	Number of Phases		2		
	Body Force Formulation		Implicit Body Force		
Materials	Air	Material Type		Fluid	
		Fluent Fluid Materials		Air	
		Density ( $Kg / m^3$ )		1.225	
		Viscosity ( $Kg / m - s$ )		1.7894E-05	
	SCC	Material Type		Fluid	
		Fluent Fluid Materials		SCC	
		Density ( $Kg / m^3$ )		2240	
		Viscosity* ( $Kg / m - s$ )	Herschel-Bulkley (Non-thixotropic)	Consistency Index, k	Value of $\mu$
				Power-Law Index, n	1
				Yield Stress Threshold	Value of $\tau_0$
				Yielding Viscosity	1E+07
		User-Defined Function (Thixotropy modeling)			$\lambda_0$
					$\tau_0$
	$\mu$				
	$\alpha$				
Phases	Air		Primary Phase		
	SCC		Secondary Phase		
Boundary Conditions	Inlet		Velocity Inlet		
	Outlet		Pressure Outlet		
Operating Conditions	Operating Pressure (Pa)		101325		
	Gravitational Acceleration		-9.81		
	Specified Operating Density		Check		
	Operating Density ( $Kg / m^3$ )		1.225		
Solution Initialization	Compute From		All Zones		
Residual Monitors	Plot		Check		
Iterate	Time Stepping and Size		Set to Ensure an Error-Free Convergence		



### 5.3 NUMERICAL (CFD) SIMULATION OF THE SLAB CASTING

A numerical modeling of the casting process was achieved using the FLUENT software. Figure 5.10 shows the meshing (as created in the GAMBIT) and boundary condition used for the slab geometry. Defining the problem in a FLUENT environment follows the same way as earlier explained for the conventional tests on SCC (section 5.2).

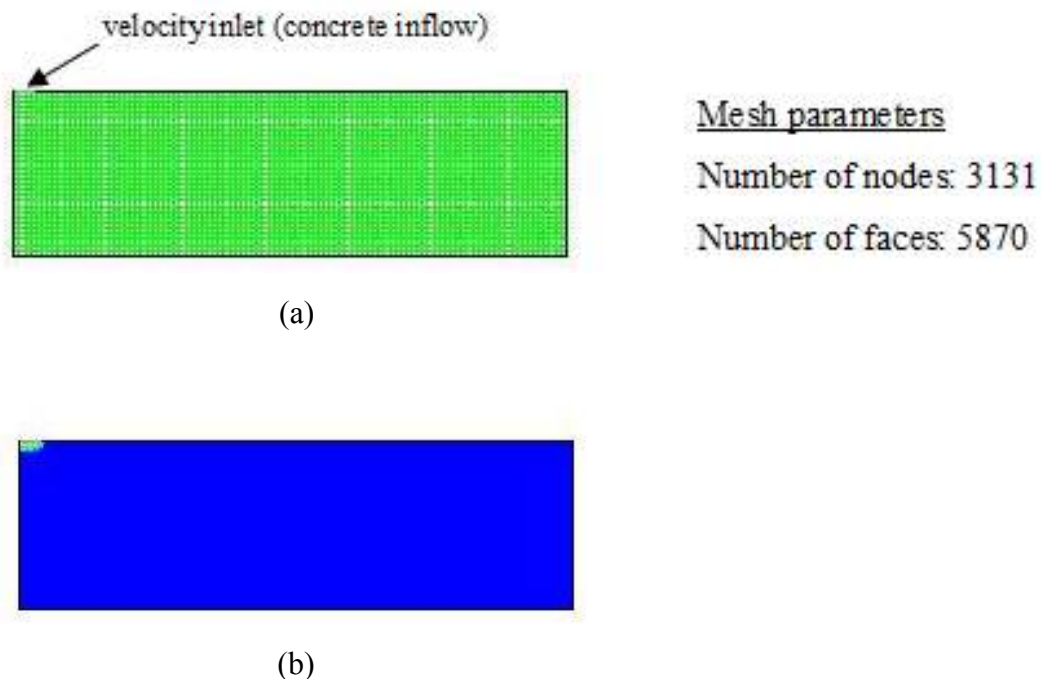


Figure 5.10: 2D Simulation of Slab Casting (a) Grid (b) Contours of SCC at  $t = 0$  sec.

### 5.4 NUMERICAL (CFD) SIMULATION OF THE WALL CASTING

Going by the same manner described section 5.2, the full-scale wall casting was simulated using FLUENT software package after the geometry creation and its discretization. Figure 5.11 shows the mesh used and the initial contours of SCC.

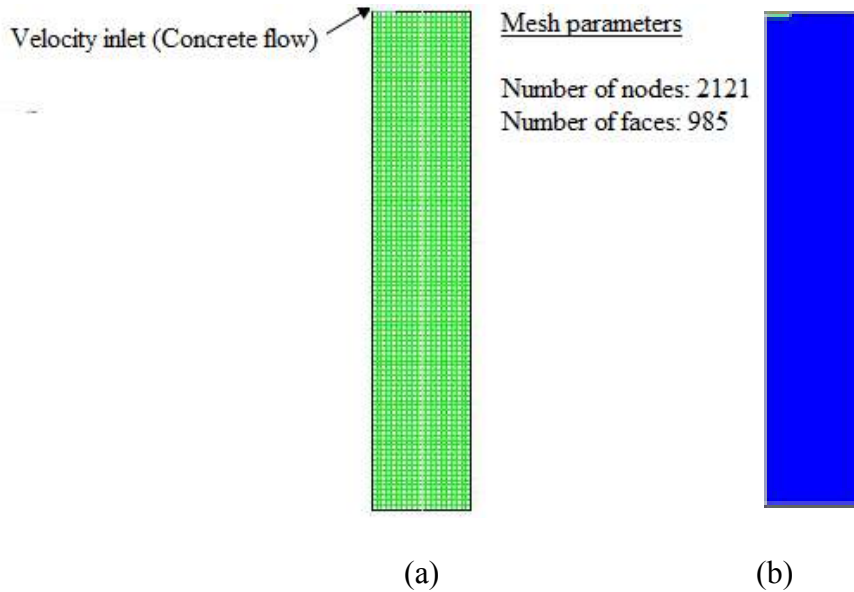
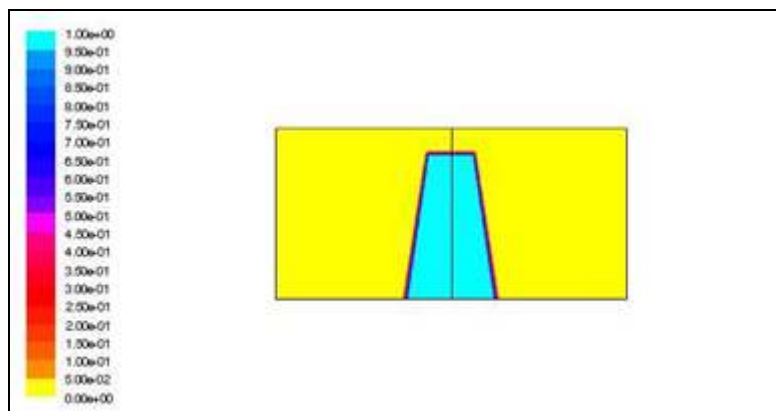


Figure 5.11: 2D Simulation of Wall Casting (a) Grid (b) Contours of SCC at  $t = 0$  sec.

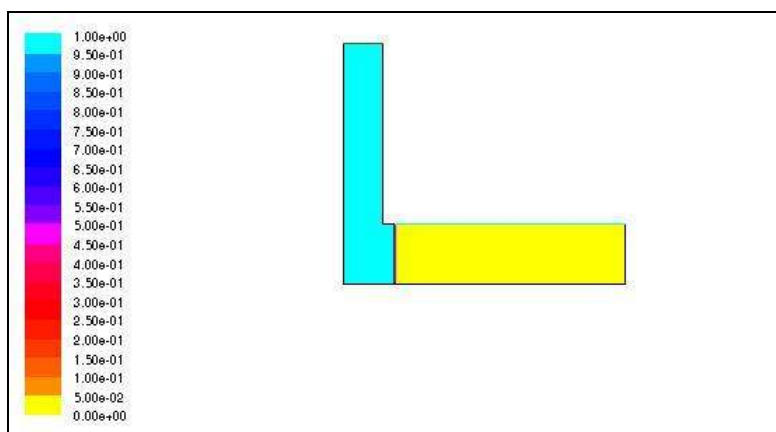
## 5.5 RESULTS OF THE NUMERICAL (CFD) SIMULATION OF SCC FLOW

### TESTS

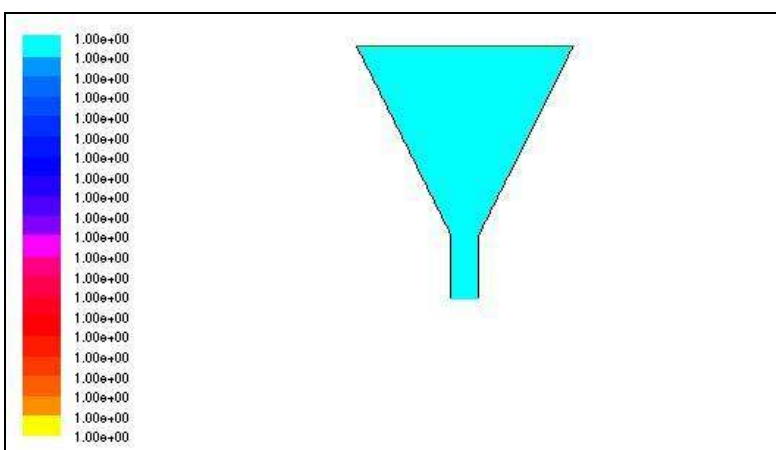
The results achieved at the end of the numerical simulation (using FLUENT) for the conventional tests on SCC carried out by Malik (2011) are presented in this section. The initial set-ups (time = 0) for the Slump flow, L-box, and V-funnel tests are shown in Figure 5.12 (a), (b) and (c) respectively. Contours of the volume fraction (ranging from 0 to 1) in the figure helps identify the instantaneous position of the SCC-Air interface in the domain modeled. Typical flow profiles for the mix made with 2.5% Silica fume are shown in Figs. 5.13, 5.14, and 5.15 for the Slump flow, L-box and V-funnel tests respectively. Every other mix modeled has similar flow topologies as the ones shown here, and these are given, comprehensively, in appendix A.



(a)



(b)



(c)

Figure 5.12: Contours of Volume Fraction of SCC at  $t = 0$  Sec.

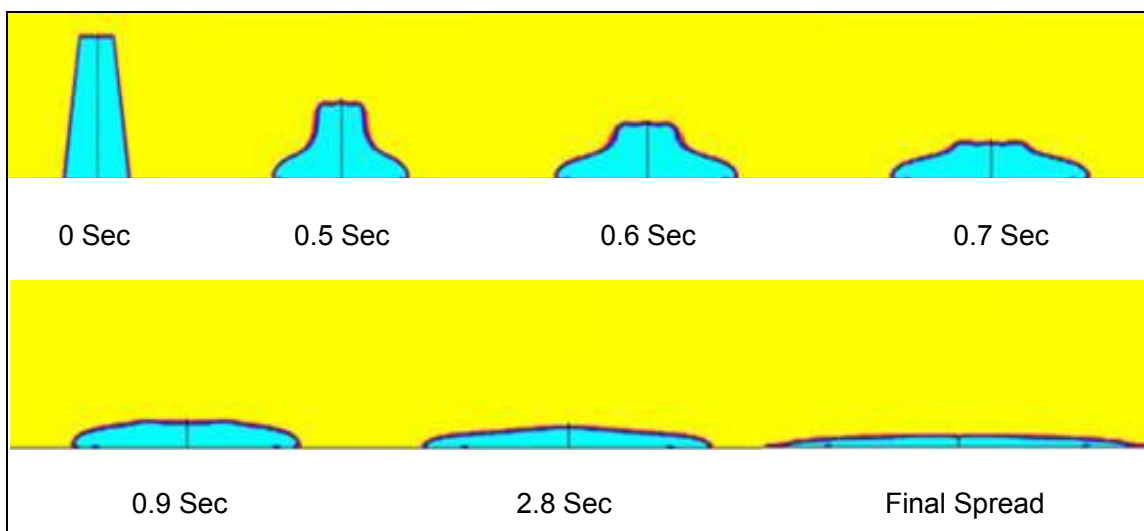


Figure 5.13: Typical Progressive Flow of SCC during the Simulation of Slump Test for 2.5% Silica Fume.

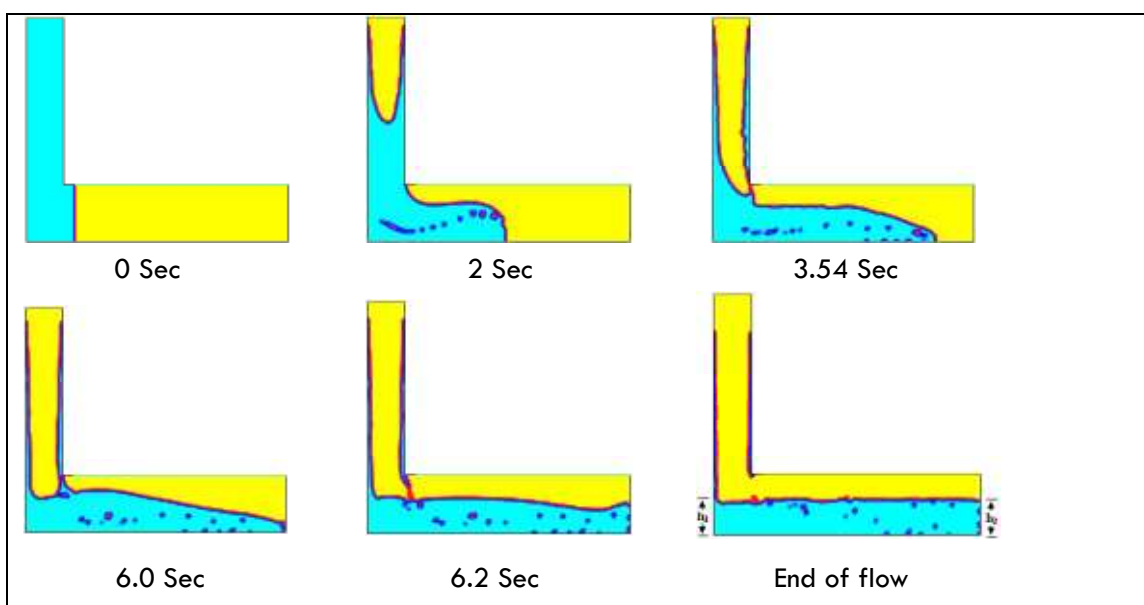


Figure 5.14: Typical Progressive Flow of SCC during the Simulation of L-box test for 2.5% Silica Fume.

It would be expedient to mention here that it is not the intent of the model's validation to assess the influence of the mineral admixtures used by Malik (2011) on the test results presented herein. Therefore, no attempt is made to go into such further details. Rather,

for the model validation, comparison is made between his experimental and the numerical simulations.

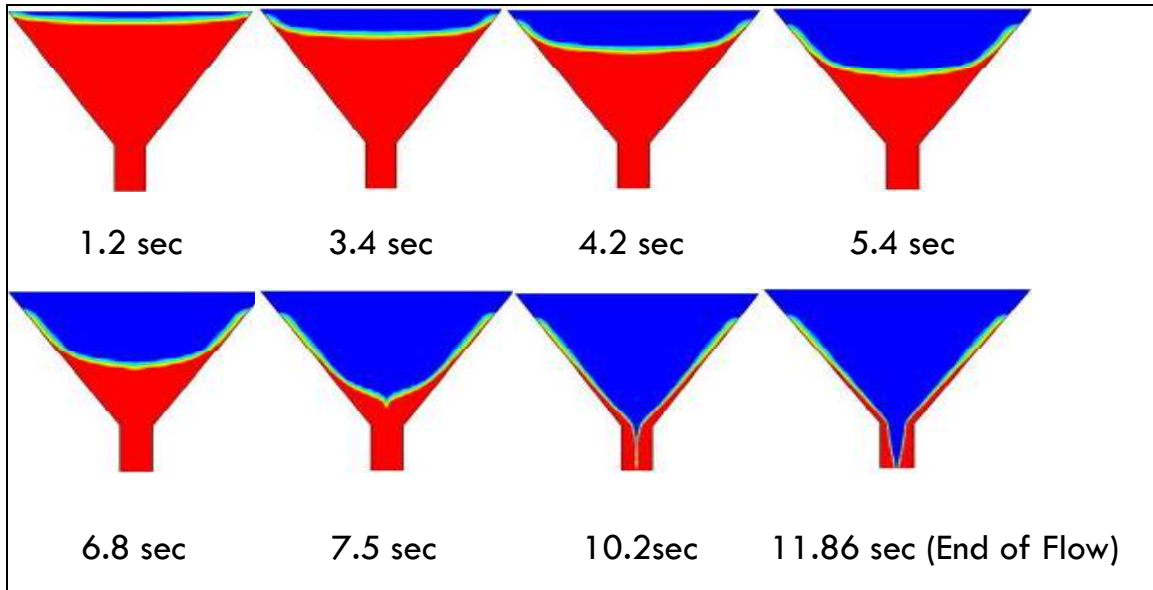


Figure 5.15: Typical Progressive Flow of SCC during the Simulation of V-funnel Test for 2.5% Silica Fume.

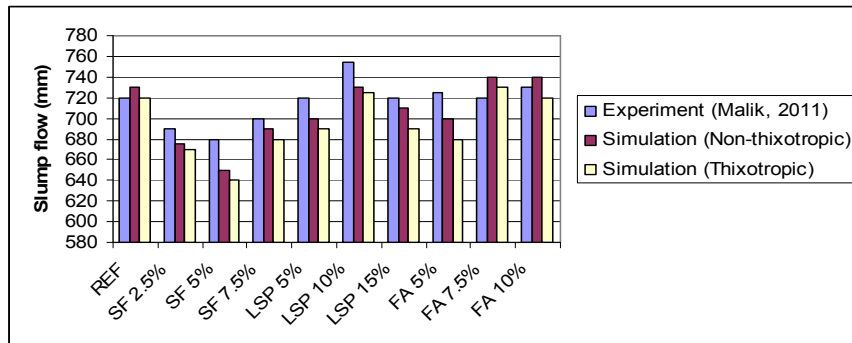
The summary of the results for all the mixes so modeled is given in tables 5.5, 5.6 and 5.7 for the Slump flow and T-50, L-Box, and V-funnel tests respectively. The graphical representations of these are also shown in Figs. 5.16, 5.17 and 5.18 for the Slump flow and T-50, L-box, and V-funnel tests respectively.

### 5.5.1 Slump Flow and T500 Test

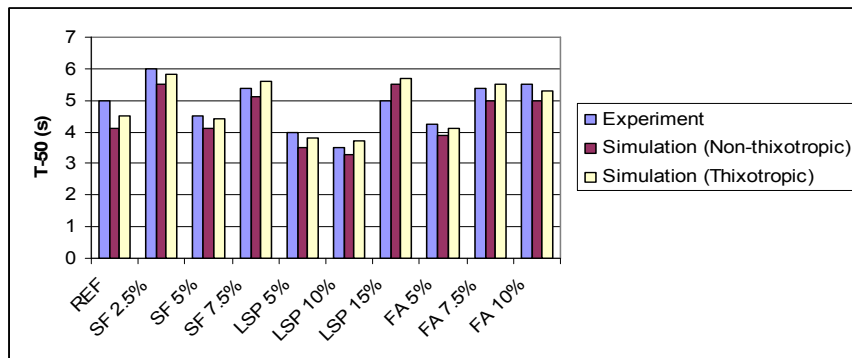
Both thixotropic and non-thixotropic simulations of the slump flow and Test give comparable results to the actual experimental ones. Although most of the slump flow readings obtained from the non-thixotropic simulation results are somehow lower than the experiments they are still within the allowable limits and, hence, acceptable. Few cases, like that of the reference mix and F.A 7.5% and F.A 10%, show the slump flow simulation results to be a little above those observed during the experiment. Despite

Table 5.5: Slump flow and T-50 Test Results.

Mix	Slump flow (mm)			T-50 (s)		
	Expt'l	Simulation (Non-thix.)	Simulation (Thixotropic)	Expt'l	Simulation (Non-thix.)	Simulation (Thixotropic)
REF	720	730	720	5	4.1	4.5
SF 2.5%	690	675	670	6	5.5	5.8
SF 5%	680	650	640	4.5	4.1	4.4
SF 7.5%	700	690	680	5.4	5.1	5.6
LSP 5%	720	700	690	4	3.5	3.8
LSP 10%	755	730	725	3.5	3.3	3.7
LSP 15%	720	710	690	5	5.5	5.7
FA 5%	725	700	680	4.25	3.9	4.1
FA 7.5%	720	740	730	5.4	5	5.5
FA 10%	730	740	720	5.5	5	5.3



(a)



(b)

Figure 5.16: Comparison between Experimental and Numerical Simulation for (a) Slump Flow, and (b) T-50 Tests.

the fact that the effect of thixotropy is neglected in the first phase of the modeling, it can be seen from Table 5.5 and Figure 5.16(a) that no much difference is observed. This is, however, expected to happen for the fact that in the actual laboratory experiments conducted, the fresh concrete was poured and tested immediately after mixing without any delay due to resting time, and at that time the flocculation may not have started. As a result, the non-thixotropic simulation results appear closer to the experimental result than the thixotropic model. Incorporating the thixotropic parameters of  $\alpha$  and  $\lambda_0$  as explained by Equation 5.7, relatively smaller values of slump flow were obtained for the same mixes modeled by neglecting the thixotropy. The parameters used in arriving at the thixotropic simulation models are for 1 minute resting time thereby resulting in little effect on the test results. As the resting time increases, more difference is bound to be observed.

The T-50 values obtained with and without the thixotropy effects also give a good result that compares well with the experiment (Figure 5.16 (b)). Just like the slump flow, the T-50 values for the non-thixotropic model were, in most cases, found to be a little lower than those from the experiment. In numerical simulation the self-weight of the virtual material (SCC) initially makes it flow relatively faster thereby resulting into smaller T-50 values after which the flow subsequently decelerates to give lower final spread values mainly due to decrease in the rate of shear from the material self-weight.

Incorporating the thixotropy effect into the model gave rise to T-50 values higher than those in which thixotropy was neglected. This reasoning is logically acceptable because the thixotropy model so incorporated will not allow a free flow of this material compared to the non-thixotropic one and, hence, longer time will be expected for it to reach the

50cm mark during the flow. The greatest discrepancy noticed between the thixotropic and non-thixotropic simulation is 20mm and 0.5 Seconds for the slump flow and T-50 respectively. In the case of the slump flow, this happened for the Lsp 15%, F.A 5% and F.A10% samples whereas for the T-50, it happened for the F.A 7.5%. However, despite all these, both the two numerical results achieved are acceptable and reliable enough to be used as predictive tools in addition to the available experimental results.

### 5.5.2 L-box Test

Figure 5.14 shows the simulation results for the L-box test of the mix containing silica fume. The height of SCC in the vertical column and its horizontal movement at various time intervals, as obtained from numerical simulation in FLUENT are shown in the figure. At 6.2 sec. the SCC has completely passed out of the vertical column into the horizontal section. Table 5.6 and Figure 5.17 show the simulation result obtained.

Table 5.6: L-box Test Results.

Mix	L-Box ( $\frac{h_2}{h_1}$ )		
	Experimental	Simulation (Non-thixotropic)	Simulation (Thixotropic)
REF	0.97	1	0.87
SF 2.5%	1	1	0.95
SF 5%	1	0.94	0.8
SF 7.5%	0.96	0.97	0.92
LSP 5%	1.13	1	0.95
LSP 10%	1.15	1	0.98
LSP 15%	0.93	0.92	0.87
FA 5%	1.15	1	0.94
FA 7.5%	0.86	0.8	0.76
FA 10%	1.5	1	0.97



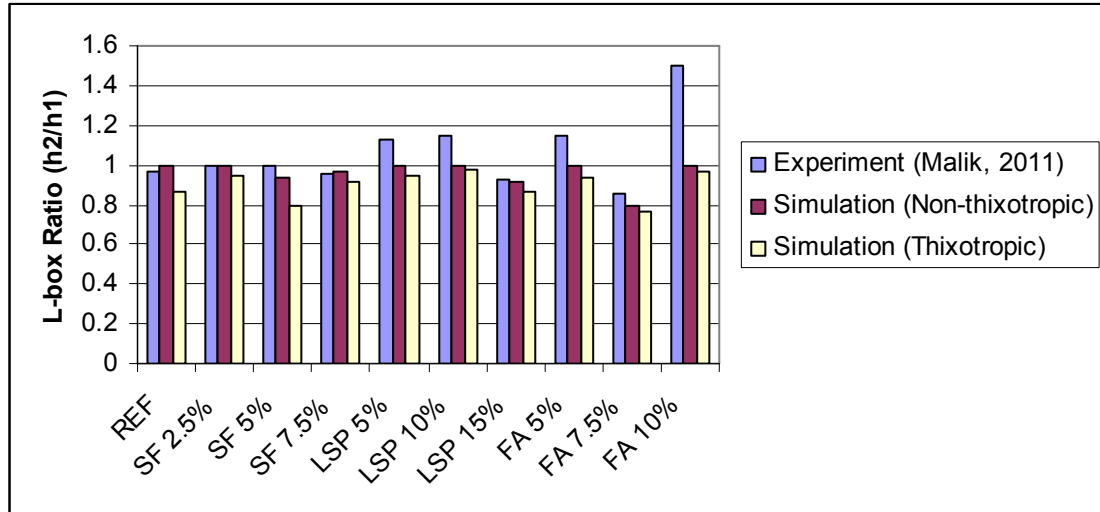


Figure 5.17: Comparison between Experimental and Numerical Simulation for the L-box Test.

The L-box ratio ( $h_2/h_1$ ) obtained from both numerical simulation and the experiment (Table 5.6 and Figure 5.17) for all the mixes shows slight differences between the thixotropic and non-thixotropic models. As expected, the L-box ratios obtained for the thixotropic model are lower than those of non-thixotropic ones in all the cases. This happened due to the same reason explained earlier in the thixotropic/non-thixotropic slump flow simulation.

### 5.5.3 V-funnel Test

Simulation results for the V-funnel test (Table 5.7 and Figure 5.18) show negligible difference between the thixotropic and non-thixotropic models. This is not surprising since the time needed to empty the funnel is not long enough to allow for the thixotropic, and hence flocculation, effect to prevail. The longest time reported from the experiment was 17 seconds (Malik, 2011) and can, still, be considered short enough to permit neglecting the thixotropic effect. In practice, this test method predicts the flow ability of

the fresh concrete being tested. A funnel test flow time in the range 6-12 seconds is recommended for concrete to be qualified as SCC.

Table 5.7: V-funnel Test Results.

Mix	V-funnel(s)		
	Experimental	Simulation (Non-thixotropic)	Simulation (Thixotropic)
REF	12	10.7	11.1
SF 2.5%	11.43	11.9	12.2
SF 5%	11	9.6	9.8
SF 7.5%	12	10.2	10.5
LSP 5%	14	12.8	13.1
LSP 10%	17	14.3	14.6
LSP 15%	10	8.3	8.7
FA 5%	13	12.8	13.3
FA 7.5%	12	11.1	11.4
FA 10%	11.26	10.4	10.7

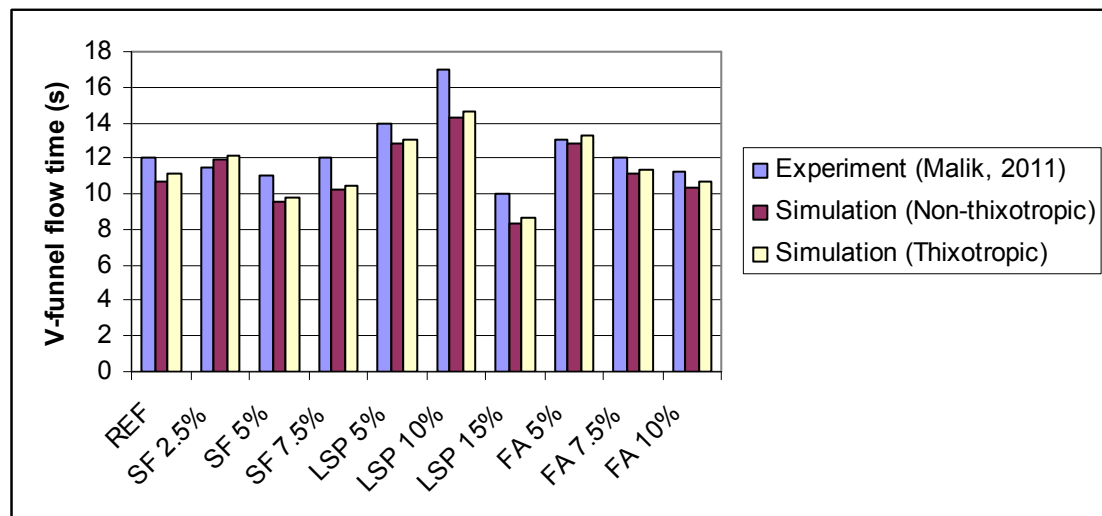


Figure 5.18: Comparison between Experimental and Numerical Simulation for the V-funnel Test.

All the V-funnel experimental test results reported by Malik (2011) satisfy this criterion except the case of Lsp 5% and Lsp 10% which have flow times of 14 and 17 seconds respectively. Hence, as a simple and effective tool to globally characterize the SCC fluidity, the V-funnel test results obtained from the experiment and simulation qualify all the mixes as satisfactory except for the two mentioned above.

It is worth noting that much additional information regarding the flow behavior of this material is obtainable by this simulation tool. In the laboratory or field, these type of tests do not give more than one or two parameters; Time of emptying the funnel and probably  $T_{5min}$ . The latter is used to indicate the tendency for segregation, wherein the funnel can be filled with concrete and left for 5 minutes to settle. If the concrete shows segregation, the flow time will increase significantly. With this model, however, the distributions of flow velocity, pressure, shear stresses, density, and molecular viscosity to mention but a few within the material can all be studied in addition to the time of emptying the funnel and  $T_{5min}$ . It is the flexibility of studying these and many more parameters that makes the simulation tool more versatile than the experiments. The simulation, however, does not substitute the experimental works and whenever the need arises, experiments should be conducted in order to verify the reliability of the model.

## **5.6 RESULTS OF THE NUMERICAL (CFD) SIMULATION OF SLAB CASTING**

Results achieved at the end of the full-scale slab casting were used in validating the CFD simulation of the same element. Calibrating the model with  $\tau_0=34\text{Pa}$ ,  $\mu=36\text{Pas}$  (Herschel-Bulkley model) and a discharge of  $2.7 \times 10^{-3} \text{ m}^3 / \text{s}$ , an excellent correlation was observed between the experiment and numerical simulation as shown in Table 5.8 and Figure 5.19.

Table 5.8: Experimental and Numerical Simulation Result for the Full-Scale Slab Casting.

H (cm)	Time (s)	
	Experimental	Simulation
5	19.1	17.97
10	34.5	33.57
15	53.3	56.37
20	86.2	83.97
25	114.5	110.97

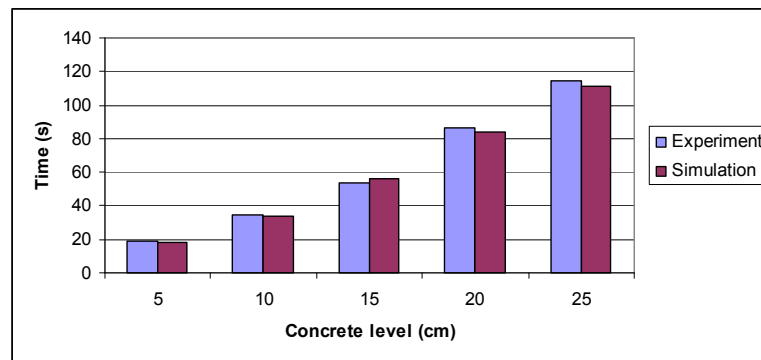


Figure 5.19: Comparison between Experiment and Numerical Simulation for the Slab Casting Process.

The minor discrepancies observed may be attributed to the partial fluctuation of the discharge during the actual experimental measurements which was not so observed during the simulation.

Figure 5.20 shows the progression of the flow profile of the simulation during the slab casting process. An important feature worth mentioning in the simulation of the casting process of the above slab is the proper choice and calibration of the SCC rheological properties that resulted in a smooth flow profile (as observed during the experiment) without the need for constantly shifting the supply hose from one point to another before getting a proper filling behavior. That is the reason why the SCC level increases almost

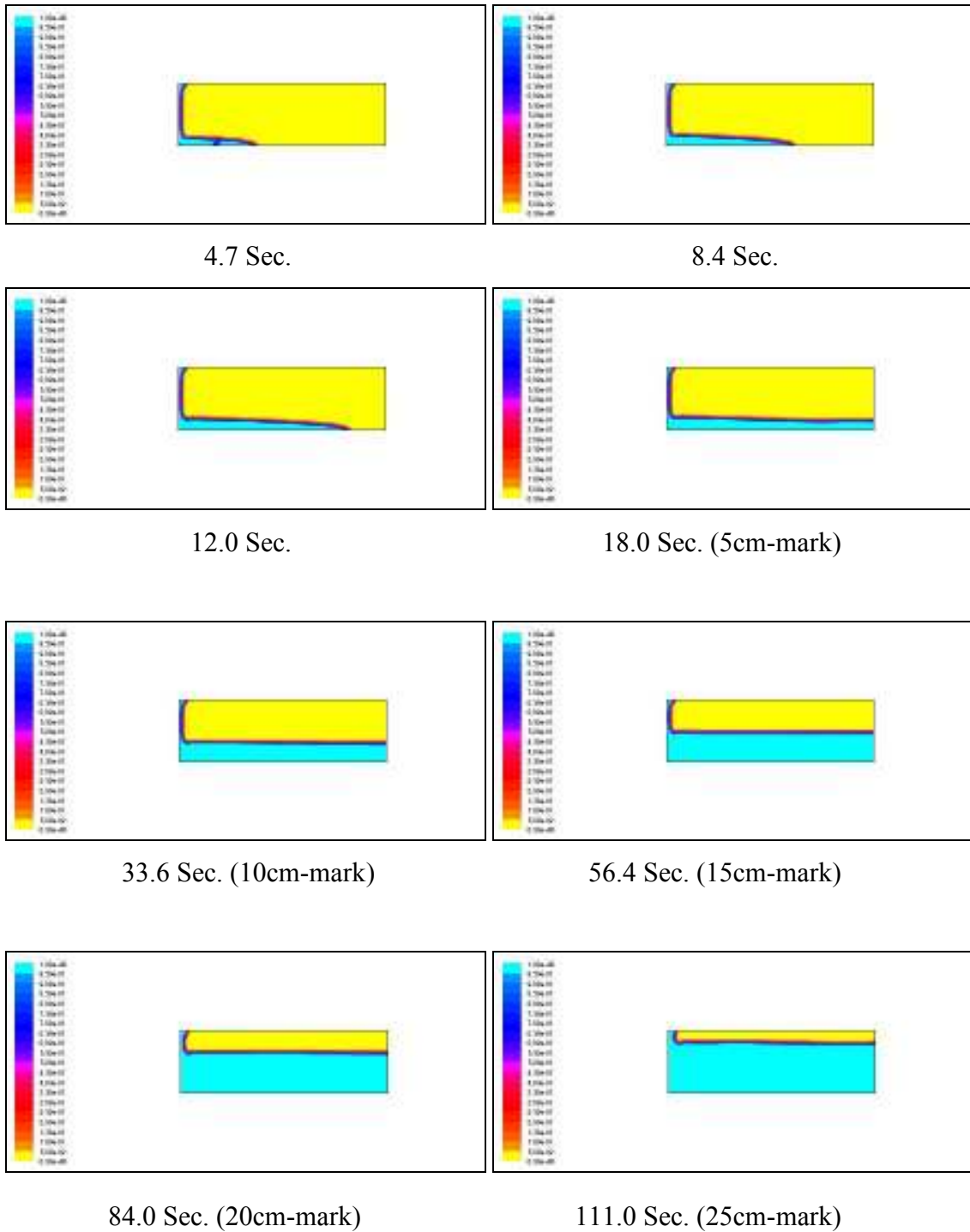


Figure 5.20: Progressive Flow of SCC during the Simulation of Full-Scale Casting of the Slab.

uniformly throughout the formwork modeled as shown in Figure 5.20. However, an improper design of this material may result in a stiff SCC that can result in difficulties in

its free flow and filling ability. This idea was modeled and the flow profile shown in Figure 5.21. A choice of the rheological properties of  $\tau_0 = 100 Pa$  and  $\mu = 90 Pas$  showed an unsatisfactory form-filling ability as can be clearly observed in the figure. This stiff material deviates from the requirements of acceptable SCC for the case being considered here. The last profile in the same figure suggests the necessity to move the supply hose further away before the form can get filled satisfactorily since the material at the hose's location reaches its maximum possible height whereas the remaining portion remains too solid to flow and fill everywhere. In more complicated structures, this phenomenon can lead to the problems of honey-combing and the likes: Even in the relatively simple slab element modeled here, some air pockets can be seen in the material shown in Figure 5.21.

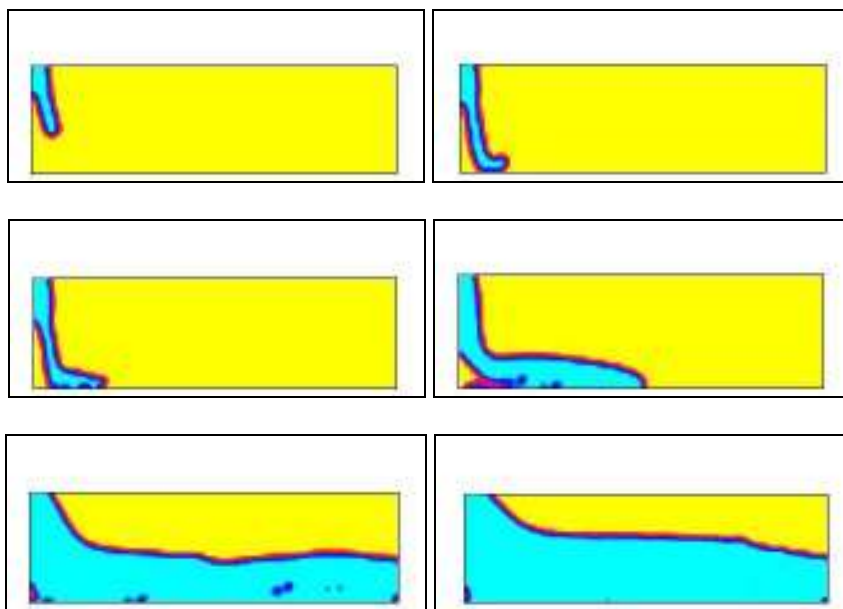


Figure 5.21: The Flow Profile of a Typical SCC Mix Too Stiff to have a Satisfactory Filling Ability.

## 5.7 RESULTS OF THE NUMERICAL (CFD) SIMULATION OF WALL CASTING AND RESULTING FORMWORK PRESSURE

Experimental and CFD simulation results of the wall casting process to study the formwork pressure due to SCC carried out are presented here. Readings obtained at the end of the casting operation are that of lateral pressure at intervals of 15 seconds. From these, a relationship between pressure and height ( $P = \rho gh$ ) was used to estimate the approximate heights corresponding to the pressure readings obtained and the results are shown in Table 5.9. The heights obtained increases from zero to a maximum of 1m except between 0.75m and 0.72m. This happened as a result of the experimental pressure reading saved by the data logger where it can be observed, from the second row of Table 5.9, that a drop in pressure from 16.5Kpa to 15.8Kpa was recorded. It can be attributed to the dynamic effect because of the manner (partially alternating discharge) in which the SCC was discharged from the hose. Although the simulation was ran with such errors eliminated, still the corresponding value of pressure at the height of 0.72 from the simulation is shown for the sake of comparison. Same rheological properties ( $\tau_0 = 34Pa$  and  $\mu = 36Pas$ ) calibrated during the slab simulation were used in the simulation of the wall casting.

Table 5.9: Experimental Pressure Measurements and Numerical Simulation during the Vertical Wall Casting Process.

Height (m)	0	0.06	0.16	0.32	0.50	0.53	0.75	0.72	0.79	0.85	1.0
P-experiment (Kpa)	0	1.3	3.4	6.9	11	11.7	16.5	15.8	17.2	18.6	20.8
P-simulation (CFD) (Kpa)	0	1.27	3.29	6.76	10.5	11.4	15.9	15.5	16.6	18.1	20.1
Hydrostatic Pressure ( $\gamma h$ ) (Kpa)	0	1.31	3.5	7.0	10.9	11.6	16.4	15.8	17.3	18.6	21.9

Figure 5.22 shows the progression of the flow profile of the simulation during the wall casting process, whereas Figure 5.23 shows the contours of the lateral pressure obtained numerically at the end of the casting operation (20.1Kpa).

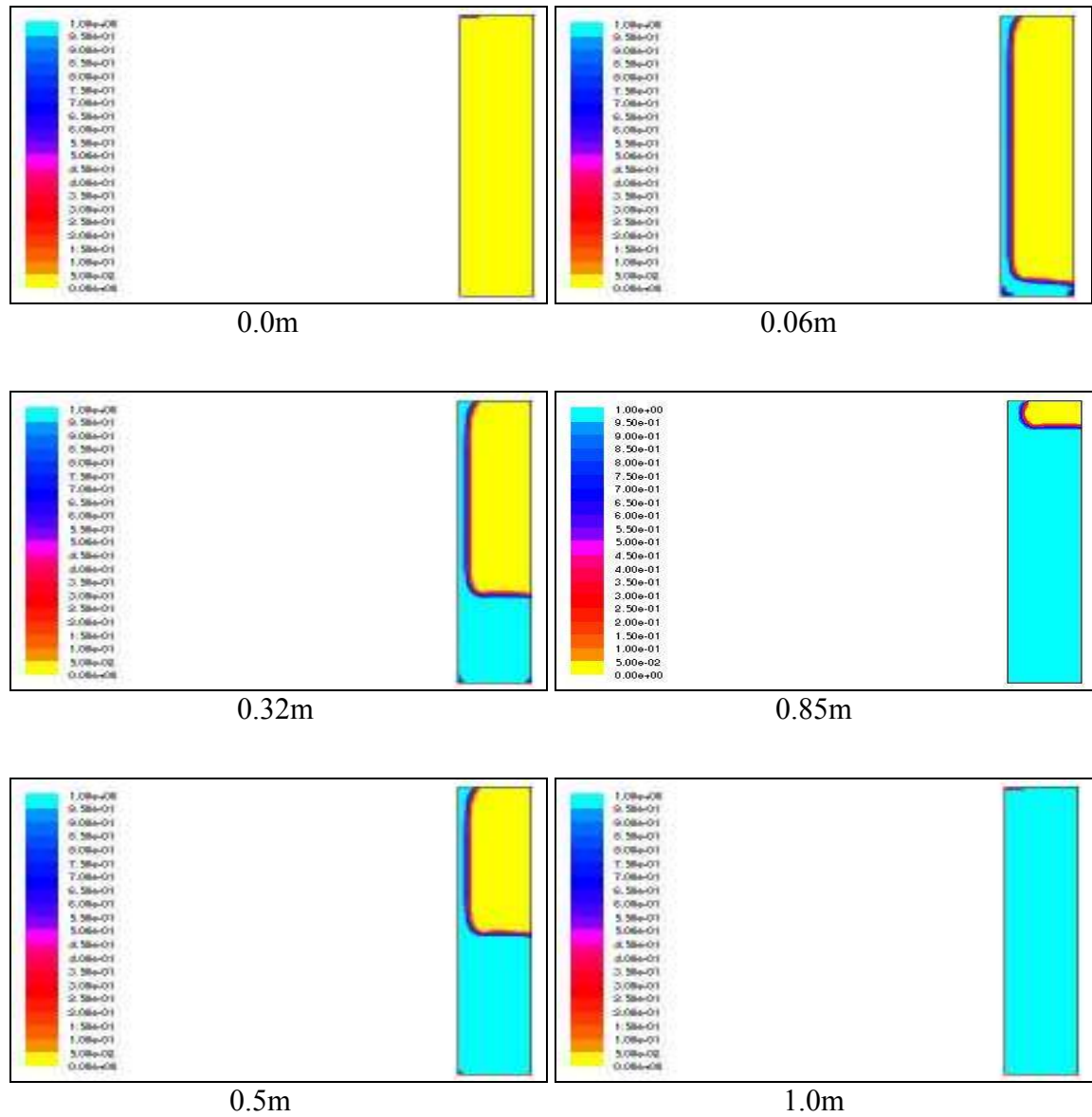


Figure 5.22: Progressive Flow of SCC During the Simulation of Full-Scale Casting of the Wall.



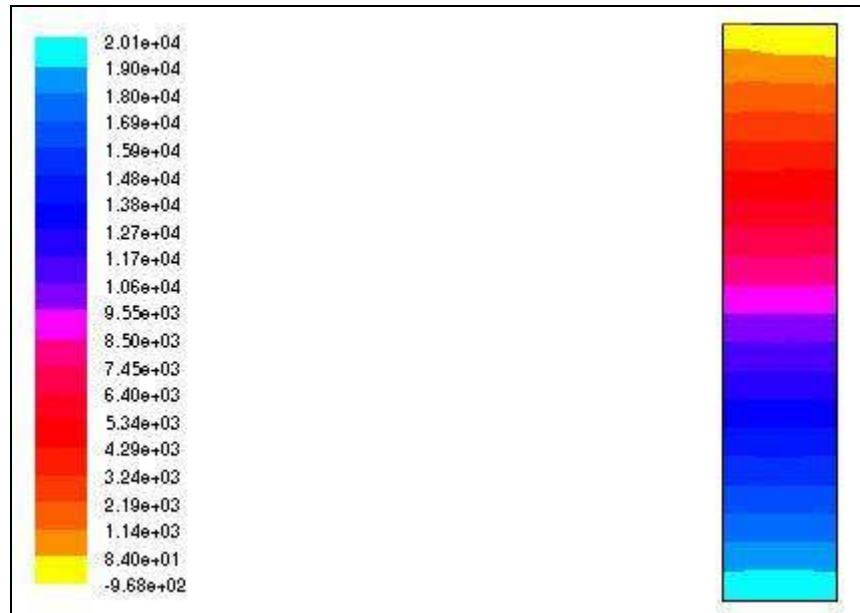


Figure 5.23: A CFD Solution for the Lateral Pressure Exerted on the Formwork at the End of Casting.

As seen in Table 5.9, good agreement is evident between the experimental and CFD simulation results for the pressure exerted on the formwork. Both the two results resulted in maximum pressure reading a little below the hydrostatic value.

## CHAPTER SIX

### FINITE ELEMENT MODEL DEVELOPMENT AND SIMULATION RESULTS FOR THE EVOLUTION OF SCC FORMWORK PRESSURE

#### 6.1 GENERAL

Study of the behavior of lateral formwork pressure exerted by self-compacting concrete (SCC) is important for safe and economical design of formworks. Many designers may be tempted to design formworks to withstand the maximum hydrostatic pressure due to the high fluidity of SCC thereby increasing the cost and limiting the allowable placement heights. Formwork pressure is influenced by thixotropy behavior of SCC; rapid flocculation of this material after it is placed in formworks results in significant reduction in the pressure. Numerical modeling can be an invaluable tool to aid in predicting the factors likely to affect the rate of evolution of formwork pressure for SCC.

In this chapter, a new finite element model is proposed for computing and studying the evolution of lateral pressure evolution in self-compacting concrete incorporating the factors such as the casting rate and the evolution of rheological properties of SCC. The model presented considers the SCC as a homogeneous isotropic linear elastic material below the yield stress confined in an elastic medium of density  $\rho$  in a rigid formwork.

The approach utilized here involves solving for the unknown stresses using a 2-D plain strain finite element model. The boundary shear stress values at different locations vary depending of the interval of time from the casting of the portion under consideration to the instance at which the pressure measurement was made (resting time).

The finite element model proposed in this study is meant to model the evolution of formwork pressure within the first few hours after casting before the hydration starts. Purely thixotropic behavior can not be achieved after the onset of hydration and as a result, such regimes are not of much interest.

## 6.2 DEVELOPMENT OF MODEL FOR THE FORMWORK PRESSURE

### 6.2.1 Treatment of Boundary Conditions

The coordinate system and formwork geometry for the finite element model development is shown in Figure 6.1.

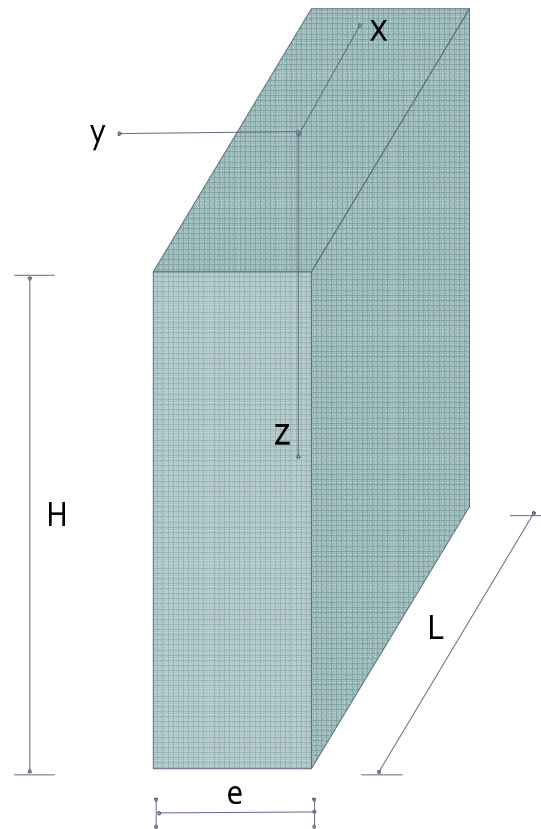


Figure 6.1: Formwork Geometry and Coordinate System.

The treatment of the boundary shear stress conditions in this study is based on the work of Roussel (2006) explained in section 2.2 under the literature review. All the parameters

explained in the section ( $A_{thix}$ ,  $T$ ,  $\lambda$  and  $\alpha$ ) can be computed through rheological measurements conducted on the SCC. The flow history determines the flocculation state. The thixotropic apparent yield stress due to flocculation  $\lambda_0\tau_0$  is also equal to zero immediately after mixing. Through the successive steps in the casting process,  $\lambda_0$  will evolve from its initial zero value to a positive value and an apparent yield stress greater than the initial yield stress will appear.

Ovalez and Roussel (2006) suggested that  $\tau_0$  in Equation 2.10 can be neglected due to its relatively small magnitude compared to that due to resting and flocculation ( $A_{thix}t_{rest}$ ). Where  $t$  in the equation is substituted with  $t_{rest}$  to emphasize on the fact that it represents a resting time. Therefore, one can write

$$\tau(t) = A_{thix}t_{rest} \quad (6.1)$$

Starting the casting at a time  $t_{rest} = 0$ , successive layers of this material will be deposited resulting in the final topmost layer having the least resting time. As a result, a linear variation in  $\tau(t)$  will be expected (Figure 6.2).

The model proposed in this work treats the time-dependent boundary shear stress  $\tau(t)$  using discrete spring elements of stiffness  $k$  as shown in Figure 6.3.

Since the use of the stiffness  $k$  aims at simulating the distribution of  $\tau(t)$  along the vertical edges it is necessary to devise a means of linking  $k$  to some type of time dependent relationship taking into consideration the rheological properties of SCC. Hence, the use of  $k(t)$  instead of just  $k$  seems more appropriate. By definition, stiffness is defined as force per unit length. Thus, taking a tributary length  $y$  multiplied by

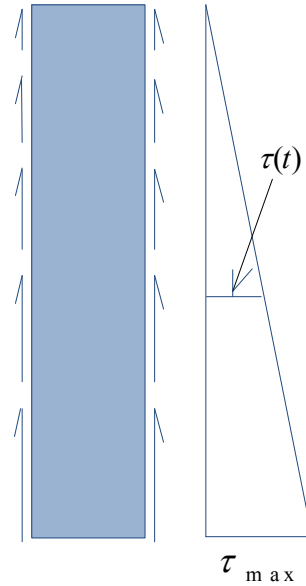


Figure 6.2: 2D Boundary Shear Stress Distribution as a Function of the Resting Time.

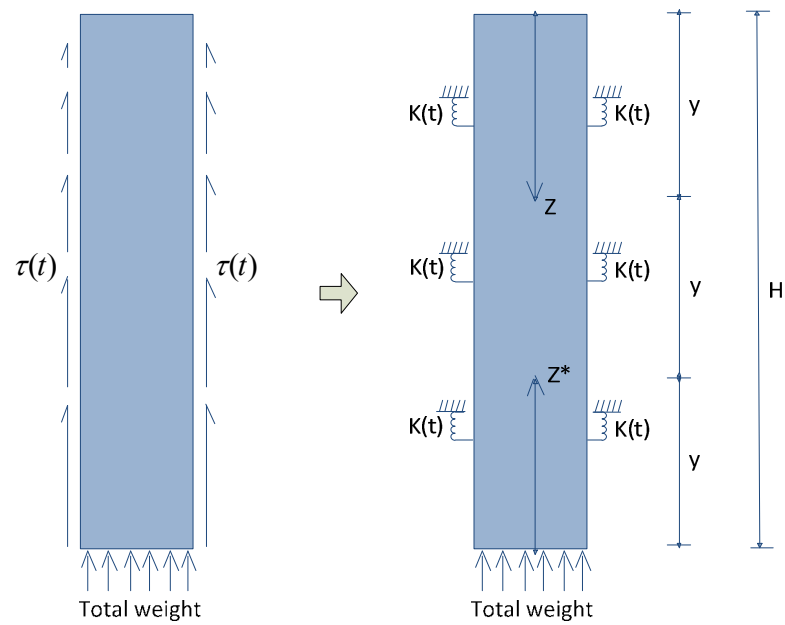


Figure 6.3: Physical Model of the Shear Boundary Condition using Discrete Springs of Time-Dependent Stiffness  $k(t)$ .

$\tau(t)$  yields equivalent spring force. Denoting the local vertical deformation by  $u_y$ , one writes the “time-dependent” spring stiffness as follows

$$k(t) = \frac{\tau(t) \times y}{u_y} \quad (6.2)$$

Using Equation (6.1) for  $\tau(t)$ , Equation (6.2) yields

$$k(t) = \frac{A_{thix} \times t_{rest} \times y}{u_y} \quad (6.3)$$

The casting rate  $R$  has an effect on the value of  $\tau(t)$ , and hence on the value of  $k(t)$ , and so plays a role too in the evolution of the lateral stress since the resting time  $t$  is dependent on it through,

$$R = \frac{H}{t} \quad (6.4)$$

At an instance of time,  $t^*$  (before the formwork gets filled up) the material rises to a depth  $z^*$  and this time is given by

$$t^* = \frac{z^*}{R}, \quad 0 < z^* < H \quad (6.5)$$

and  $z + z^* = H$

Thus, the resting time  $t_{rest}$  of any particular layer at a depth  $z$  from the bottom of the formwork will be given by

$$t_{rest} = (t - t^*) = \left(t - \frac{z^*}{R}\right) \quad (6.6)$$

Therefore, Equation (4.15) can be written as

$$\tau(t) = A_{thix} \left( t - \frac{z^*}{R} \right) \quad (6.7)$$

Eq. (6.6) suggests that the bottom layer will have the highest resting time than all the other successive layers cast above it.

Hence, for casting rate-dependent stiffness, Equation (6.3) in terms of  $R$  using Equation (6.6) gives

$$k(t) = \frac{A_{thix} \times \left( t - \frac{z^*}{R} \right) \times y}{u_y}, \quad 0 \leq t \leq \frac{H}{R} \quad (6.8 \text{ a})$$

$$k(t) = \frac{A_{thix} \times \left( t + \left( \frac{H - z^*}{R} \right) \right) \times y}{u_y}, \quad t > \frac{H}{R} \quad (6.8 \text{ b})$$

Where Equation (6.8 a) applies to the case in which  $t$  starts from the start of casting and Equation (6.8 b) to that in which  $t$  starts immediately after casting is completed.

### 6.2.2 Solution of Problem in ANSYS Environment

To analyze the concrete material the proposed model was solved using ANSYS finite-element software (ANSYS inc., 2007). The two-sided vertical wall formwork was analyzed for different experimental results available in the literature. The geometry of the formwork is already described in Figure 6.1. Due to the fact that wall formworks are sufficiently long in one direction which can be simplified into a 2-D model, use of plane strain element was made.

Eight-node plane elements were used to simulate the fresh concrete. Spring-damper element type was used to model the interaction between the fresh concrete and the

formwork. The 2-D longitudinal spring-damper is a uniaxial tension-compression element with two degrees of freedom at each node: translations in the nodal  $x$  and  $y$  directions. This element was placed at discrete location along the vertical exterior boundaries of the fresh concrete. Since the aim is study how the lateral pressure evolves with time, the discrete spring stiffness coefficients are calculated using either of Equations 6.8(a) or (b) (depending on the time the pressure measurement starts). Hence at each time step, the stiffness coefficient changes and, hence, the approach treats the springs with time-dependent stiffnesses. Material properties are entered including the values of  $E$  and  $\nu$ . Treating the SCC material as an incompressible fluid,  $\nu \approx 0.498$  was used to take care of the numerical errors that will result when a value of exactly 0.5 is used. A value of 7 Gpa was used for the elastic modulus,  $E$ . The flowchart shown in Figure 6.4 illustrates this idea.

The discretization of the concrete domain was achieved using a very fine mesh size (Figure 6.5 (a)) and the boundary conditions (Figure 6.5 (b)) used includes; (i) Rollers at the two vertical sides to restrain any horizontal movement while the vertical one is free, (ii) Rollers at the base of the formwork to allow free horizontal movement while restraining the vertical one, and (iii) Fixed joints/nodes at the ends of the spring elements.

### **6.3 THE PROPOSED FINITE ELEMENT MODEL (FEM) PREDICTIONS VERSUS EXPERIMENTAL MEASUREMENTS**

In order to validate the proposed model's ability to predict the lateral stresses exerted by SCC on formwork, experimental results obtained from the full-scale wall casting described in chapter four and some additional ones from existing literature were utilized.

Use was made of the ANSYS commercial software to solve for the unknown stresses.



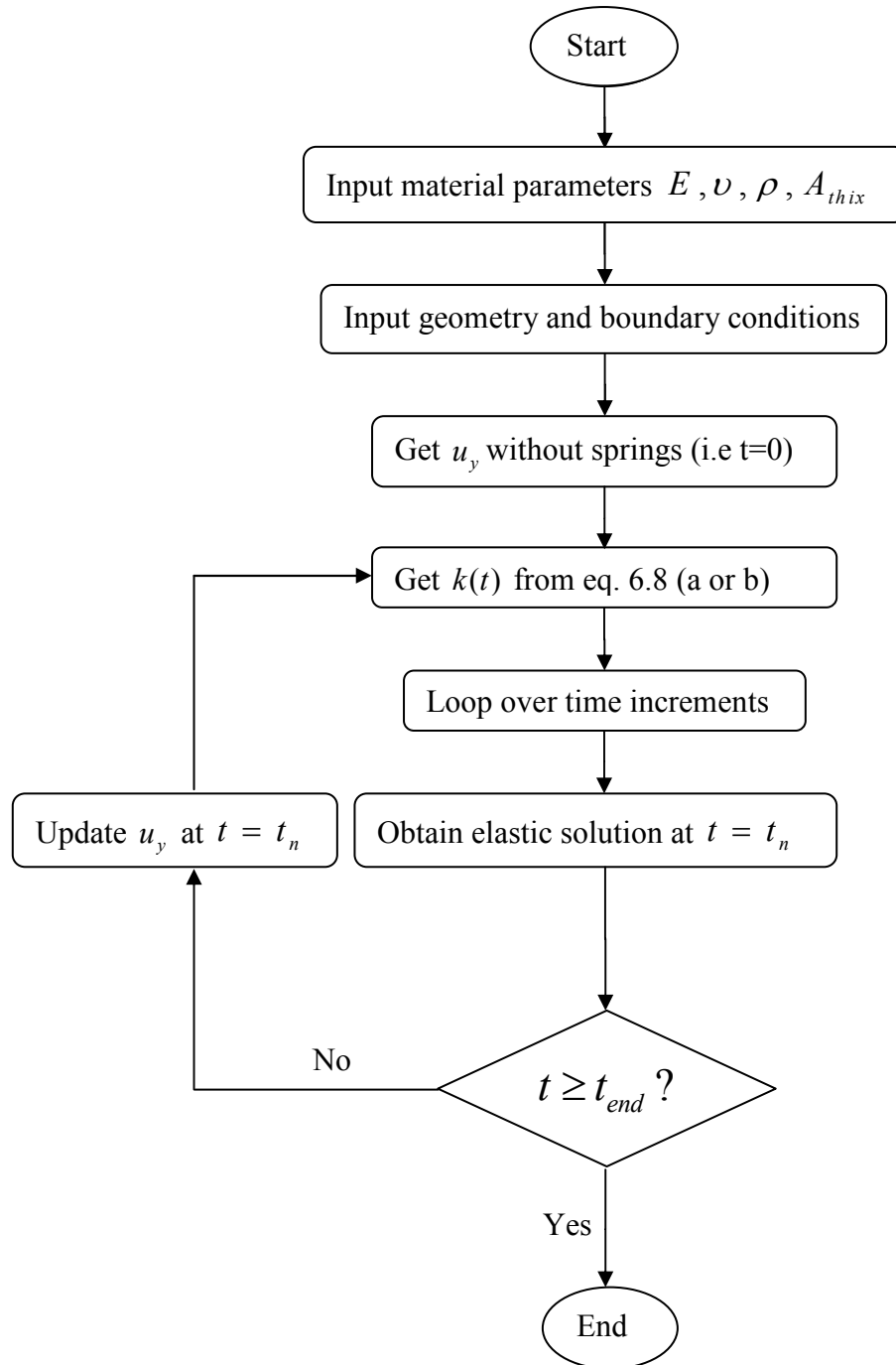


Figure 6.4: Interdependency between the Steps in Solving the Problem.

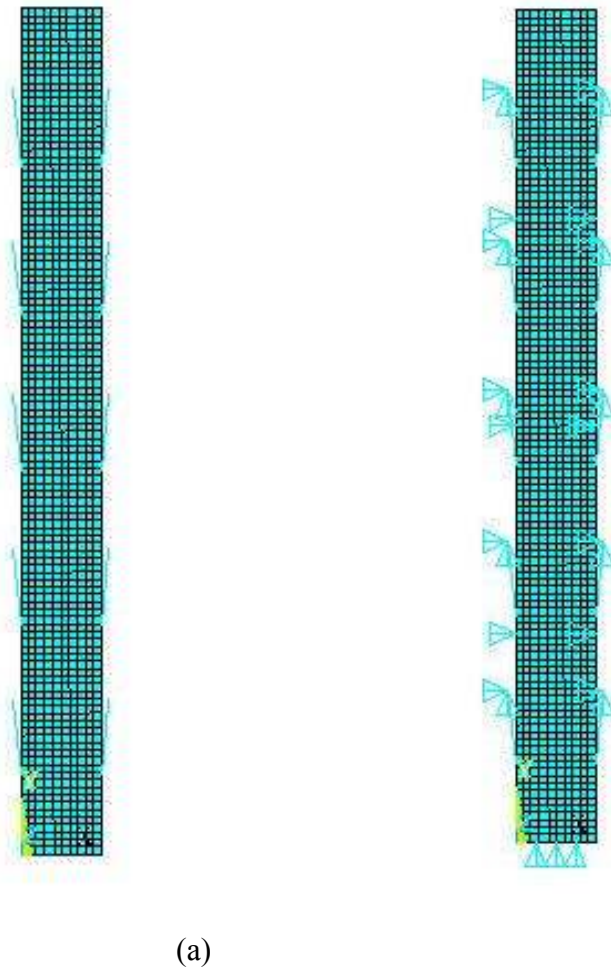


Figure 6.5: Domain of the Modeled Fresh Concrete showing (a) Discrete Spring Elements and Meshing (b) Boundary Conditions.

However, as the model is meant to capture the evolution of lateral stress with time after casting, it is important to mention that the model's validation using the conducted experiment corresponds to the pressure achieved immediately after casting (time = 0). More comprehensive validation of the model developed (taking into consideration the timely variation of the pressure) is done utilizing experimental results from existing literature as presented in the subsequent sections.

Figure 6.6 shows the finite element solution of the vertical wall cast using the selected mix-design of SF2 10% (table 4.1). As seen from the contours of the lateral stress

immediately after casting, a maximum value of 20.2Kpa at the location of the base pressure transducer was obtained. This compares well with the result obtained from the experiment (20.8Kpa) and that obtained from the numerical simulation using CFD (20.1Kpa) as shown in Figure 6.7. Both the CFD simulation result and that of the proposed finite element model resulted in maximum pressure reading a little below the hydrostatic value (22Kpa).

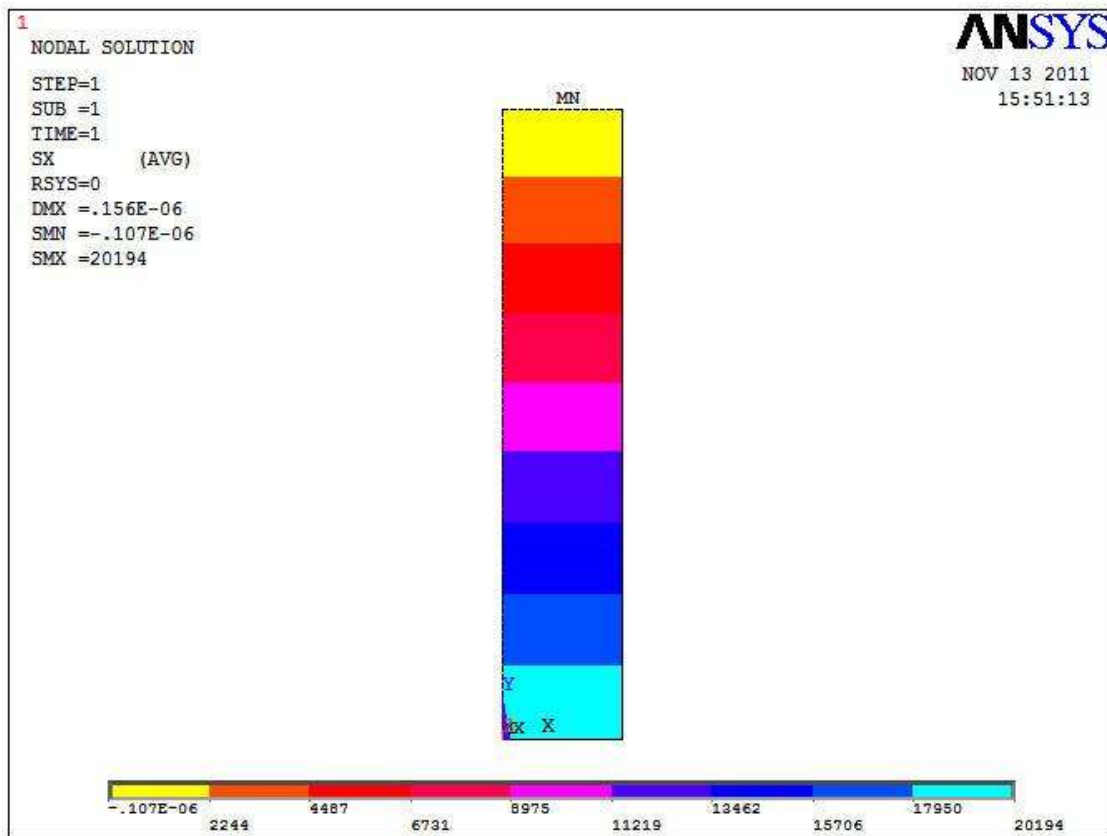


Figure 6.6: A finite Element Solution using the Proposed Model for the Lateral Pressure Exerted on the Formwork at the End of Casting.

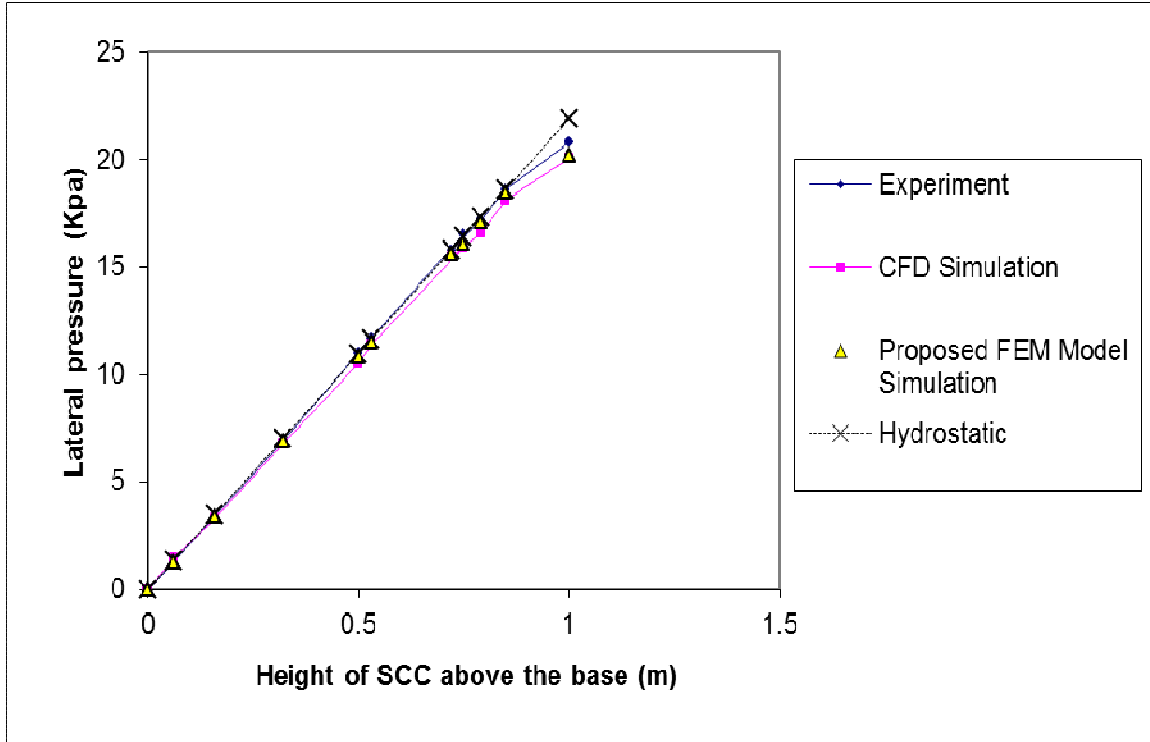


Figure 6.7: Comparison between Experimental, Finite Element and CFD Simulation Results for the Lateral Pressure Variation at the Base of the Wall Formwork at Various Casting Heights.

### 6.3.1 Decay of Lateral Pressure with Respect to Time

To illustrate the response of the model developed in this research based on timed measurements of the pressure exerted on formwork by SCC, experimental results obtained from Khayat et al. (2005) and Gregori et al.(2008) were utilized here. In (Khayat et al. 2005), effect of casting rate on maximum pressure at the base of an instrumented column was determined as part of the objectives of their study. They made use of two types of experimental columns, one measuring 2.1 m in height and 0.2 m in diameter and the other 3.6 m in height and 0.92 m in diameter. For the 2.1 m high column, two different casting rates were used, namely 10 m/hr and 25 m/hr and the variations (with time) of the ratio of stress determined from the bottom sensor to the corresponding hydrostatic pressure was obtained as reported in their paper.

Based on their results for the 2.1 m high column, Ovarlez and Roussel (2006) validated their analytical model for maximum lateral stress due to SCC. However, to do that, and since Khayat et al. (2005) had not reported a value for  $A_{thix}$ , Ovarlez and Roussel calibrated their model by suggesting a value of  $0.2 Pa/s$  for the flocculation coefficient ( $A_{thix}$ ). This value fitted well and resulted in close agreement between their model and the experimental result reported by Khayat et al. (2005). The use of  $A_{thix} = 0.2 Pa/s$  suggested that the material is somehow low thixotropic according to the work reported by Roussel (2006) shown in table 2.1.

Using the same value of  $A_{thix}$  suggested above ( $0.2 Pa/s$ ), the model presented in this research was able to predict the variation of the lateral pressure with time at the base of the 2.1 m high column experimented by Khayat et al. (2005). Figs 6.8 and 6.9 show the plots of these comparisons for two casting rates,  $R = 25m/hr$  and  $R = 10m/hr$ , respectively. As shown in these, close agreement is obtained between the proposed model and the experimental results. The maximum relative lateral pressure prediction of this same material was evaluated using the model proposed by Roussel (2006) to be about 0.95 and 0.975 for casting rate of  $10m/hr$  and  $25m/hr$  respectively and it only predicts for  $t = 0$ . These compare well with the prediction by the proposed model here (0.955 and 0.965 respectively) which in addition predicts these ratios for various timings. In addition, the model developed here was able to predict the influence of casting rate on relative lateral pressure in the same way Khayat et al. (2005) reported it. Figure 6.10 shows the influence of the rate of placement (casting) on lateral pressure for the 2.1 m high column. Though both the two casting rates depict the same slope of pressure drop, it

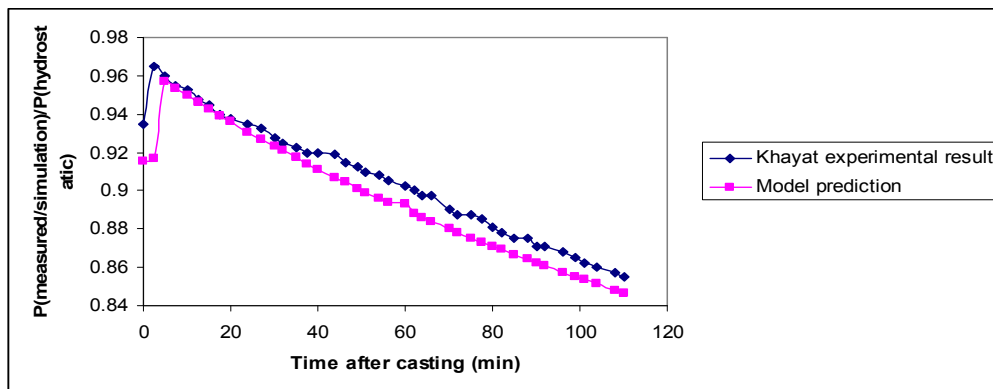


Figure 6.8: Comparison between Literature Experimental Results [Khayat et al., 2005] and Predictions of the Proposed Model for the Evolution of Base Relative Lateral Pressure with Time after Casting at a Rate of  $R=25m/hr$ .

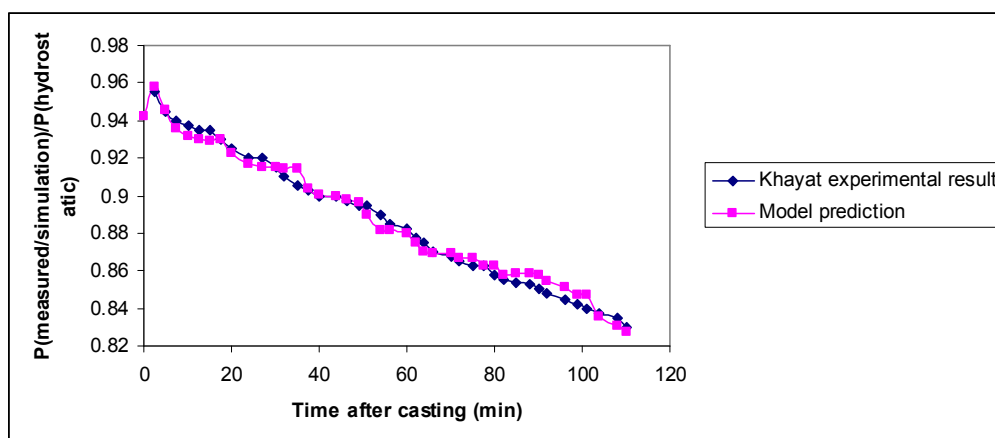


Figure 6.9: Comparison between Literature Experimental Results [Khayat et al., 2005] and Predictions of the Proposed Model for the Evolution of Base Relative Lateral Pressure with Time after Casting at a Rate of  $R=10m/hr$ .

is still clear that the pressure at every point of time during the measurement is lesser for the slower casting rate ( $R = 10m/hr$ ). This is attributed to the thixotropic behavior of the concrete material which behaves more or less like a fluid when cast at a faster rate. At slower rates, however, the already placed material flocculates and builds up a structure strong enough to support portion of the weight of subsequent material cast above it thereby resulting in lower pressure readings than the former case. The model was able to depict similar behavior due to the time dependent spring elements whose stiffnesses

increase with increase in time after casting. These springs are responsible for providing support to the concrete column and, therefore, resulting in lower pressure values with time and/or with slower casting rates.

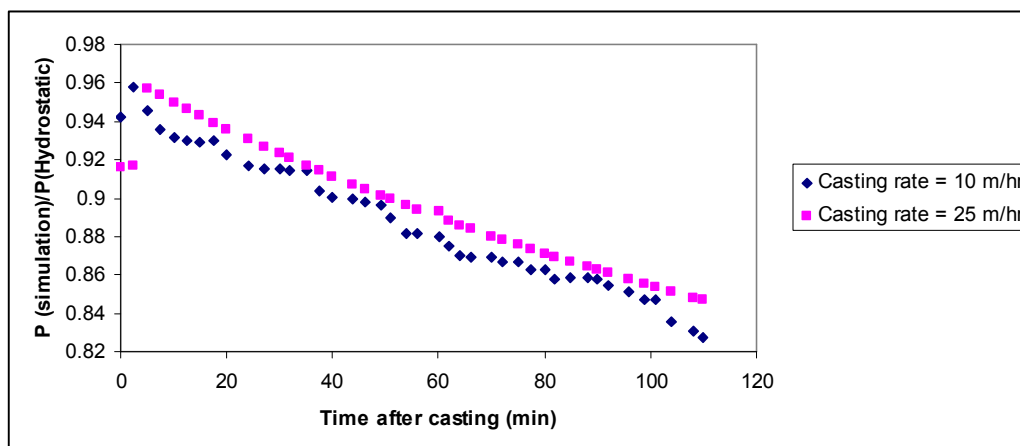


Figure 6.10: The Finite Element Model Showing the Influence of Casting Rate on Lateral Pressure Variations.

Fictitious simulation runs were carried out with two more different values of  $A_{thix}$  (0.5Pa/s and 1.0Pa/s) in addition to the one (0.2Pa/s) used in the above case. Figure 6.11 shows the relative effect of thixotropy on lateral pressure decay. It is evident from the figure that the use of higher thixotropic SCC will result in more reduction in the value of the lateral pressure on formwork.

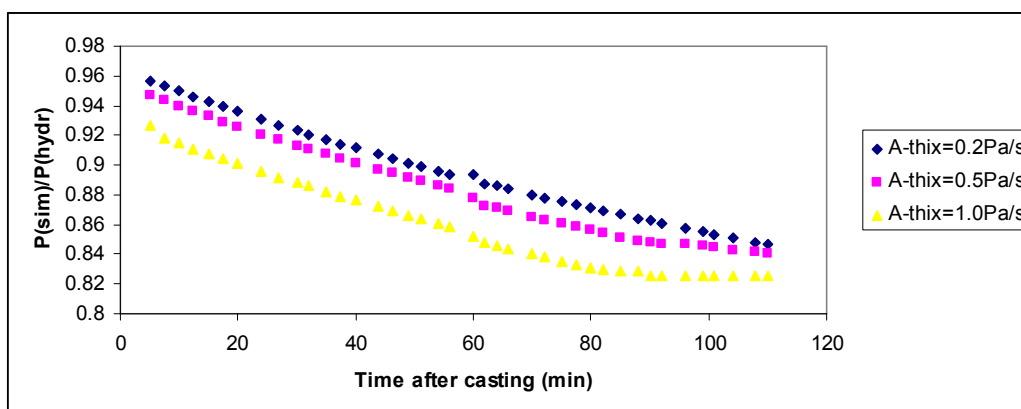


Figure 6.11: Relative Effect of Thixotropy on Lateral Pressure Decay.

In order to verify the model's validity at different heights of a formwork use was made of more data from the work published in (Khayat et al. 2005). The same maximum concrete column modeled above was considered here. Figure 6.12 shows the result obtained from the model's simulation of the relationship between the three variables involved, namely, the lateral pressure, the head of concrete and the time after casting (resting time).

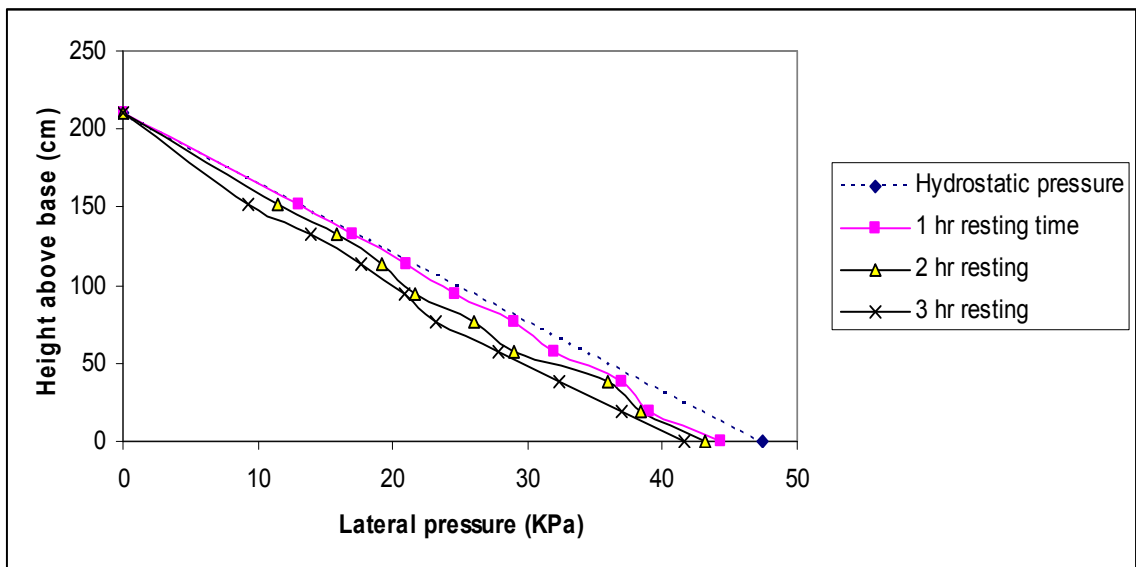
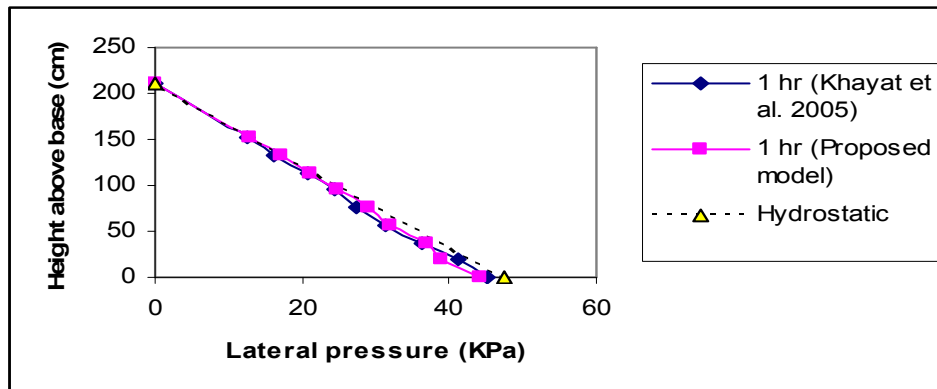


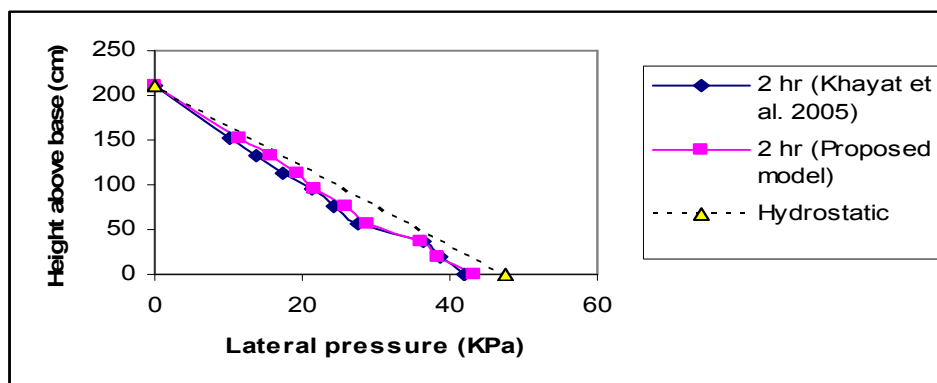
Figure 6.12: Prediction of the Lateral Pressure Variation by the Proposed Finite Element Model at Various Heights above the Base of the 2.1m High Concrete Tested by Khayat et al. (2005).

Figure 6.13 shows the comparison with the results achieved by (Khayat et al. 2005). From these figures (a, b and c) it is obvious how the simulation/experimental curves move further away from the hydrostatic pressure envelope.

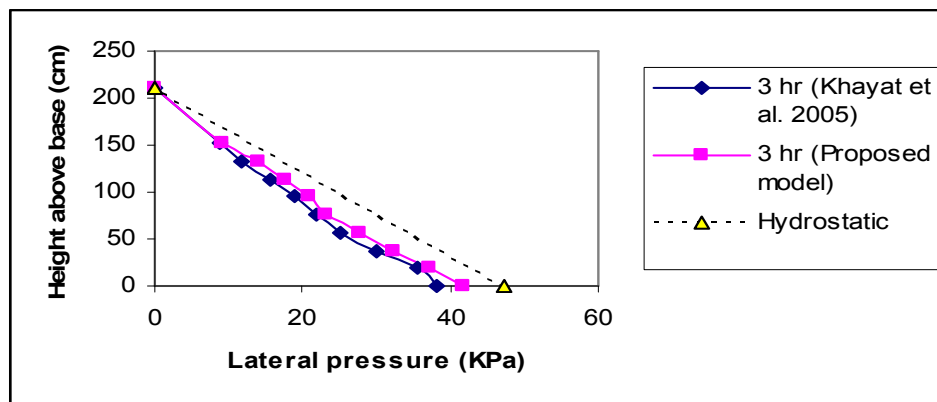




(a)



(b)



(c)

Figure 6.13: Comparison between Literature Experimental Results [Khayat et al., 2005] and Predictions of the Proposed Model of the Lateral Pressure Variations ((a) 1 hour (b) 2 hours (c) 3 hours) at Various Heights above the Base of a 2.1m High Column.

### 6.3.2 Pumping Versus Casting

It has been shown in the previous validations that the model presented in this research can predict the variation of lateral pressure in a vertical formwork at various heights with respect to time after casting. However, it will be reiterated here that the model may not be suitable for predicting such behavior in the case of pumped/injected concrete. In order to illustrate how the model behaves relative to the two different phenomena (casting and pumping/injection), the experimental work carried out by Vanhove et al. (2004) is simulated here and the results compared with the model developed by the same authors. The estimation by their model uses the Janssen's model as used in the statics of ensiled granular material. Briefly, their experimental work includes setting up two forms 12 m high. Injection of SCC was carried in the first formwork and poured from the top opening in the case of the second one. Using their proposed equation, with the aid of tribometry measurements, they estimated the lateral pressure of the concrete against the formwork in each of the two cases. Prediction of their model in the case of casting and injection/pumping compared to their experimental readings for the poured concrete is illustrated in Figure 6.14. Also, the prediction by finite element model developed in this work is superimposed. The three curves show clearly that the model developed in this research is more suitable for adoption when simulating the pressure variation in the case of poured rather than injected concrete. The latter can be seen, from the graph, to approach the hydrostatic pressure head, because during pumping the concrete stays predominantly as fluid.

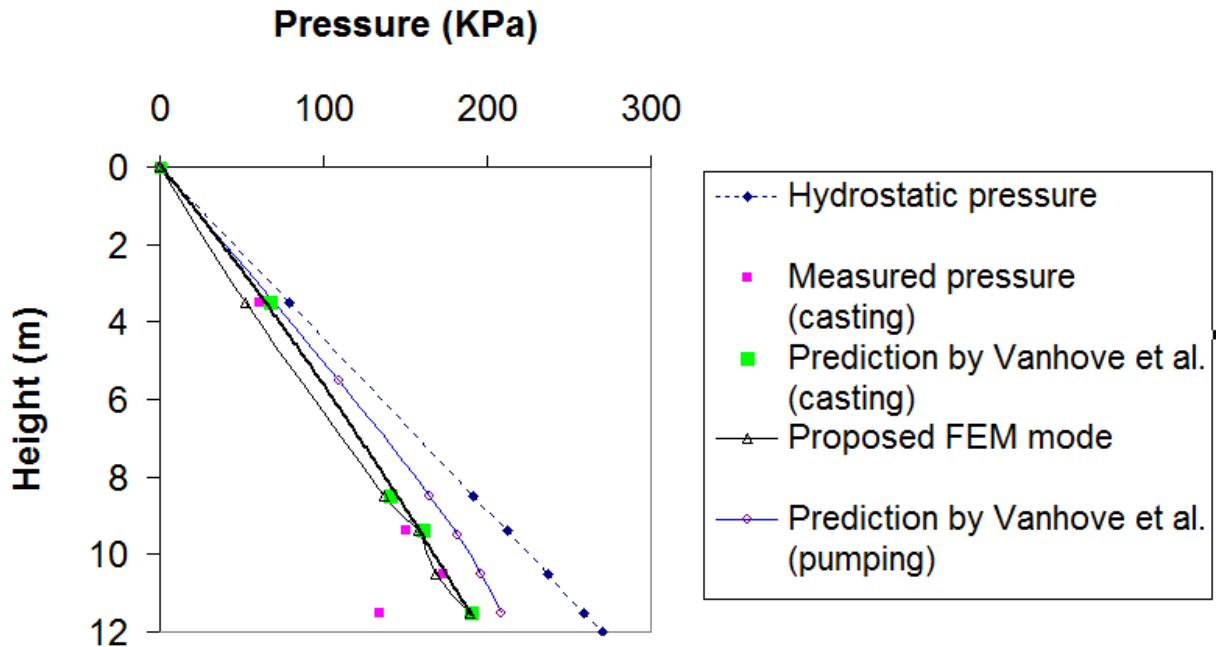


Figure 6.14: Comparison between Literature Experimental Results [Vanhove et al., 2004] and Predictions of the Proposed Model for the Evolution of Relative Lateral Pressure with Time after Casting at a Rate of  $R=10.3m/hr$  and  $A_{thix}=0.4Pa/s$ .

### 6.3.3 Effect of Casting Rate on Maximum Lateral Pressure

Ovarlez and Roussel (2006) noticed and reported the contradiction in the statements found in literature that the maximum lateral pressure is slightly affected by casting rate (Khayat et al. 2005) and the casting rate plays a major role (Billberg 2003). However, with the aid of their analytical model, Ovarlez and Roussel (2006) were able to explain this phenomenon beyond doubt. The finite element model developed here has also successfully captures this observation. Figure 6.15 shows the existence of two regimes as reported by Ovarlez and Roussel (2006); the casting rate plays a significant role on the variation of the relative lateral stress within the first regime, whereas the second regime shows negligible effect of this parameter.

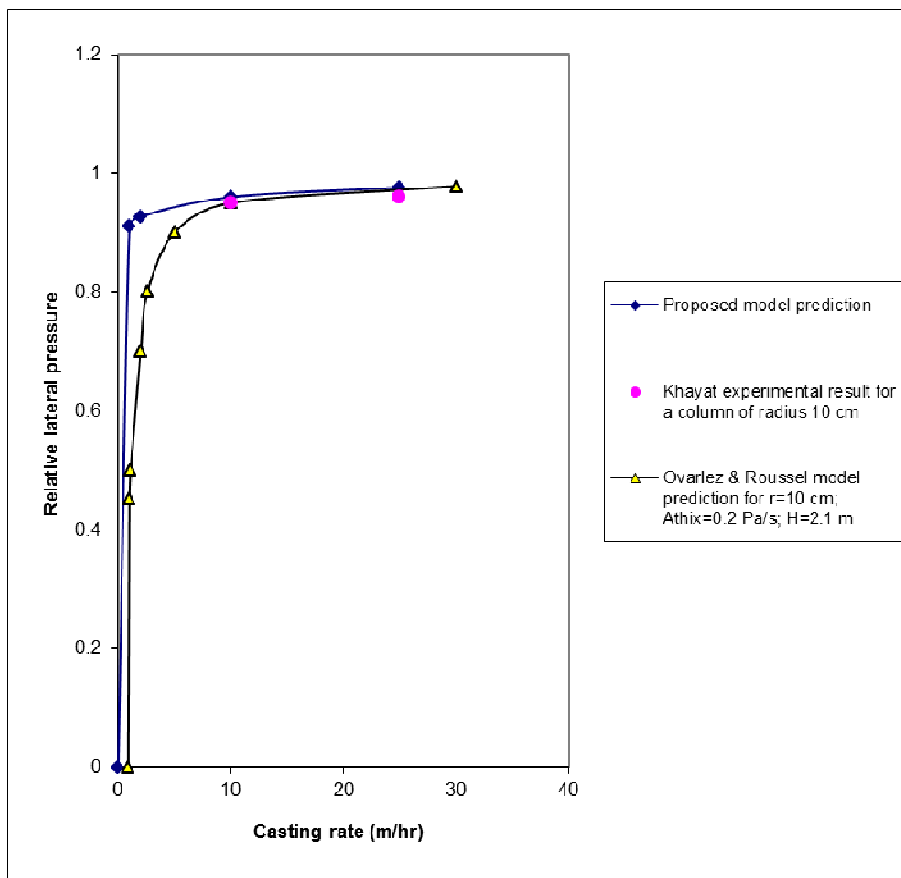


Figure 6.15: Comparison between Prediction by the Model Proposed, Experimental Result by Khayat et al. (2005), and the Model Proposed by Ovarlez and Roussel (2006) for the Effect of Casting Rate on Relative Lateral Pressure at the Base of a 2.1m High Column.

## CHAPTER SEVEN

### CONCLUSIONS AND RECOMMENDATIONS

#### 7.1 CONCLUSIONS

Both filling and passing behavior of SCC as well as slab and wall castings were numerically simulated using the commercial software FLUENT in order to substantiate the validation of the hydrodynamic modeling of the flow behavior of this material. Using the volume of fluid (VOF) approach and Herschel-Bulkley viscosity model (both thixotropic and non-thixotropic), an excellent agreement between the experiment and the simulation results was obtained. In addition, a new finite element model for the prediction of lateral stress evolution due to self compacting concrete was developed and presented in this research. Its validation relies, mainly, on the use of available experimental results from the literature. Predictions achieved by this model were found to be successful.

Based on this study, the following conclusions are made.

- 1) CFD simulation for flow of fresh SCC yields results that match experimentally observed values of flow characteristics in the slump, L-box, and the V-funnel tests. The CFD model, using the dynamic yield stress  $\tau_0$  and plastic viscosity  $\mu_p$  as input parameters, predicts various flow characteristics for different SCC mixes, including those admixed with silica fume, fly ash and limestone powder.
- 2) The thixotropy model can be included as user-defined function into FLUENT and is noted to change the flow attributes of the SCC in contrast to the non-thixotropic model, and as confirmed by experimental observations.

- 3) Immediate casting with SCC's using retarding agents in the mix will lead to development of high formwork pressure for vertical walls due to significant reduction in  $A_{thix}$  in the presence of retarding agents.
- 4) The proposed finite element model presented in this research is able to describe quantitatively the evolution of the lateral stress on the formwork in terms of the thixotropic evolution of the yield stress at rest and its influence on the boundary conditions.
- 5) For a very high casting rate,  $R$  the maximum lateral pressure in a formwork approaches the hydrostatic value because the material is not able to flocculate and thus keeps on behaving as a fluid. On the other hand, the lateral pressure remains below the hydrostatic pressure when the material is cast from the top of the formwork at a rate slow enough to allow flocculation.
- 6) Highly thixotropic SCC material displays a smaller maximum lateral pressure value even if cast at a high rate unlike the less thixotropic one.
- 7) The lateral pressure decreases quickly after the end of the casting as the concrete is now at rest and so able to develop a higher yield stress and starts behaving as a solid.
- 8) The simple model can be used by mix designers for selection of appropriate SCC to yield the required  $A_{thix}$  for minimization of formwork pressure in casting of deep members such as retaining walls and shear walls.
- 9) The virtual simulation for flow of SCC presented in this research could be used as a useful tool for ensuring a robust SCC mix for construction and, hence, with its successful validation, this work stands to make a considerable contribution towards optimizing SCC and increasing its uptake in the Kingdom of Saudi Arabia.

## 7.2 RECOMMENDATIONS FOR FUTURE RESEARCH

The following recommendations can be made for further research in this area

- 1) In this research, a single fluid modeling approach was used to simulate the flow behavior of SCC during testing and casting processes. Although this was proved to be sufficient in studying the flow behavior globally, but future work may incorporate the heterogeneity effects and, hence, provides the means to study other micro or local behavior such as the possibility of segregation of this material.
- 2) Either a CFD, analytical or finite element model can be devised to study the effect of thixotropy during pumping and the resulting segregation of SCC.
- 3) Since the finite element model for lateral formwork pressure developed in this research is meant to simulate SCC materials that are poured during casting, further study to adjust the model for application in the case of injected concrete is recommended. This way, it will serve as a more versatile tool for the prediction of pressure evolution with more pronounced economic impact due to the reduction in the number of experiments needed to study such phenomenon.
- 4) Due to the considerable reduction in thixotropy of the retarder admixed SCC noticed in this study, and the fact that formwork pressure development is linked to the thixotropic behavior of the material, further research to study the effect of using such retarders on formwork lateral pressure is recommended.

## **APPENDIX: SCC Flow Test Simulation Results**



### Slump Flow and T500 Test:

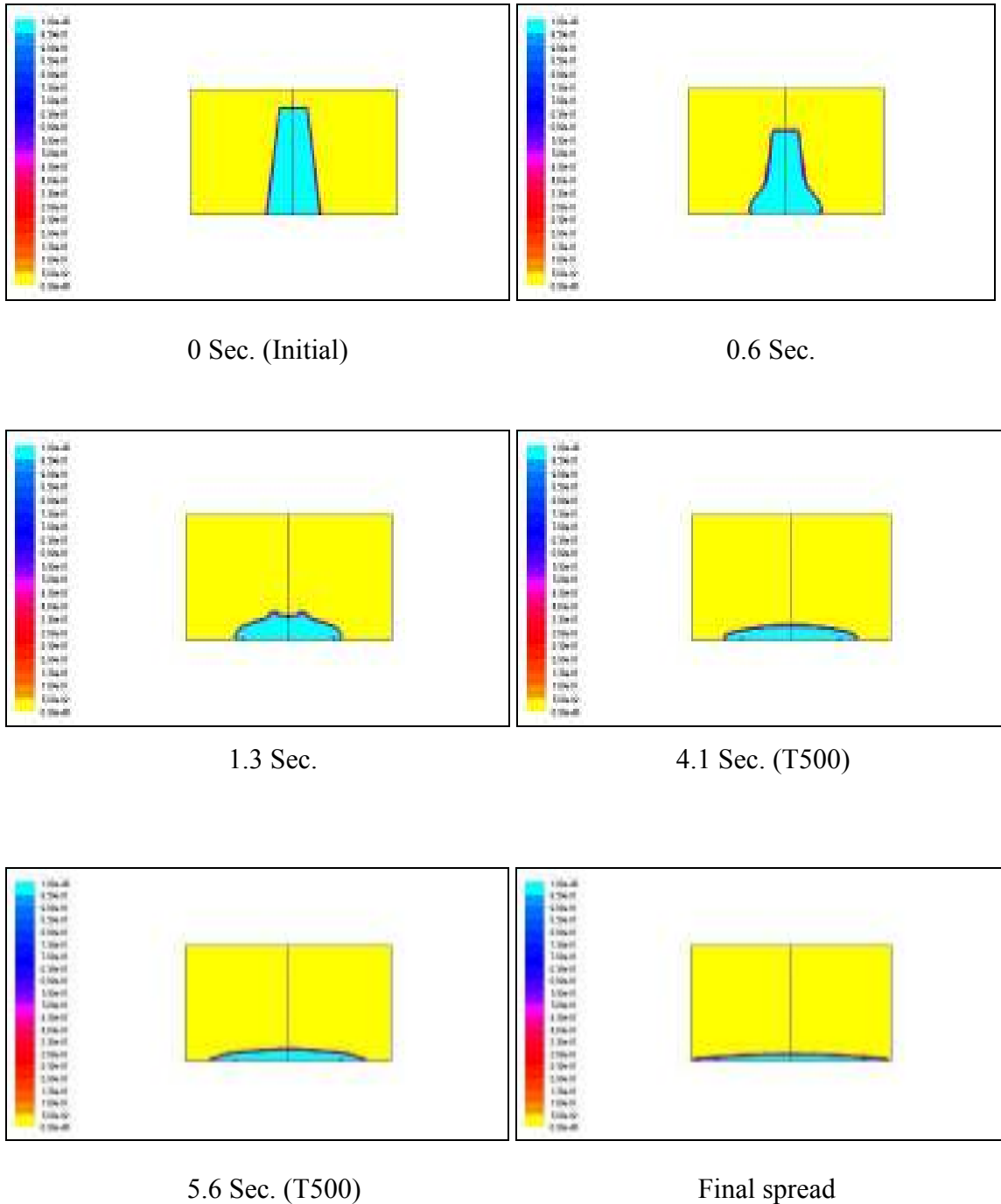


Figure A 1: Progressive Flow of SCC during the Simulation of Slump Test for the Reference Mix.

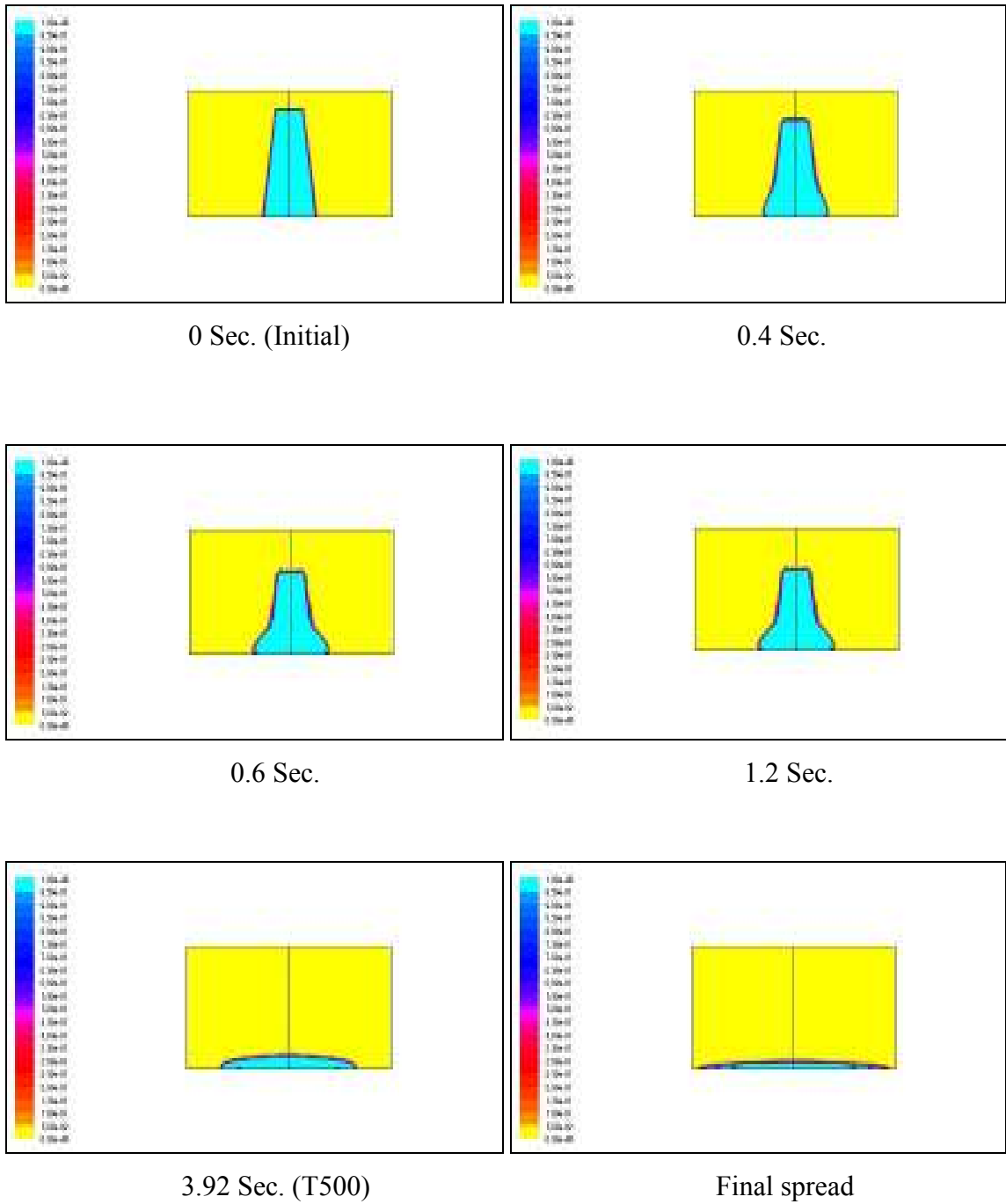


Figure A 2: Progressive Flow of SCC during the Simulation of Slump Test for 5% Fly-Ash.

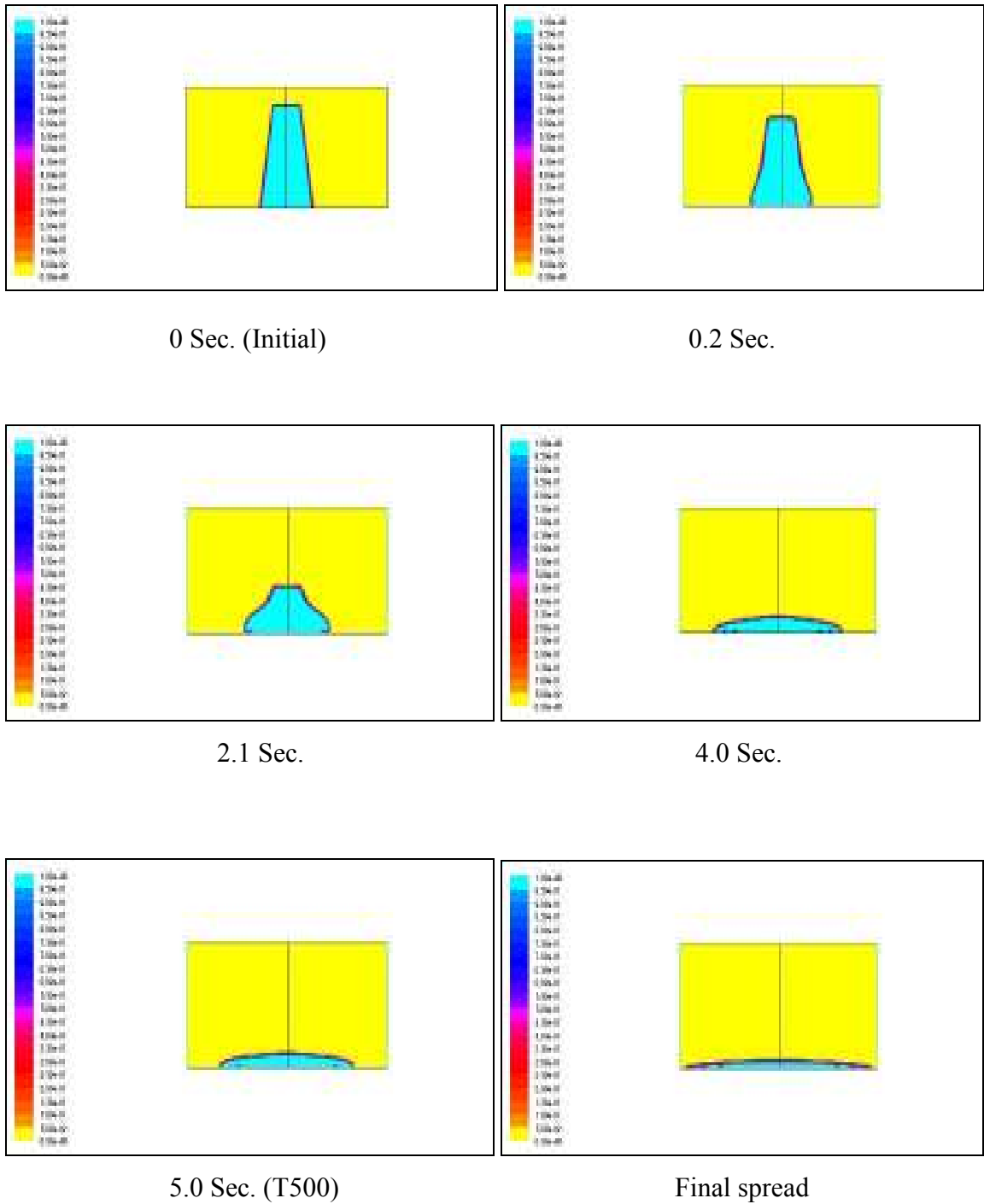


Figure A 3: Progressive Flow of SCC during the Simulation of Slump Test for 7.5% Fly-Ash.

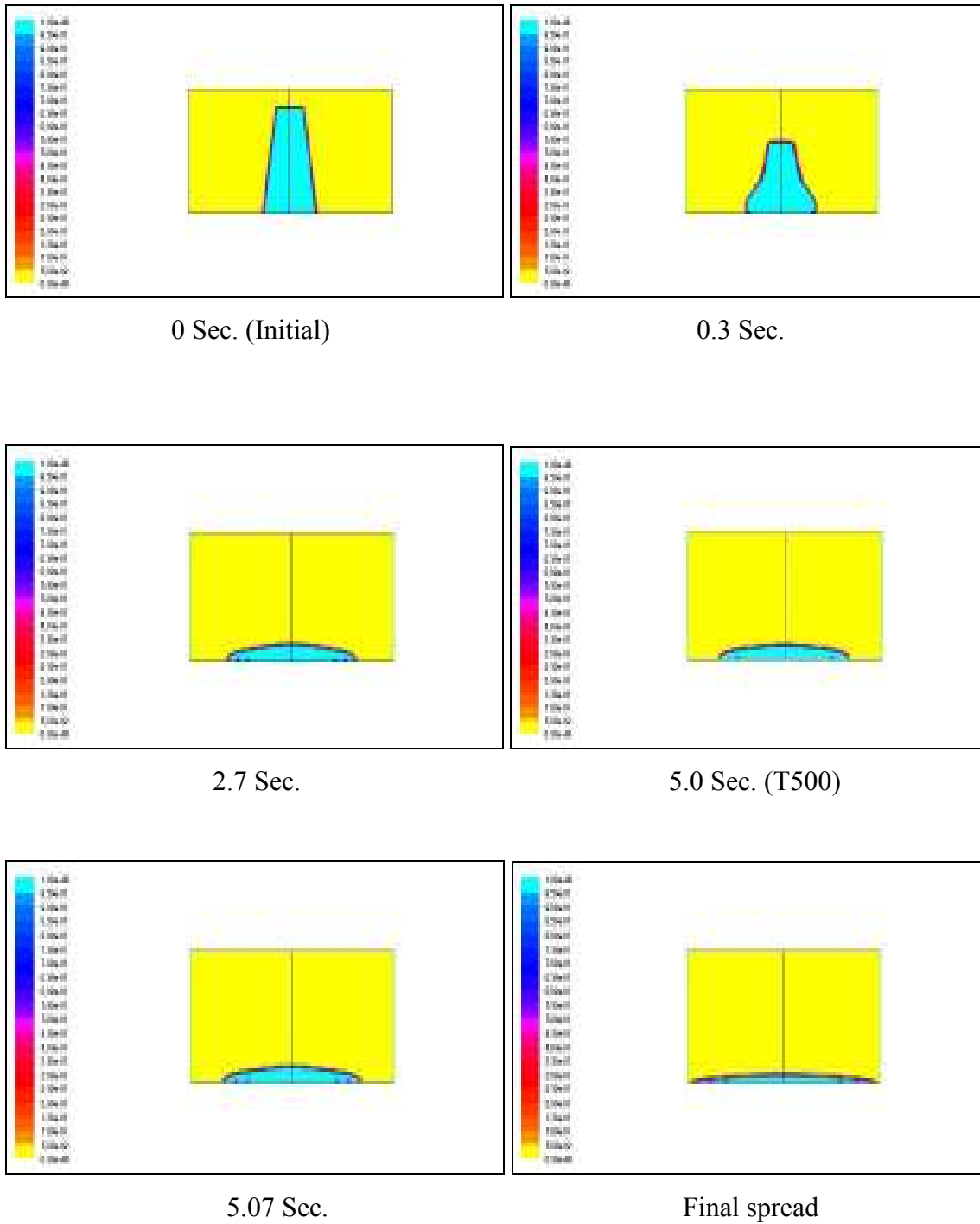


Figure A 4: Progressive Flow of SCC during the Simulation of Slump Test for 10% Fly-Ash.

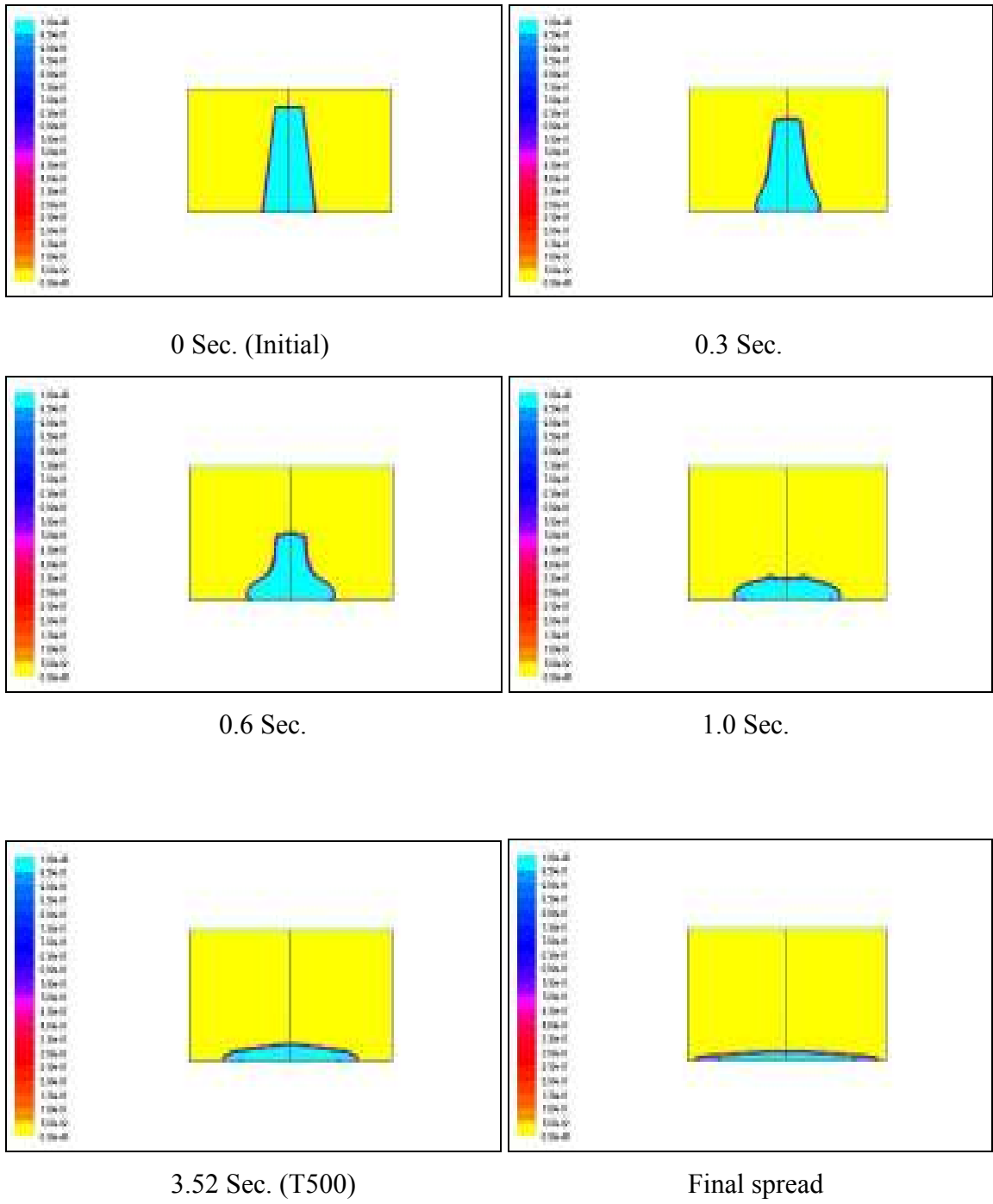


Figure A 5: Progressive Flow of SCC during the Simulation of Slump Test for 5% Lsp.

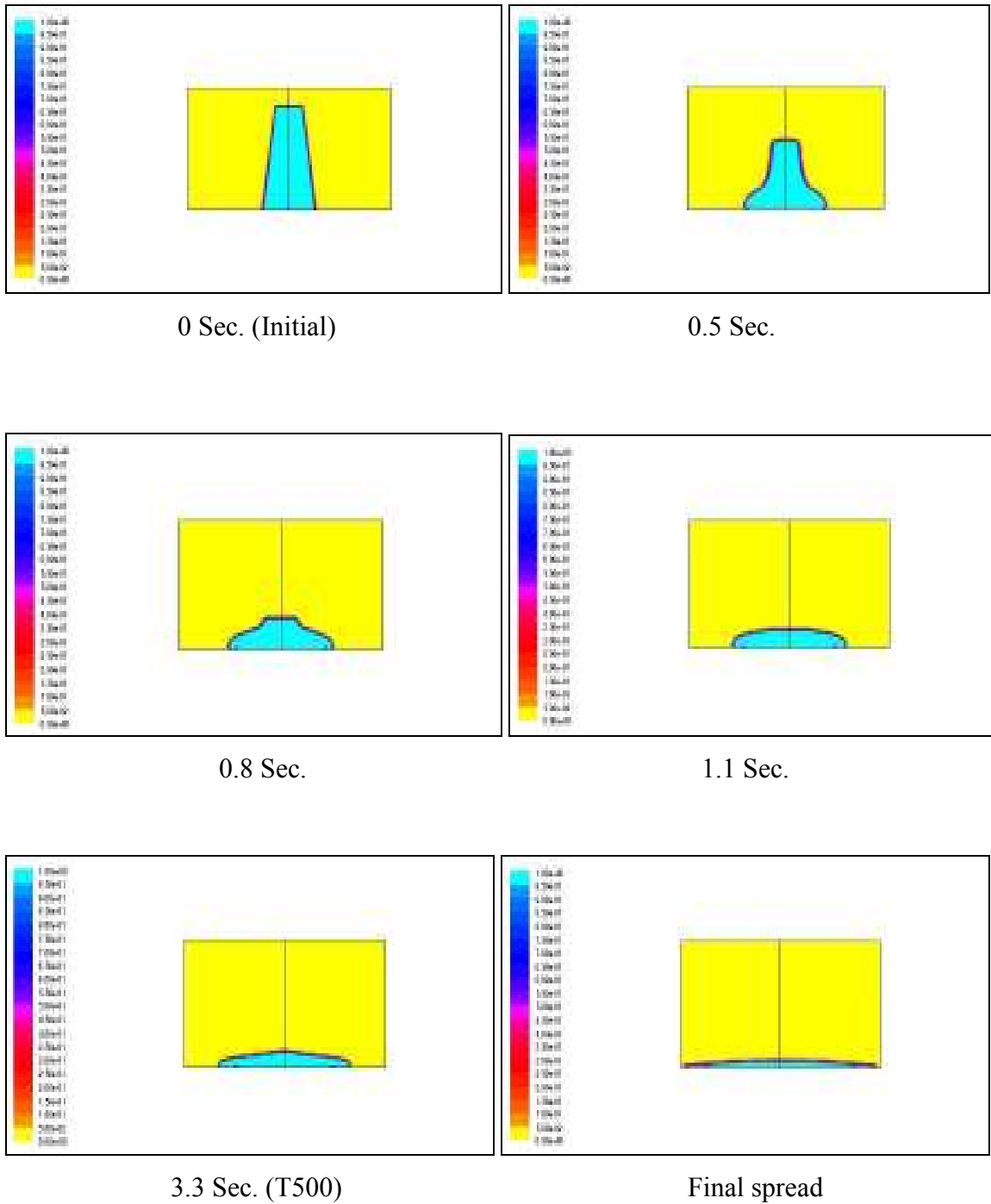


Figure A 6: Progressive Flow of SCC during the Simulation of Slump Test for 10% Lsp.

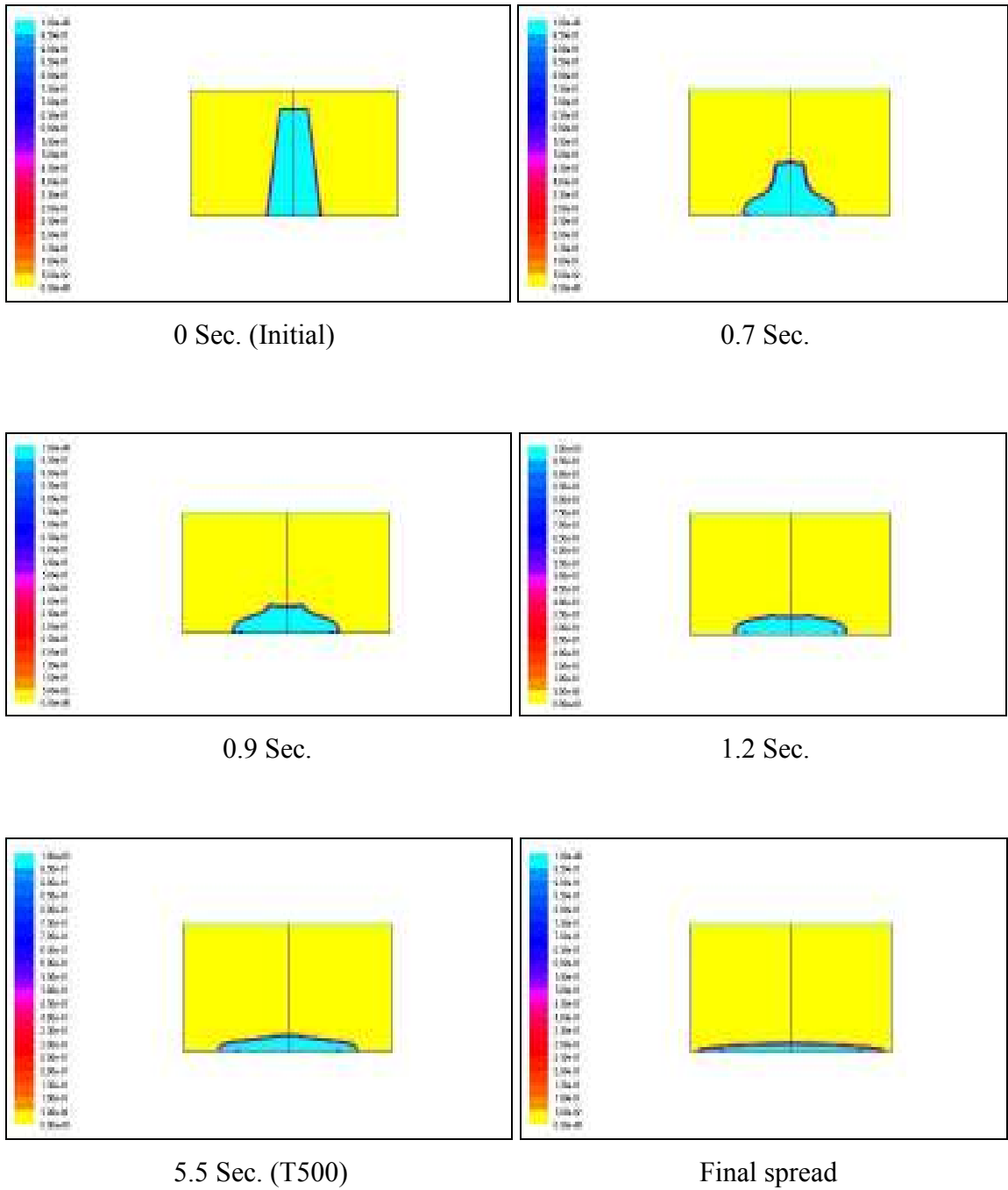


Figure A 7: Progressive Flow of SCC during the Simulation of Slump Test for 15% Lsp.

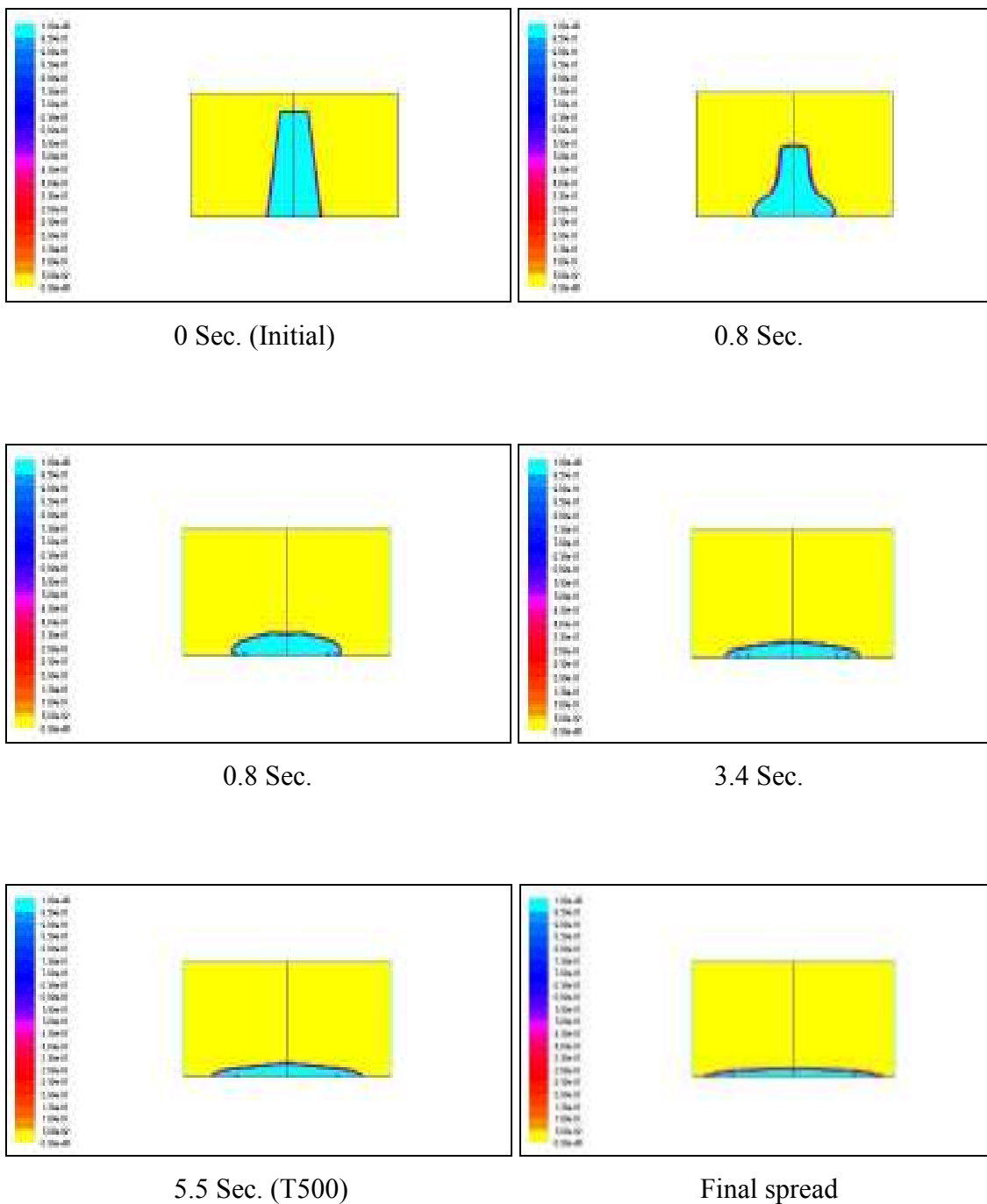


Figure A 8: Progressive Flow of SCC during the Simulation of Slump Test for 2.5% Silica Fume.



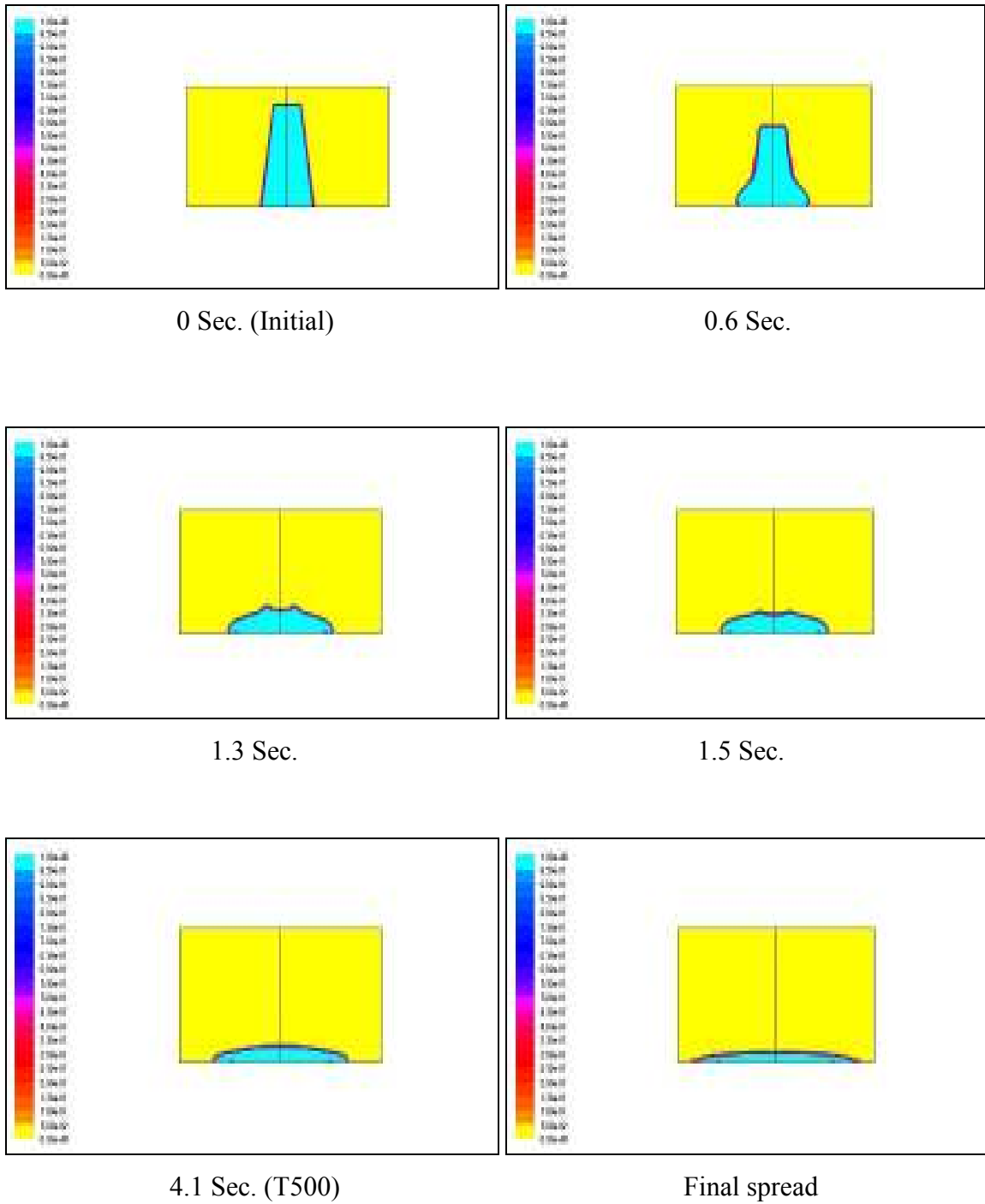
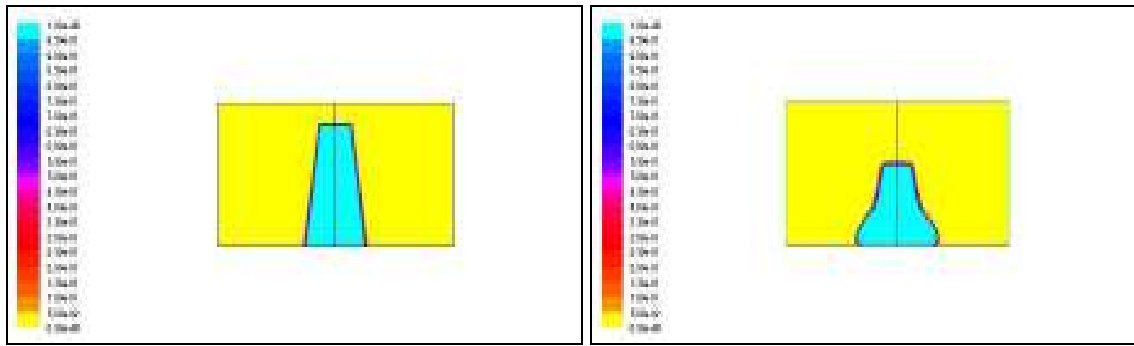
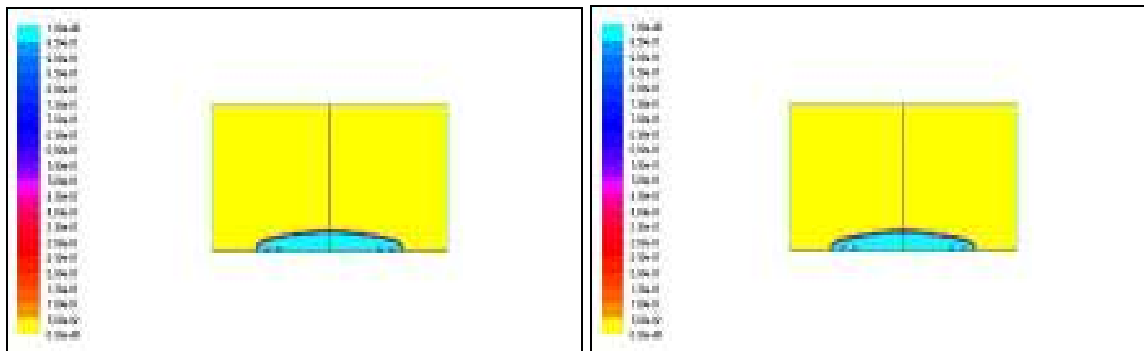


Figure A 9: Progressive Flow of SCC during the Simulation of Slump Test for 5% Silica Fume.



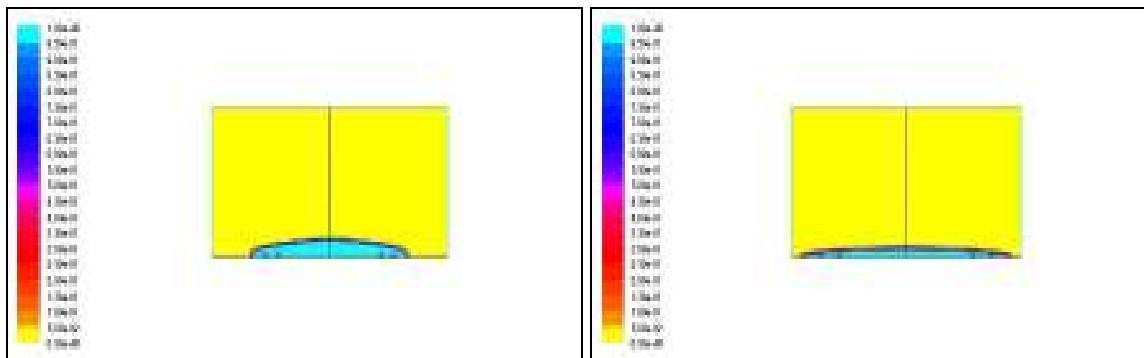
0 Sec. (Initial)

0.3 Sec.



2.4 Sec.

2.9 Sec.



5.1 Sec. (T500)

Final spread

Figure A 10: Progressive Flow of SCC during the Simulation of Slump Test for 7.5% Silica Fume.

**L-box Test:**

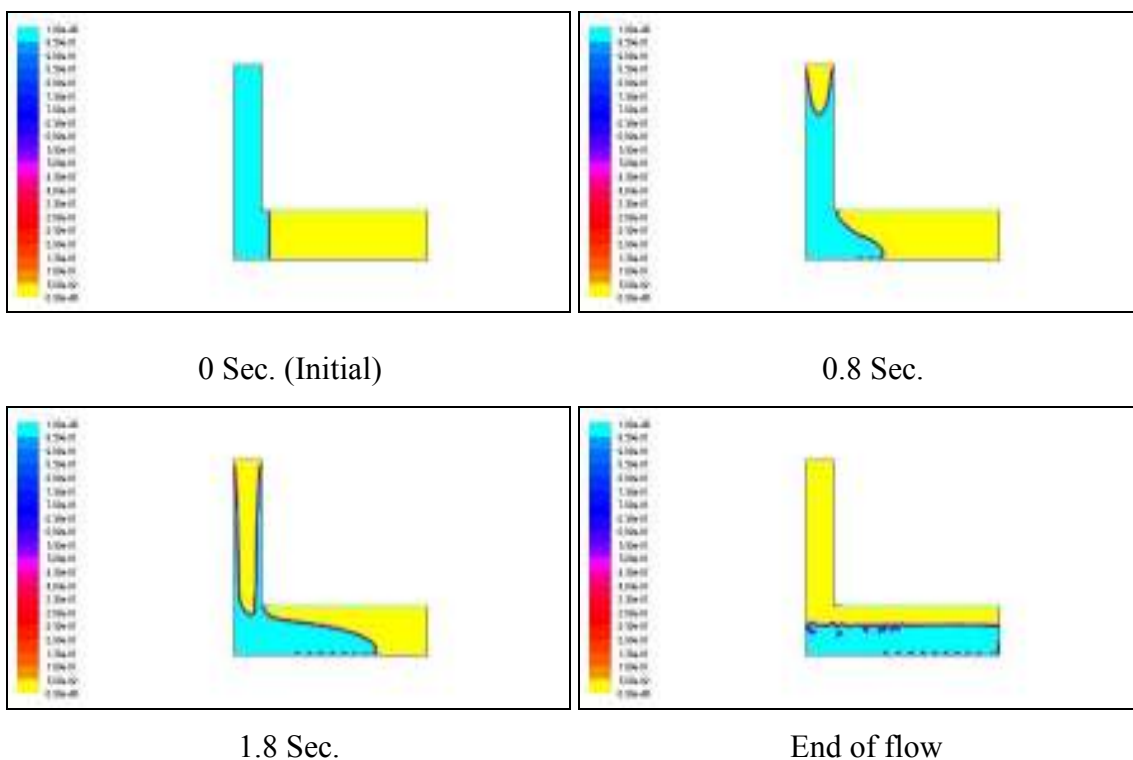


Figure A 11: Progressive Flow during the Simulation of L-box Test for the Reference Mix.

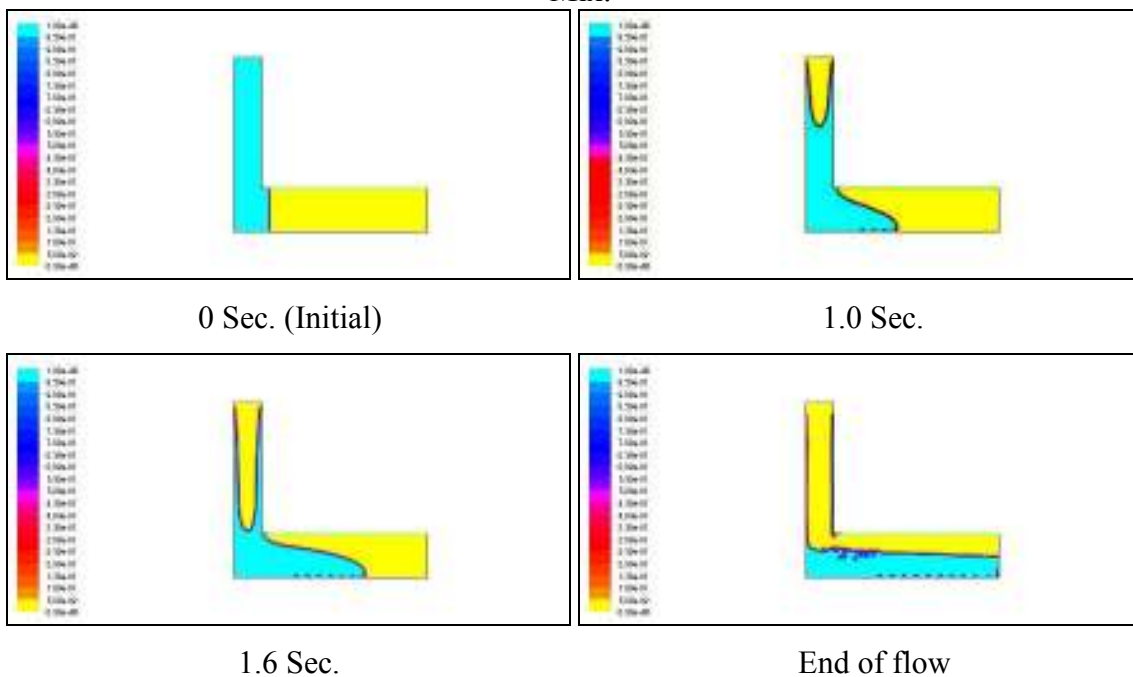


Figure A 12: Progressive Flow during the Simulation of L-box Test for the 5% Fly-Ash.

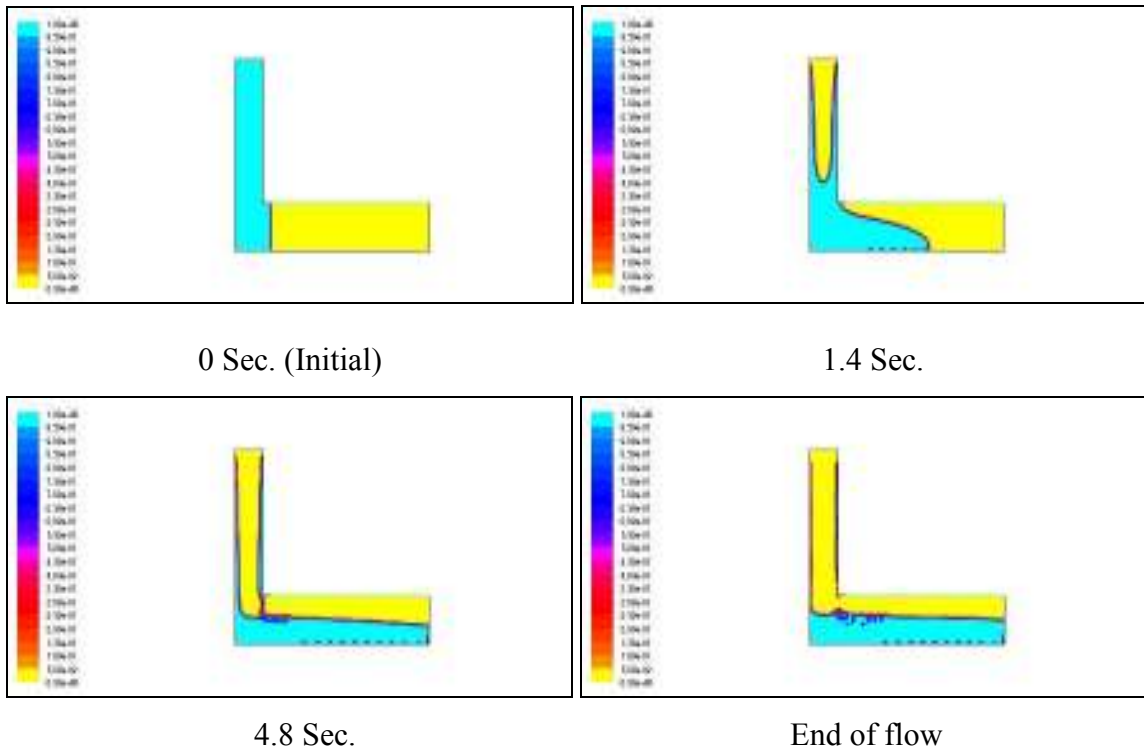


Figure A 13: Progressive Flow during the Simulation of L-box Test for the 7.5% Fly-Ash

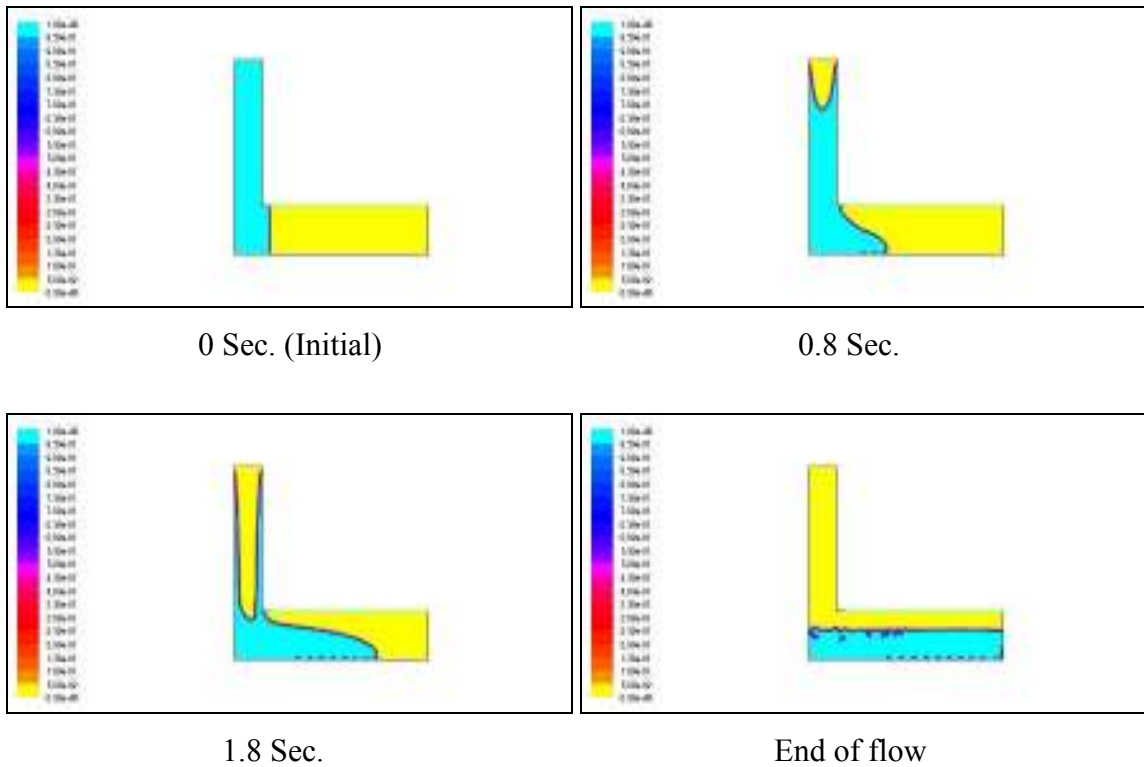


Figure A 14: Progressive Flow during the Simulation of L-box Test for the 10% Fly-Ash.

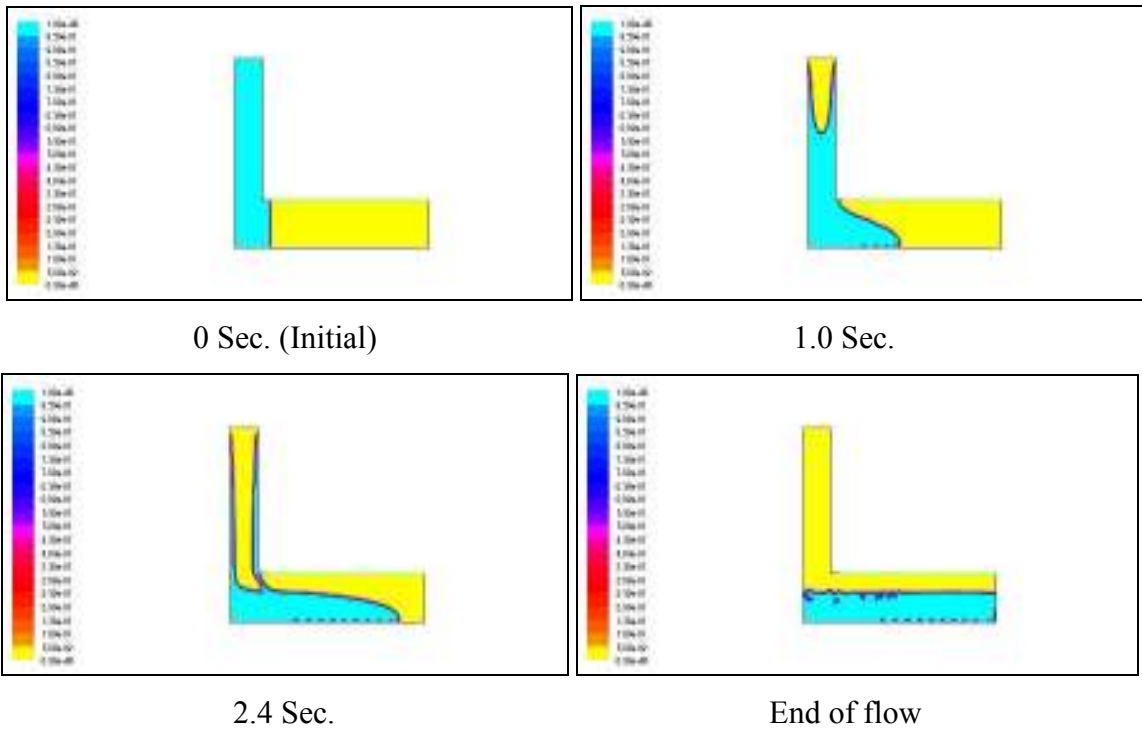


Figure A 15: Progressive Flow during the Simulation of L-box Test for the 5% Lsp.

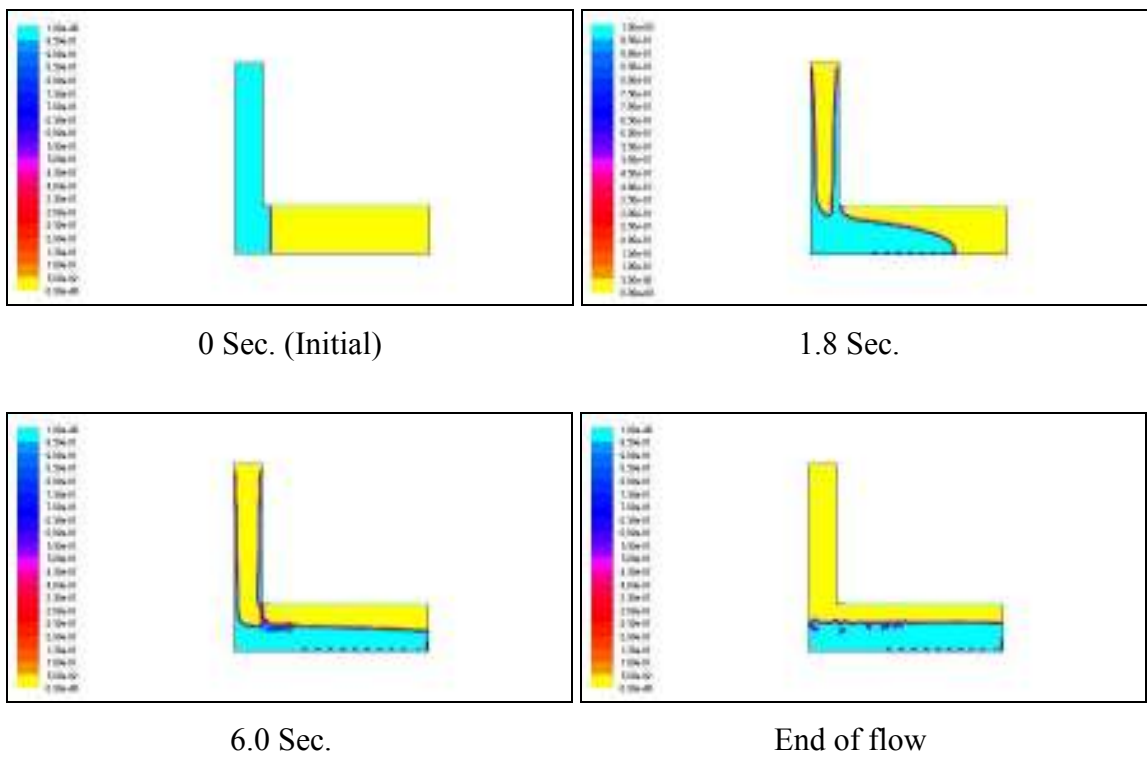


Figure A 16: Progressive Flow during the Simulation of L-box Test for the 10% Lsp.

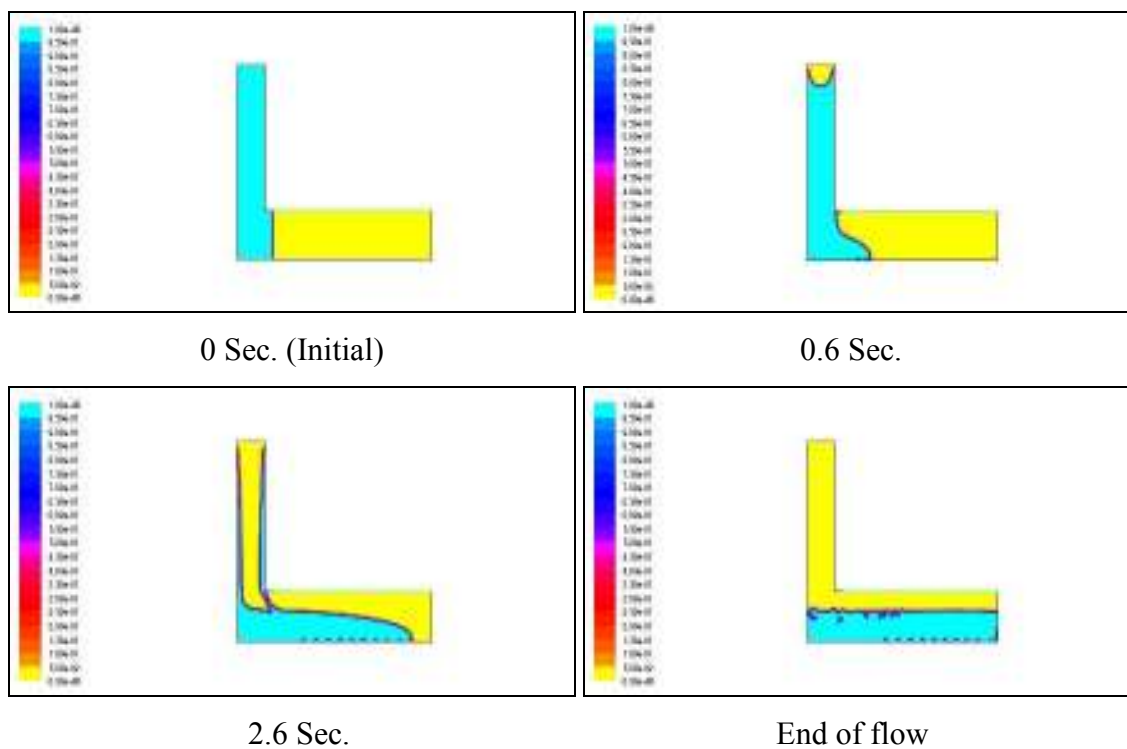


Figure A 17: Progressive Flow during the Simulation of L-box Test for the 15% Lsp.

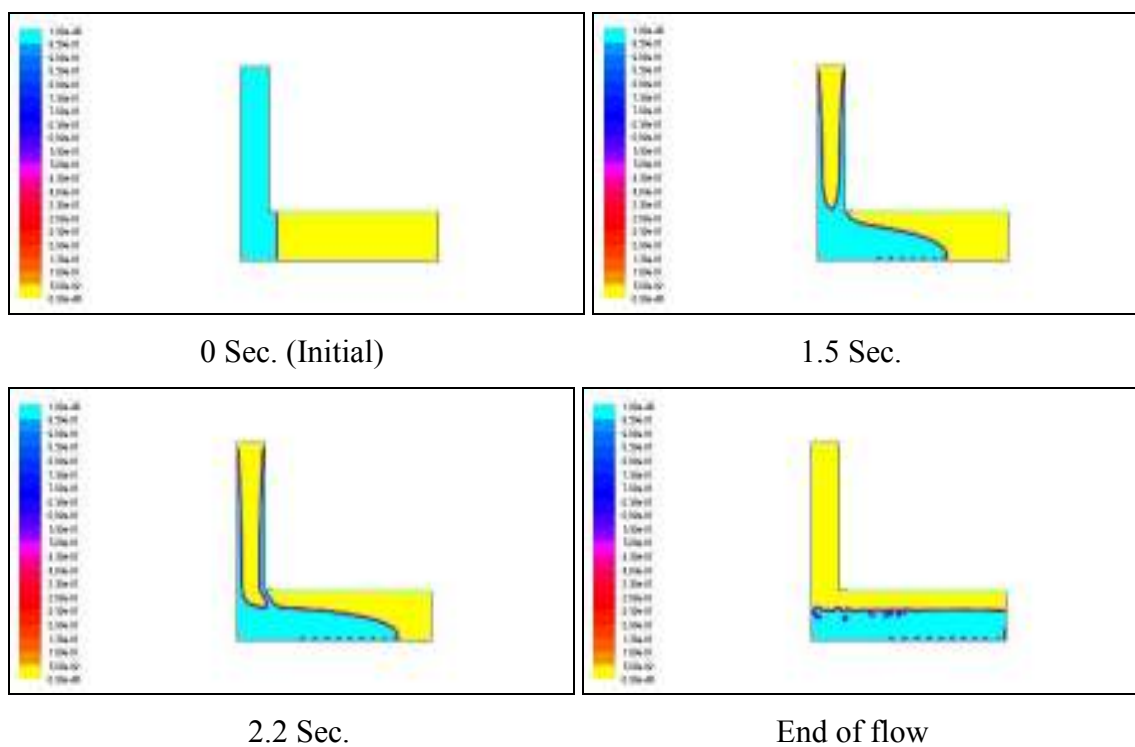


Figure A 18: Progressive Flow during the Simulation of L-box Test for the 2.5% Silica Fume.

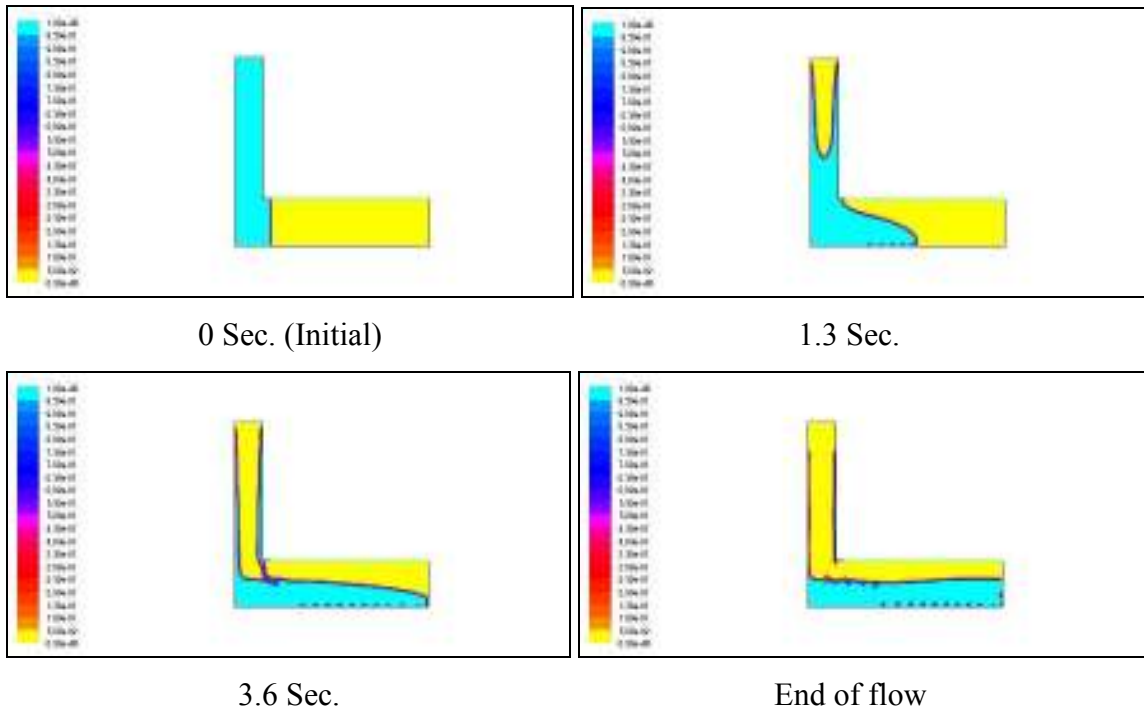


Figure A 19: Progressive Flow during the Simulation of L-box Test for the 5% Silica Fume.

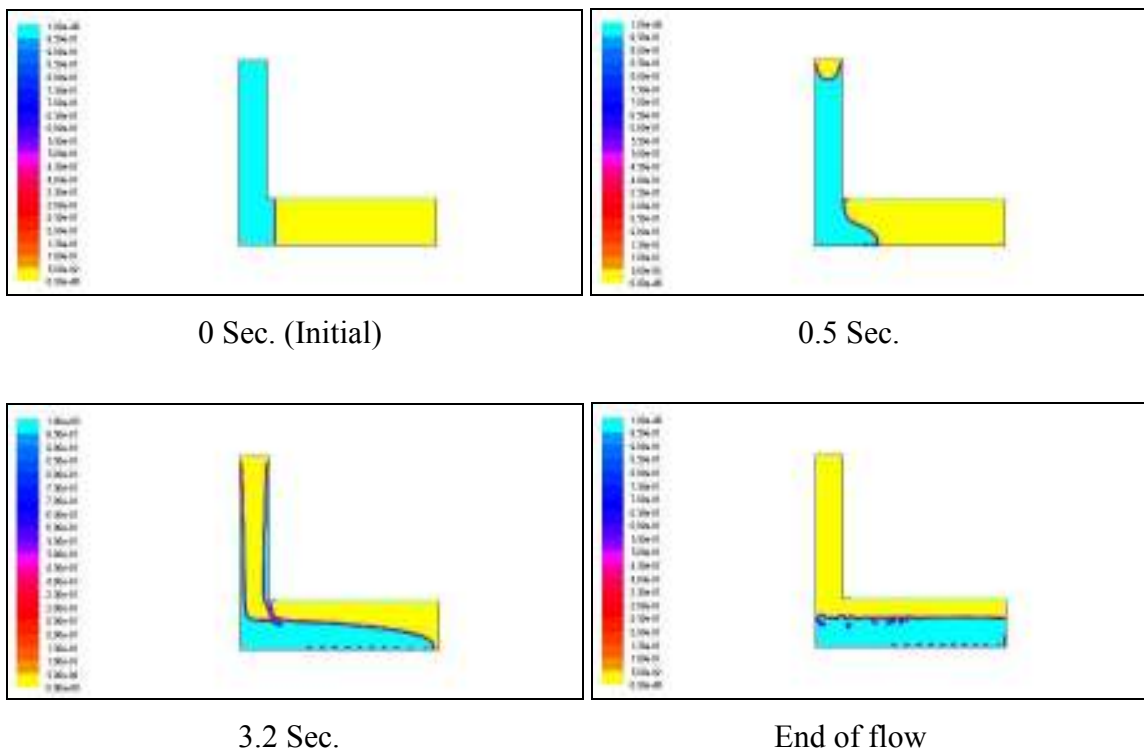


Figure A 20: Progressive Flow during the Simulation of L-box Test for the 7.5% Silica Fume.

**V-funnel Test:**

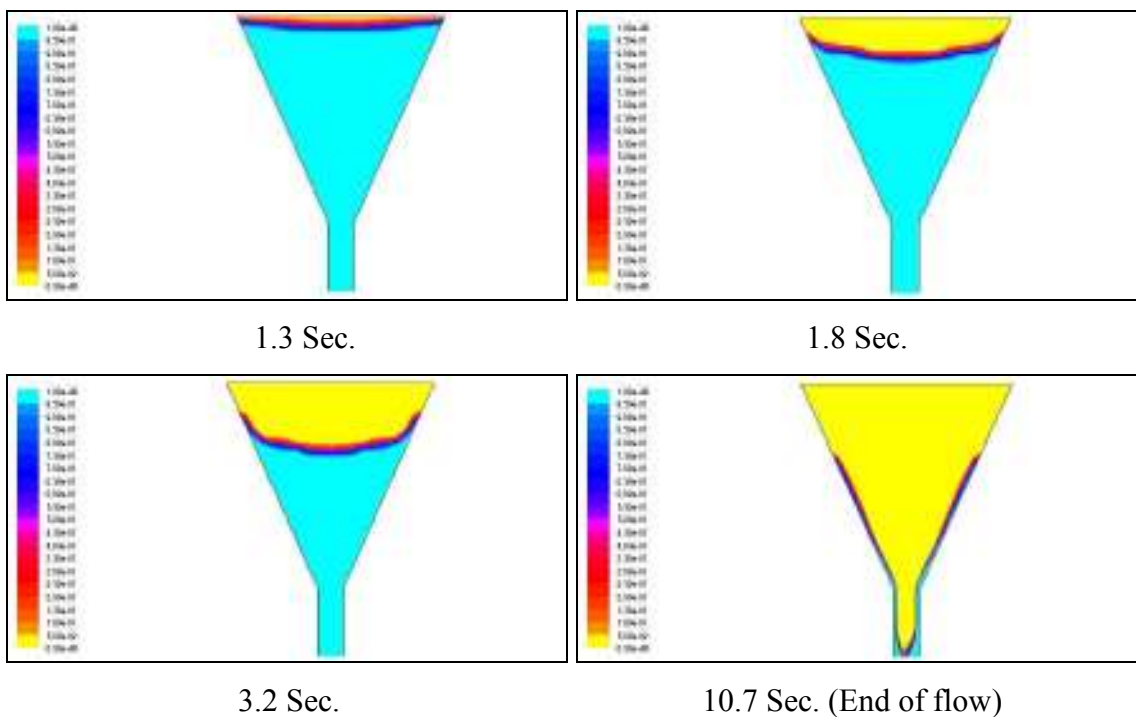


Figure A 21: Progressive Flow during the Simulation of V-funnel Test for the Reference Mix.

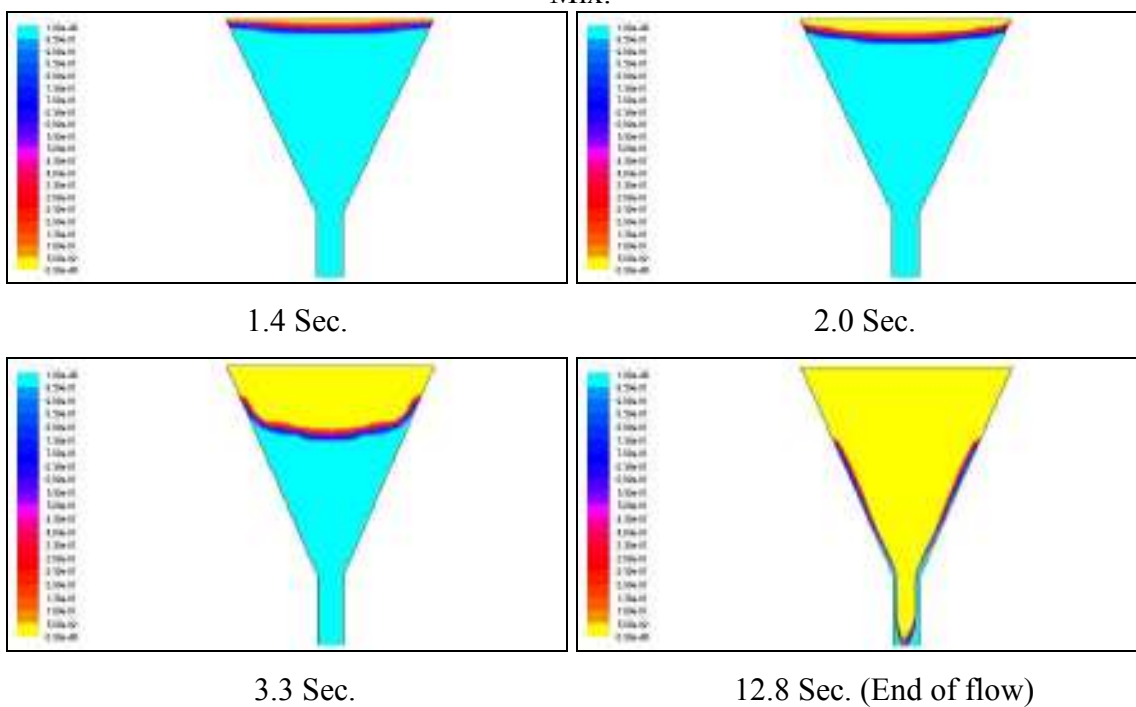


Figure A 22: Progressive Flow during the Simulation of V-funnel Test for the 5% Fly-Ash.



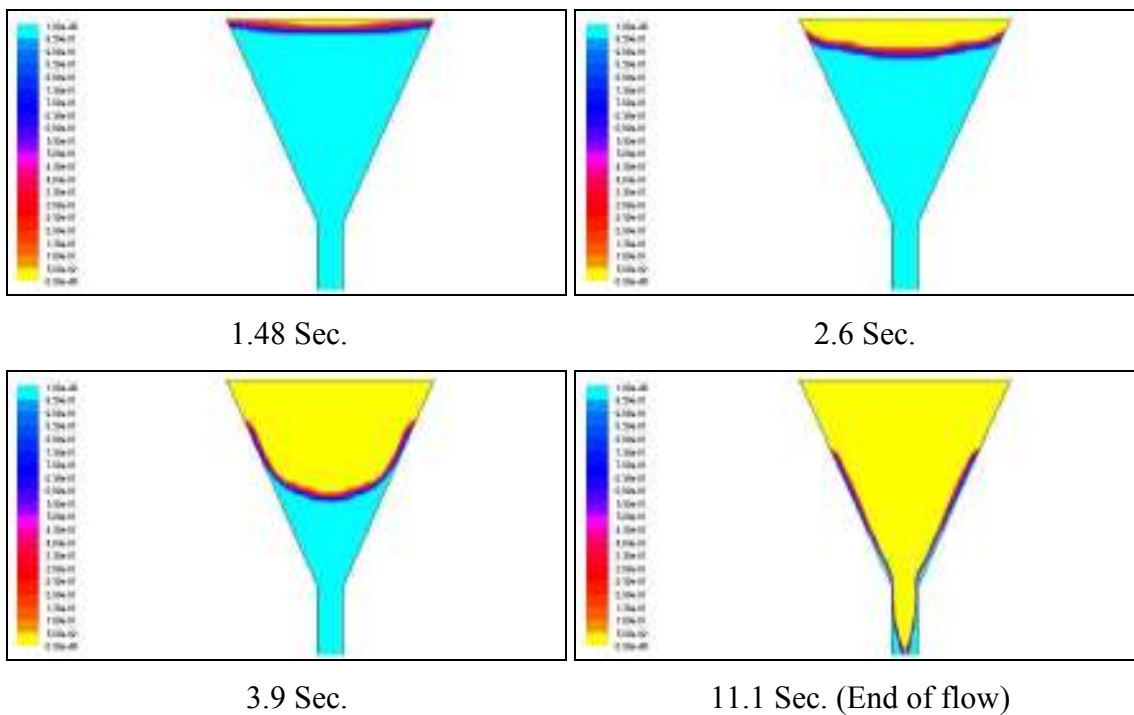


Figure A 23: Progressive Flow during the Simulation of V-funnel Test for the 7.5% Fly-Ash.

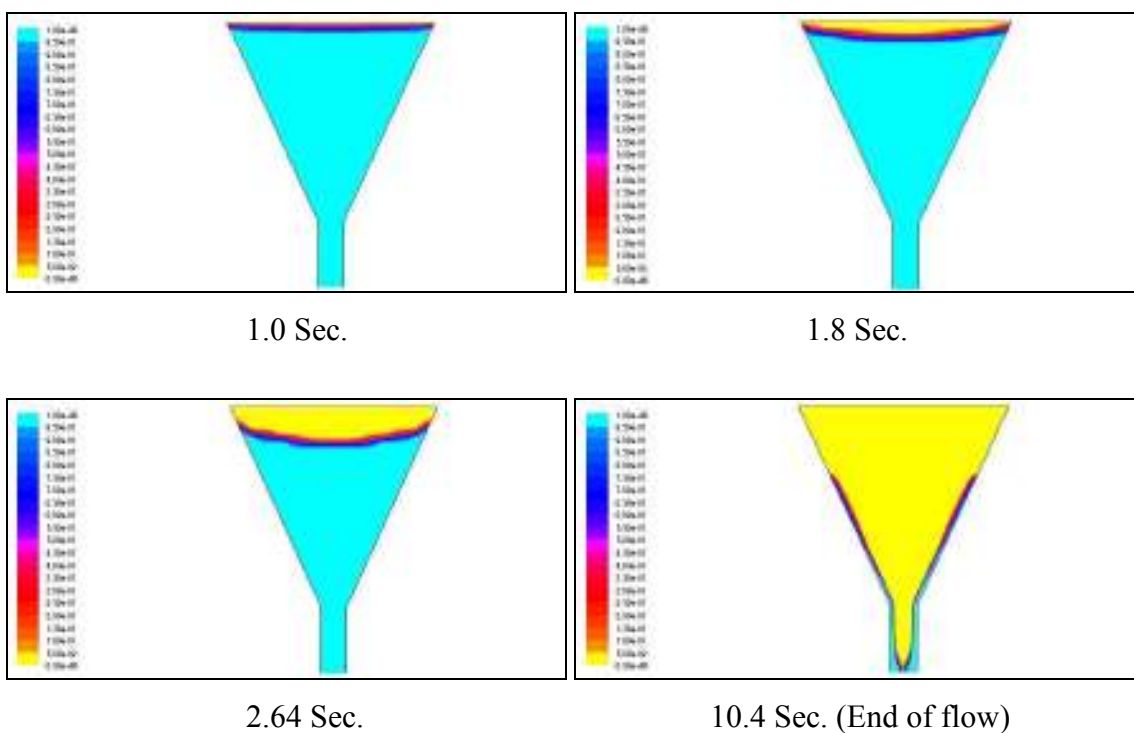


Figure A 24: Progressive Flow during the Simulation of V-funnel Test for the 10% Fly-Ash.

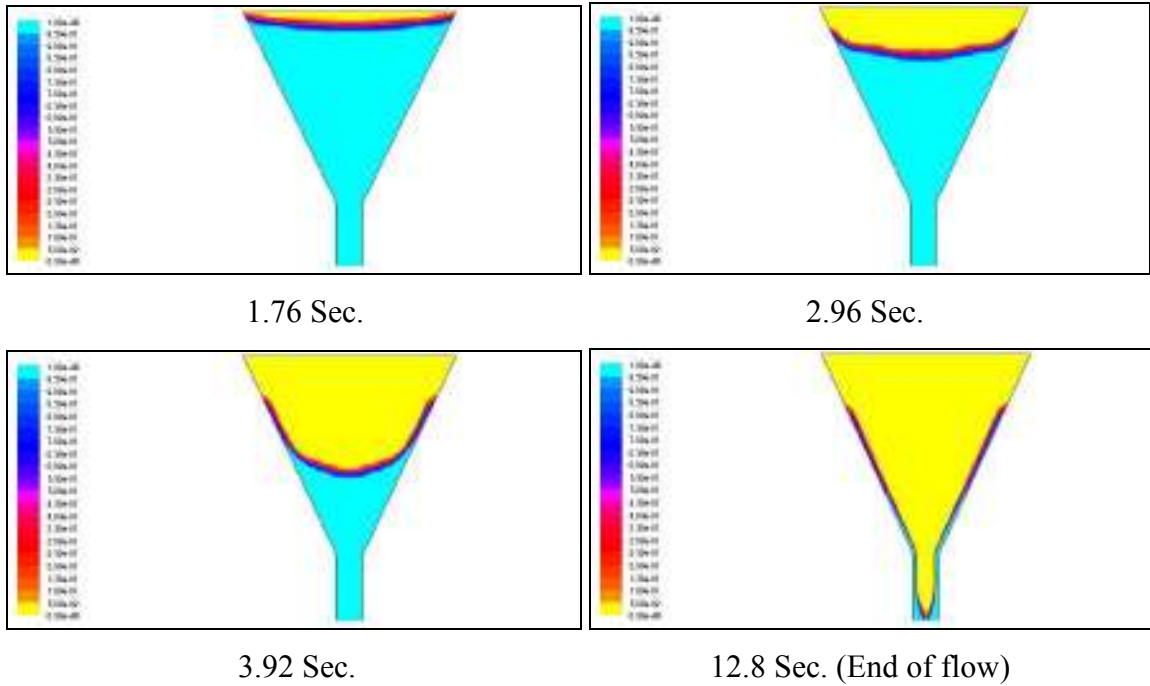


Figure A 25: Progressive Flow during the Simulation of V-funnel Test for the 5% Lsp.

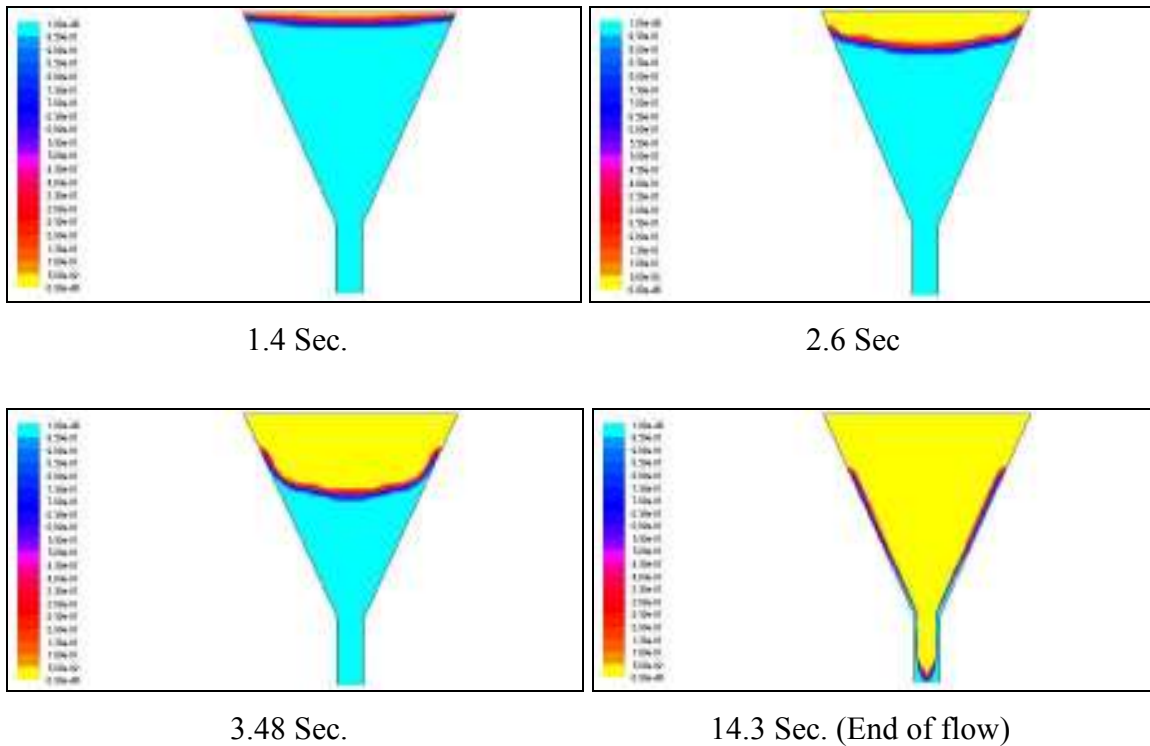


Figure A 26: Progressive Flow during the Simulation of V-funnel Test for the 10% Lsp.

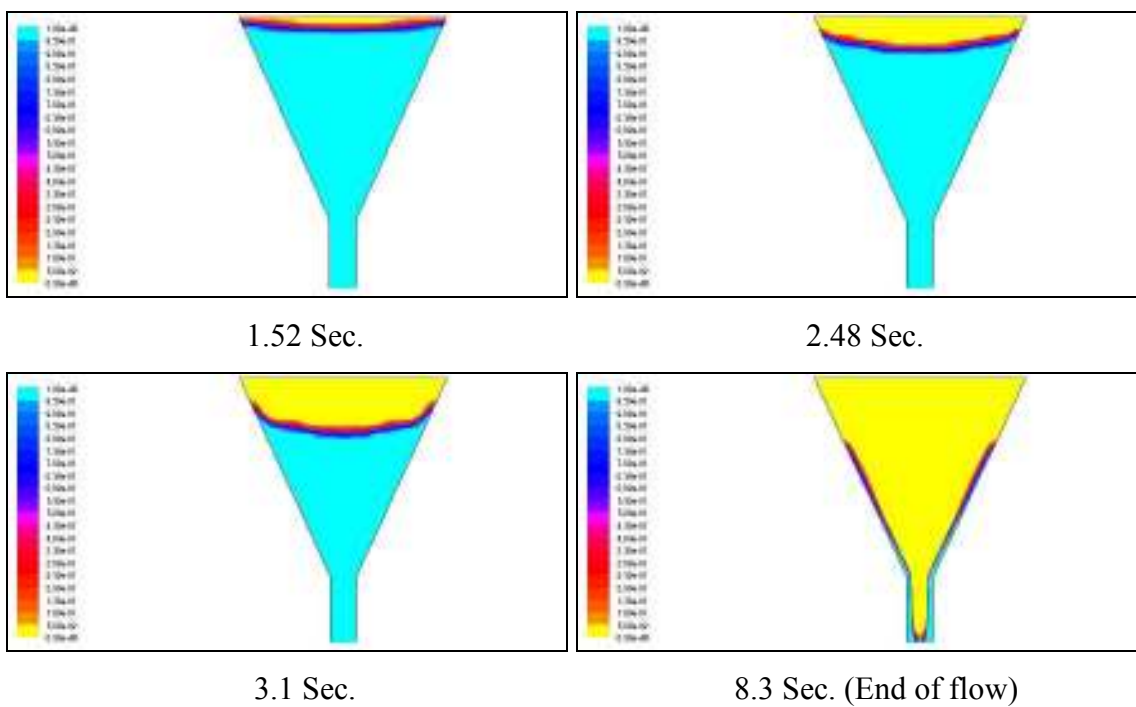


Figure A 27: Progressive Flow during the Simulation of V-funnel Test for the 15% Lsp.

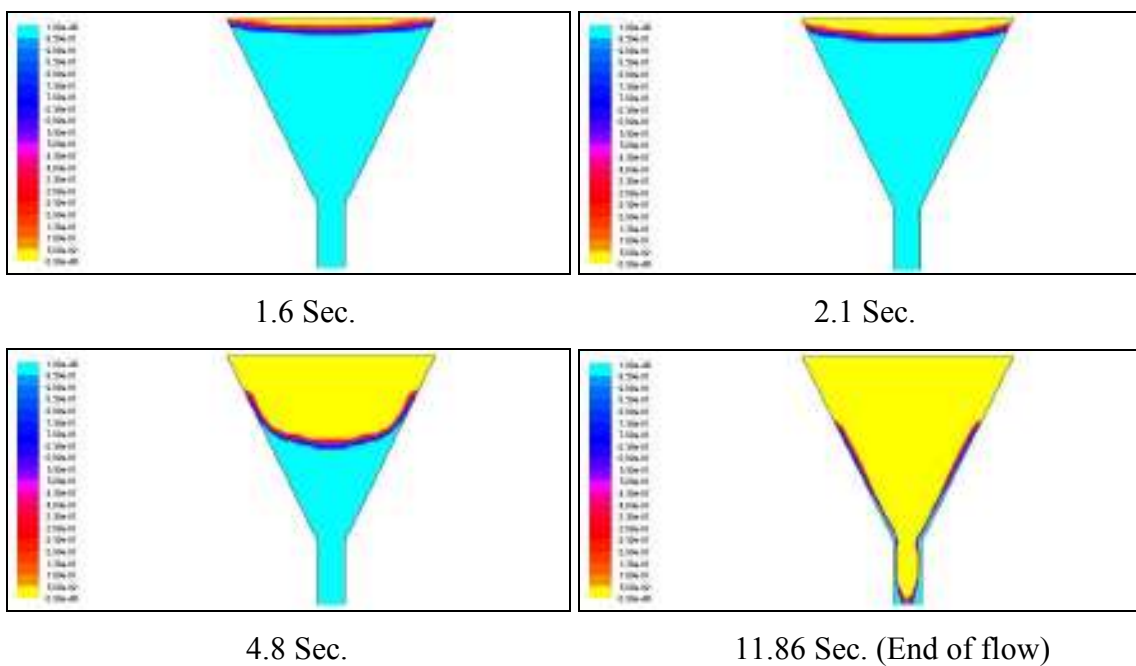


Figure A 28: Progressive Flow during the Simulation of V-funnel Test for the 2.5% Silica Fume.

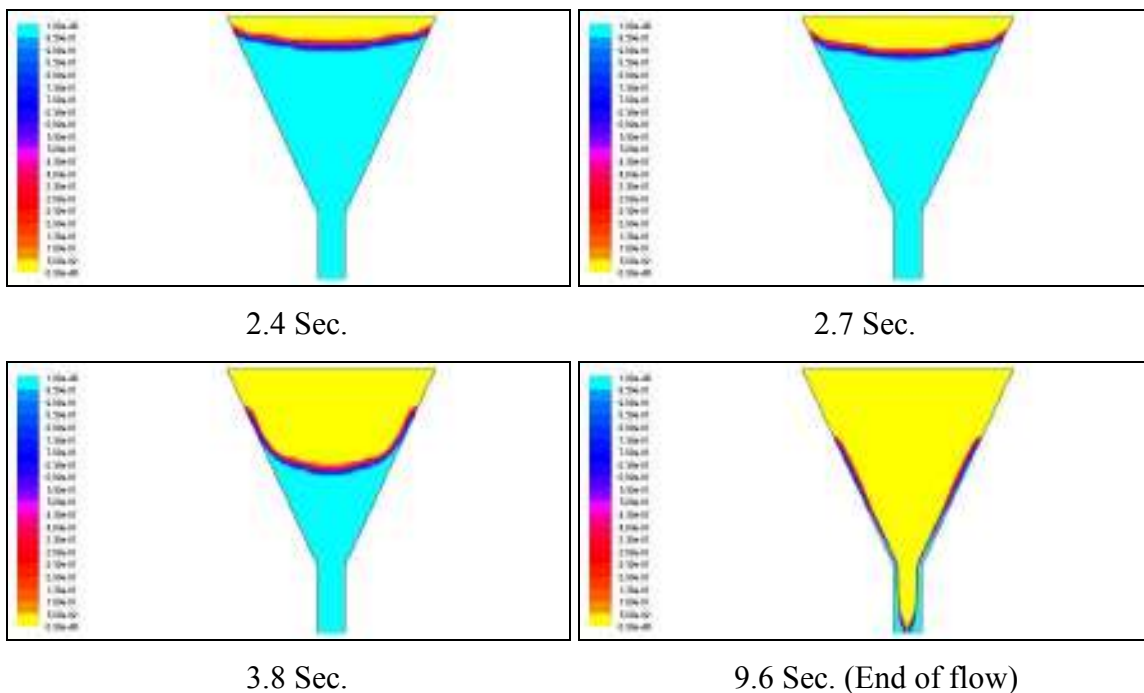


Figure A 29: Progressive Flow during the Simulation of V-funnel Test for the 5.0% Silica Fume.

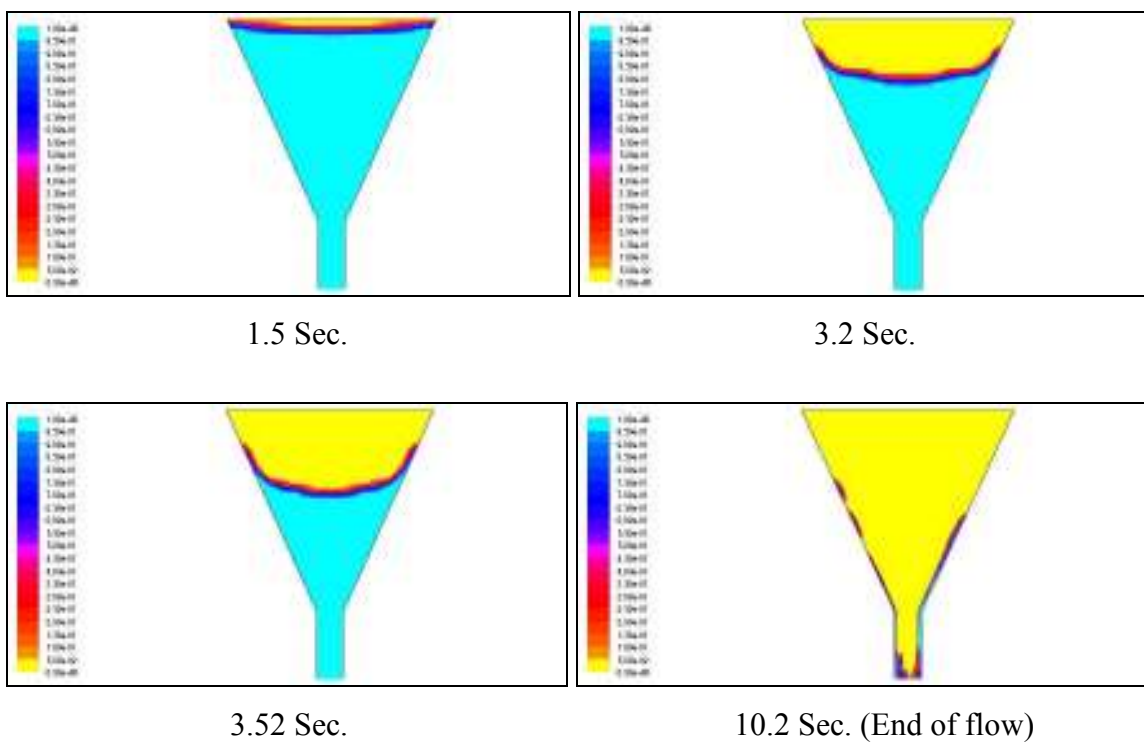


Figure A 30: Progressive Flow during the Simulation of V-funnel Test for the 7.5% Silica Fume.

## REFERENCES

1. Andriamanantsilavo, N. R. and Amziane S., “Maturation of fresh cement paste within 1- to 10-m-large formworks”. *Cement and Concrete Research*, V. 34, March 2004, pp. 2141–2152.
2. ANSYS inc., “ANSYS Inc. release notes; release 11.0”. Global Headquarters, South Pointe, 275 Technology Drive, Canonsburg, PA, Jan. 2007.
3. Arslan, M., Simsek, O., and Subasi, S. “Effects of formwork surface materials on concrete lateral pressure”. *Construction and Building Materials*, V. 19, 2005, pp. 319–325.
4. Assaad, J. J. and Khayat, K. H., “Effect of mixture consistency on formwork pressure exerted by highly flowable concrete”. *Journal of Construction Engineering and Management (ASCE)*, V. 18, 2006, pp. 786–791.
5. Assaad, J., Khayat, K. H. and Mesbah, H., “Variation of formwork pressure with thixotropy of self-consolidating concrete”. *ACI Materials Journal*, Jan-Feb 2003, pp. 29-37.
6. Baluch, M. H., Rahman, M. K. and Gadhib, A. H., “First progress report for Study on Segregation and Rheology of Self Compacting Concrete”. *Deanship of Scientific Research, King Fahd University of Petroleum and Minerals, Saudi Arabia*, 2010.
7. Baluch, M. H., Rahman, M. K., Mukhtar, F. and Malik, M. A., “A 2-D Computational Fluid Dynamics Simulation of Slump Flow and L-Box Test on SCC Using ANSYS/FLUENT”. *2<sup>nd</sup> International Engineering Mechanics and Materials Specialty Conference, Ottawa, Ontario Canada*, June 2011.
8. Barnes, H.A., “Thixotropy-A Review”. *Journal of Non-Newtonian Fluid Mechanics*, 70, 1997, pp. 1-33.
9. Bhaskaran, R. and Collins, L. “Introduction to CFD Basics”. *Cornell University - Sibley School of Mechanical and Aerospace Engineering, Ithaca, USA*, 2002.
10. Bhattacharya, A., Rayand, I. and Julio, F. D., “Effects of Aggregate Grading and Admixture/Filler on Self-Consolidating Concrete”. *The Open Construction and Building Technology Journal*, 2, 2008, pp. 89-95.

11. Billberg, P., "Form pressure generated by self-compacting concrete", *Proceedings of the 3<sup>rd</sup> international RILEM Symposium on Self-Compacting Concrete, Reykjavik, Iceland*, 17-20 August 2003, pp. 271-280.
12. Cyr, M., Legrand, C. and Mouret, M., "Study of the shear thickening effect of superplasticizers on the rheological behaviour of cement pastes containing or not mineral additives". *Cement and Concrete Research*, 30, 2000, pp. 1477-1483.
13. De Schutter, G., "Hydrodynamic modeling of the flow of self-compacting concrete in complex-shaped formworks". *Research proposal for Chinese students with CSC-scholarship, Department of Structural Engineering, Ghent university, Belgium*, 2008.
14. De Schutter, G., Audenaert, K., "Durability of Self-Consolidating Concrete-State of the art report", *RILEM Report 38, RILEM Publications*, 2007.
15. Dufour, F., Pijaudier-Cabot, G., "Numerical modeling of concrete flow: homogeneous approach". *International Journal for Numerical and Analytical Methods in Geomechanics*, V. 29, 2005, pp. 395-416.
16. Fluent Inc., *Fluent 6.1 User's Guide*, Lebanon, NH, USA, 2003.
17. Gallego, E., Fuentes, J. M., Ramírez, A. and Ayuga, F., "Design of Tall Formworks by a Finite-Element Model". *Journal of Construction Engineering and Management (ASCE)*, V. 136, July 2010, pp. 803–810.
18. Gallego, E., Fuentes, J. M., Ramírez, A. and Ayuga, F., "Computer simulation of complex-shaped formworks using three-dimensional numerical models". *Automation in Construction*, March 2011, doi: 10.1016/j.autcon.2011.03.001.
19. Gram, A., "Numerical Modeling of Self-Compacting Concrete Flow-Discrete and Continuous Approach". M.Sc. Thesis, *Department of Civil and Architectural Engineering, Division of Structural Design and Bridges, Stockholm, Sweden*, 2009.
20. Gregori, A., Ferron, R. P., Sun, Z. and Sha, S. P., "Experimental Simulation of Self-Consolidating Concrete Formwork Pressure". *ACI Materials Journal*, Jan-Feb 2008, pp. 97-104.
21. ICAR 2008. ICAR Rheometer Users Manual.
22. Khayat, K., Assaad, J., Mesbah, H. and Lessard, M., "Effect of section width and casting rate on variations of formwork pressure of self-consolidating concrete". *Materials and Structures*, V. 38, Jan-Feb 2005, pp. 73-78.

23. Khayat, K. H. and Assaad, J. J., "Measurement systems for determining formwork pressure of highly-flowable concrete". *Materials and Structures*, V. 41, Jan. 2007, pp. 37-46.
24. Khayat, K. H. and Assaad, J., "Use of thixotropy-enhancing agent to reduce formwork pressure exerted by self-consolidating concrete". *ACI Materials Journal*, Jan-Feb 2008, pp. 88-96.
25. Kim, J. H., Beacraft, M. and Sha, S. P., "Effect of mineral admixtures on formwork pressure of self-consolidating concrete". *Cement and Concrete Composites*, Aug. 2010, pp. 665-671.
26. Kim, J. H., Beacraft, M. W., Kwon, S. H., and Sha, S. P., "Simple analytical model for formwork design of self-compacting concrete". *ACI Materials Journal*, V. 108, Jan. 2011, pp. 38-45.
27. Kulasegaram, S., Karihaloo, B. L., Ghanbari, A., "Modelling the flow of self-compacting concrete". *International Journal for Numerical and Analytical Methods in Geomechanics*, 2010.
28. Kwon, S. H., Shah, S. P., Phung, Q. T., Kim, J. H. and Lee, Y., "Intrinsic model to predict formwork pressure". *ACI Materials Journal*, Jan-Feb 2010, pp. 20-26.
29. Lange, D.A., Struble, L.J., D'Ambrosia, M.D., Shen, L., Tejada-Dominguez, F., Birch, B.F., and Brinks, A.J., "Performance and Acceptance of Self Consolidating Concrete". Final Report, Research Report FHWA-ICI-08-020, *Illinois Center for Transportation*, July 2008.
30. Malik, M. A., "Study on Segregation and Rheology of Self Compacting Concrete". M. S. thesis, *Department of Civil Engineering, King Fahd University of Petroleum and Minerals, Saudi Arabia*, 2011.
31. Mori, H., Tanigawa, Y., "Simulation Methods for Fluidity of Fresh Concrete". *Memoirs of the School of Engineering, Nagoya University*, Vol. 44, No. 1992, pp. 71-133.
32. Nguyen, V.H., Remond, S., Gallias, J.L., Bigas, J.P., Muller, P., "Flow of Herschel-Bulkley fluids through the Marsh cone". *Journal of Non-Newtonian Fluid Mechanics*, vol 139, pp. 128-134, 2006.

33. Ovalez, G. and Roussel, N., "A physical model for the prediction of lateral stress exerted by self-compacting concrete on formwork". *Materials and Structures*, V. 39, Aug. 2005, pp. 269-279.
34. Raza, A., "Moisture Transport and Shrinkage in New Generation Concretes". M.S., *Dept. of Civil Engineering, King Fahd University of Petroleum and Minerals, Dhahran, Saudi Arabia*, 2006.
35. Roussel, N., "Three-dimensional numerical simulations of slump tests". *Annual transactions of the NORDIC rheology society*, vol. 12, 2004.
36. Roussel, N., "A thixotropy model for fresh fluid concretes: theory, validation and applications". *Cement and Concrete Research*, vol. 36, 2006, pp. 1797-1706.
37. Roussel, N., "Rheology of Fresh Concrete: From Measurements to Predictions of Casting Processes". *Materials and Structures*, Vol. 40, No. 10, Oct. 2007, pp. 1001-1012.
38. Roussel, N., Geiker, MR., Dufour, F., Thrane, L.N., Szabo, P., "Computational modeling of concrete flow: general overview". *Cement and Concrete Research* 2007(a), 37, 1298-1307.
39. Roussel, N., Staquet, S., D'Aloia Schwarzentruher, L., Le Roy., Toutlemonde, F., "SCC casting prediction for the realization of prototype VHPC-precambered composite beams". *RILEM Materials and structures*, March 2007(b), pp. 877-887.
40. Thrane, L.N., Szabo, P., Geiker, M., Glavind, M., Stang, H., "Simulation of the Test Method 'L-Box' for Self-Compacting Concrete". *Annual Transactions of the NORDIC rheology society*, vol. 12, 2004.
41. Vanhove, Y., Djelal, C. and Magnin, A., "Prediction of the lateral pressure exerted by self-compacting concrete on formwork". *Magazine of Concrete Research*, V. 56, Feb. 2004, pp. 55-62.
42. Wallewick, J.E., "Rheology of Particle Suspensions; Fresh Concrete, Mortar and Cement Paste with Various Types of Lignosulphonates". Ph.D. Thesis, *Department of Structural Engineering, Norwegian University of Science and Technology*, 2003.



## VITA

**NAME** : **Faisal Mukhtar**  
**PLACE OF BIRTH** : Daura, Katsina State, Nigeria.  
**E-MAIL** : [mk\\_faisal@hotmail.com](mailto:mk_faisal@hotmail.com)

### EDUCATIONAL QUALIFICATIONS

- **M.Sc Civil Engineering - Structures** (December, 2011)  
King Fahd University of Petroleum and Minerals, Dhahran, Saudi Arabia.
- **B.Eng Civil Engineering** (February, 2008)  
Bayero University Kano, Nigeria.

### MAJOR ACHIEVEMENTS AND AWARDS

- Award for the best final year research project in the B.Eng program.
- Obtained First Class Honors at the completion of the B.Eng program.
- Obtained First Class Honors at the completion of the M.Sc program.